REGULATION OF P GRANULES BY THE DISORDERED PROTEIN MEG-3

by
Helen Frances Schmidt

A dissertation submitted to Johns Hopkins University in conformity with the

requirements for the degree of Doctor of Philosophy

Baltimore, Maryland
December 2020

Abstract

C. elegans P granules are RNA granules which form in the zygote and are preferentially segregated to the germ cell lineage as the embryo develops. Formation of P granules in the embryo requires the intrinsically disordered protein MEG-3 and its close paralog MEG-4. In the absence of MEG-3/4, many protein and RNA components of the germ plasm are not properly concentrated in the embryonic germ cells. Consequently *meg-3 meg-4* worms are approximately 30% sterile.

In this study we use genome editing at the endogenous locus as well as *in vitro* techniques to perform a structure-function analysis of MEG-3. In the course of this work, we have greatly expanded our ability to perform genome editing in *C. elegans.*

We find that the long N-terminal intrinsically disordered region (IDR) of MEG-3 is necessary and sufficient to bind RNA *in vitro,* while *in vivo* the IDR is required enrich MEG-3 in the germ lineage. The C-terminus of MEG-3 is required both to form granules *in vivo* and to bind to PGL-1 and PGL-3, two protein components of P granules. We also identify a region within the C-terminus of MEG-3 with homology to HMG-box domains. By mutating four amino acids within this HMG-like motif, we completely disrupted the MEG-PGL interaction *in vivo*. Finally, the MEG-3 IDR, C-terminus and HMG-like motif are all required to enrich mRNAs in the germline and protect them from degradation. This study provides evidence for a greater role of globular protein-protein interaction domains in the assembly of RNA granules

Primary Reader and Advisor: Geraldine Seydoux

Secondary Reader: Jeffry Corden

Preface

This dissertation would not have been possible without the support of many colleagues, friends, and family. Firstly, Geraldine has been the most incredible mentor. Her curiosity and enthusiasm for science is contagious. I could not begin to count all the things I have learned about being a good scientist from her. She has build a collaborative and welcoming environment in the lab. Every one of my lab mates has helped me work out scientific problems, but they also make me laugh and keep going when things don't seem to be working. Outside of the lab, I have supported by the MBG department and Human Genetics program. Special thanks to Jeffry Corden, Erika Matunis, and Takanari Inoue for serving on my thesis committee and providing a great deal of advice on both scientific and career matters. My friends at Hopkins and outside have also helped me immensely, especially my roommates Allison and Rachel and my long-time friend Savannah. To my partner Jack, not every couple could get through medical school and grad school for so many years in separate cities, but we did it. Thank you for your love and support and for all your hard work so that we could grow together. And finally, my thank you to my Mom and Dad, who did all the wonderful supportive things parents do for their children, but also taught me how to extract DNA from peas and how to set up a PCR. Thank you all.

Table of Contents

Abstract ii

Preface iii

Table of Contents iv

List of Tables vi

List of Figures vii

Chapter 1 1

Introduction 1

The role of RNA granules in the germline 2

RNA granule formation by liquid-liquid phase separation 2

Germ granule assembly is not well explained by the LLPS model 3

The *C. elegans* P granule as a model for RNA granule assembly 3

MEG-3/4 are required redundantly for P granule assembly and localization 4

Thesis Aims 5

Chapter 2 6

Coordination of RNA and protein condensation by the P granule protein MEG-3 6

2.1 Summary 7

2.2 Results 7

2.3 Discussion 17

2.4 Methods 23

2.5 Acknowledgements 31

2.5 Figures 32

Chapter 3 54

Conclusions and Final Thoughts 54

3.1 Summary 55

How do P granules protect mRNA from degradation? 55

What is the role of MEG-3 phosphorylation in P granule assembly? 56

Final thoughts 58

Appendix A 59

Insertion of short peptide tags via CRISPR/Cas9 genome editing using single-stranded DNA oligos 59

A.1 Rationale 60

A.2 Results 61

A.3 Discussion 61

A.4 Methods 62

A.5 Figures 65

Appendix B 68

CRISPR/Cas9 replication of *mbk-2(dd5)* temperature sensitive mutant 68

B.1 Rationale 69

B.2 Results 69

B.3 Conclusions and further questions 70

B.4 Methods 70

B.5 Figures 72

Appendix C **75**
Simultaneous alanine substitution of 14 putative phosphorylation sites in MEG-3 **75**
C.1 Rationale 76
C.2 Results 76
C.3 Conclusions and further questions 79
C.4 Methods 81
C.5 Figures 85
Appendix D **95**
Replacement of all serines in the MEG-3 intrinsically disordered region (aa1-544) with alanine **95**
D.1 Rationale 96
D.2 Results 96
D.3 Conclusions and further questions 97
D.4 Methods 98
D.5 Figures 100
Appendix E **110**
RNAi insensitivity of MEG-3 derivatives **110**
E.1 Rationale 111
E.2 Results 111
E.3 Conclusions and further questions 111
E.5 Figures 113
Appendix F **116**
Table of *C. elegans* strains generated in this work **116**
References **119**
CURRICULUM VITAE **130**

List of Tables

Appendix A

Table 1 – Embryonic lethality of CRISPR-generated *mbk-2(dd5)* alleles at 25˚ C**..... 72**

Appendix E

Table 1 – Individual replicate values for response to RNAi treatment of MEG-3 derivatives **..... 115**

Appendix F

Table 1 – *C. elegans* strains generated by CRISPR/Cas9 editing in the course of this work. **..... 117**

List of Figures

Chapter 2

Figure 1 - Domain organization of MEG-3 ..... **32**
Figure 2 - *in vitro* characterization of wild-type MEG-3 and variants **34**
Figure 2 - supplement 1 – Supplementary *in vitro* characterization of wild-type MEG-3 and variants **36**
Figure 3 - Localization of wild-type MEG-3 and variants in early embryos **38**
Figure 3 - supplement 1 – Additional characterization of wild-type MEG-3 and variants in embryos **40**
Figure 4 - Localization of PGL-3 relative to wild-type MEG-3 and variants in two cell embryos **42**
Figure 4 - supplement 1 - Localization of PGL-3 relative to wild-type MEG-3 and variants in P_4 blastomeres **44**
Figure 5 - Distribution of *Y51F10.2* mRNA in embryos expressing wild-type MEG-3 and variants **46**
Figure 5 - supplement 1 - Distribution of T26A5.2 and polyadenylated mRNAs in embryos expressing wild-type MEG-3 and variants **48**
Figure 5 - supplement 2 - Distribution of *nos-2* mRNA in embryos expressing wild-type MEG-3 and variants **50**
Figure 6 - Diagram summarizing the distributions of MEG-3 and PGL-3 condensates and Y51F10.2 mRNA in P blastomeres. **52**

Appendix A

Figure 1 – MEG-1::OLLAS in the early embryo **66**

Appendix B

Figure 1 – MBK-2 activity is required for MEG-3 and PGL-1 asymmetry in the early embryo **73**

Appendix C

Figure 1 - Diagram of the generation of MEG-3_{14A} in one (A) or two (B) steps. **85**
Figure 1 – supplement 1 DNA and protein sequences of strains used in generation MEG-3_{14A} **87**
Figure 2 - Characterization of MEG-3_{14A} **93**

Appendix D

Figure 1 - Diagram of the insertion of MEG-$3_{IDR\ 87A}$ at the *meg-3* locus using CRISPR/Cas9. ..... **100**

Figure 1 – supplement 1 DNA and protein sequences of MEG-$3_{IDR\ 87A}$ aligned with MEG-3_{IDR} **102**
Figure 2 - Western blot to confirm MEG-$3_{IDR\ 87A}$ expression **106**
Figure 3 - MEG-$3_{IDR\ 87A}$ localization in embryos **108**

Appendix E

Figure 1 – Response to RNAi treatment of MEG-3 derivatives **113**

Chapter 1

Introduction

This chapter is an edited portion of “Coordination of RNA and protein condensation by the P granule protein MEG-3” by Schmidt, H**.,** Putnam, A., Rasoloson, D., and Seydoux, G. in 2020 Available on bioRxiv https://doi.org/10.1101/2020.10.15.340570

The role of RNA granules in the germline

In animals with germ plasm, specification of the germline depends on the segregation of maternal RNAs and proteins (germline determinants) to the primordial germ cells. Germline determinants assemble in germ granules, micron-sized dense assemblies that concentrate RNA and RNA-binding proteins (Jamieson-Lucy and Mullins, 2019; Marnik and Updike, 2019; Seydoux, 2018; Trcek and Lehmann, 2019). Superficially, germ granules resemble RNA-rich condensates that form in the cytoplasm of somatic cells, including P bodies and stress granules.

RNA granule formation by liquid-liquid phase separation

In recent years, much progress has been made in our understanding of stress granule assembly with the realization that stress granules resemble liquid condensates that assemble by liquid-liquid phase separation (LLPS). LLPS is a thermodynamic process that causes interacting molecules to dynamically partition between a dense condensed phase and a more dilute phase (e.g. the cytoplasm) (Banani et al., 2017; Mitrea and Kriwacki, 2016). Low-affinity binding interactions, often involving disordered and RNA-binding domains, are sufficient to drive LLPS of proteins and RNA in reconstituted systems (Lin et al., 2015; Molliex et al., 2015; Zagrovic et al., 2018). The ability of RNA to phase separate in the absence of proteins *in vitro* has also been proposed to contribute to RNA granule assembly *in vivo*, especially in the case of stress granules which arise under conditions of general translational arrest (Tauber et al., 2020; Van Treeck et al., 2018). An emerging model is that the combined action of many low-affinity interactions between RNA molecules and multivalent RNA-binding proteins create RNA-based

protein networks that drive LLPS (Guillén-Boixet et al., 2020; Sanders et al., 2020; Yang et al., 2020; Zhang et al., 2015).

Germ granule assembly is not well explained by the LLPS model

Unlike the dynamic condensates assembled by LLPS *in vitro*, germ granules are not well-mixed, single-phase liquid droplets. High resolution microscopy has revealed that germ granules are heterogenous assemblies of dynamic and less dynamic condensates that co-assemble but do not fully mix. For example, Drosophila germ granules contain non-dynamic RNA clusters embedded in dynamic, protein-rich condensates (Little et al., 2015; Niepielko et al., 2018; Trcek et al., 2015). Germ granules in zebrafish and Xenopus are built on an amyloid-like scaffold that organizes mRNAs in non-overlapping, transcript-specific zones (Boke et al., 2016; Fuentes et al., 2018; Roovers et al., 2018). The mechanisms that bring together condensates with different material properties and their contribution to RNA recruitment in germ granules are not well understood.

The *C. elegans* P granule as a model for RNA granule assembly

In this study, we examine the assembly of P granules, the germ granule of *C. elegans*. At the core of P granules are liquid condensates assembled by PGL proteins. PGL-1 and PGL-3 are self-dimerizing, RGG domain proteins that readily form condensates able to recruit other P granule components, such as the VASA-related RNA helicase GLH-1 (Aoki et al., 2016; Hanazawa et al., 2011; Saha et al., 2016; Updike et al., 2011). PGL condensates exist in germ cells throughout oogenesis and are maternally-inherited by the embryo. In newly fertilized zygotes, the surface of PGL condensates

becomes covered by smaller condensates assembled by MEG-3 and MEG-4, two homologous intrinsically-disordered proteins (Wang et al., 2014).

MEG-3/4 are required redundantly for P granule assembly and localization

MEG-3 and MEG-4 are 71% identical at the amino acid level, and have a similar domain organization, with an N-terminal disordered region and a more ordered C-terminus. We have focused on MEG-3 in this and other studies, however, we expect MEG-4 to behave similarly given their genetic redundancy (single mutants are fertile) and their high degree of identity at the sequence level. Unlike PGL condensates, MEG-3 condensates resist dilution and salt challenge, consistent with a gel-like material (Putnam et al., 2019). (In this study, we use the term condensate to refer to concentrated protein assemblies that self-assemble without implying a mechanism for assembly, which could involve aggregation, LLPS or other mechanisms). During zygote polarization, MEG-3 an MEG-4 enrich with other germ plasm components in the posterior cytoplasm (Putnam et al., 2019; Smith et al., 2016; Wang et al., 2014). This relocalization correlates with preferential growth of MEG-coated PGL droplets in the posterior and dissolution of “naked” PGL droplets in the anterior side (Brangwynne et al., 2009; Smith et al., 2016).

In addition to PGL and MEG co-assemblies, P granules also concentrate specific maternal transcripts (Parker et al., 2020; Seydoux and Fire, 1994). A survey of mRNAs that immunoprecipate with PGL-1 and MEG-3 suggest that MEG-3 is most directly responsible for recruiting mRNAs to P granules (Lee et al., 2020). MEG-3 binds to ~500s maternal mRNAs, including transcripts coding for germline determinants. Recruitment

of mRNAs to P granules ensures their preferential segregation to the primordial germ cells. Embryos lacking MEG-3 and MEG-4 do not localize PGL droplets, do not condense P granule-associated mRNAs, and display partially penetrant (30%) sterility (Lee et al., 2020; Wang et al., 2014).

Thesis Aims

My work in Geraldine Seydoux's lab was focused on the three following aims focused on understanding how MEG-3 contributes to P granule assembly:

1. Identify essential domains of MEG-3
2. Determine which MEG-3 domains are required for condensation
3. Determine which MEG-3 domains are required to recruit germline proteins and mRNAs to P granules

Chapter 2

Coordination of RNA and protein condensation by the P granule protein MEG-3

This chapter is an edited portion of "Coordination of RNA and protein condensation by the P granule protein MEG-3" by Schmidt, H**.,** Putnam, A., Rasoloson, D., and Seydoux, G. in 2020 Available on bioRxiv https://doi.org/10.1101/2020.10.15.340570

2.1 Summary

MEG-3 is related to the GCNA family and contains an N-terminal disordered region (IDR) and a predicted ordered C-terminus featuring an HMG-like motif (HMGL). Using *in vitro* and *in vivo* experiments, we find the MEG-3 C-terminus is necessary and sufficient to build MEG-3/PGL co-condensates independent of RNA. The HMGL domain is required for high affinity MEG-3/PGL binding *in vitro* and for assembly of MEG-3/PGL co-condensates *in vivo*. The MEG-3 IDR binds RNA *in vitro* and is required but not sufficient to recruit RNA to P granules. Our findings suggest that P granule assembly depends in part on protein-protein interactions that drive condensation independent of RNA.

2.2 Results

The MEG-3 IDR and C-terminus synergize to promote MEG-3 condensation *in vitro*

IUPred2A (Mészáros et al., 2018) predicts in the MEG-3 sequence a 544 residue N-terminal domain with high disorder (MEG-3_{IDR}, aa1-544) and a 318 residue C-terminal domain (MEG-3_{Cterm}, aa545-862) with lower disorder (Figure 1A, B). MEG-3_{Cterm} contains a region (aa700-744) with sequence similarity to the HMG-like motif found in the GCNA family of intrinsically-disordered proteins (Figure 1C). GCNA family members also contain long N-terminal disordered domains, but these do not share sequence homology with the MEG-3 IDR (Carmell et al., 2016) .

To determine which regions of MEG-3 are required for condensation *in vitro,* we expressed and purified His-tagged full-length MEG-3 and four derivatives: MEG-3_{Cterm}, MEG-3_{IDR}, MEG-3_{698} an extended version of MEG-3_{IDR} terminating right before the HMG-

like motif, and MEG-3_{HMGL-}, a full length MEG-3 variant with alanine substitutions in 4 conserved residues in the HMG-like motif (Figure 1B, C). The proteins were trace-labeled (Methods) with covalently attached fluorophores and condensation was assayed as a function of protein concentration in the presence of 150mM NaCl and 20ng/µl of *nos-2* RNA (*nos-2* is an mRNA found in P granules (Lee et al., 2020; Subramaniam and Seydoux, 1999, p. 1)). Wild-type MEG-3 forms small condensates at 50nM, a concentration similar to that estimated for MEG-3 *in vivo* (Putnam et al., 2019; Saha et al., 2016). With increasing protein concentration, the fraction of MEG-3 in condensates increases (Figure 2A and B). MEG-3_{HMGL-} behaved indistinguishably from wild-type. In contrast, the MEG-3_{Cterm} and MEG-3_{IDR} lagged behind, with the MEG-3_{IDR} lagging the most at the lowest concentration (Figure 2B). MEG-3_{698} behaved like MEG-3_{IDR} (Figure 2 – supplement 1A). We conclude that both the IDR and C-terminus contribute to MEG-3 condensation *in vitro*.

Co-assembly of MEG-3/PGL-3 condensates *in vitro* is driven by the MEG-3 C-terminus and does not require RNA or the MEG-3 IDR

When combined in condensation assays, MEG-3 and PGL-3 form co-condensates that resemble the architecture of P granules *in vivo*, with the smaller MEG-3 condensates (~100 nm) forming a dense layer on the surface of the larger PGL-3 condensates (Putnam et al., 2019). MEG-3_{Cterm} and MEG-3_{HMGL-} formed co-condensates with PGL-3 that were indistinguishable from those formed by wild-type MEG-3(Figure 2C). The MEG-3_{IDR}, in contrast, failed to assemble condensates on the surface of PGL-3,

or away from PGL-3, and instead mixed homogenously with the PGL-3 phase as previously reported (Putnam et al. 2019, Figure 2C).

We repeated the co-condensation assays in the absence of RNA using a higher concentration of PGL to force PGL condensation in the absence of RNA. MEG/PGL co-condensates assembled under those conditions were indistinguishable from co-condensates assembled in the presence of RNA (Figure 2C). Again, the C-terminus was necessary and sufficient for co-assembly. MEG-3_{IDR} homogenously mixed with the PGL-3 phase and did not form independent condensates, confirming that MEG-3_{IDR} is solubilized by PGL-3. We conclude that the MEG-3 C-terminus is the primary driver of MEG-3 condensation and that condensation of MEG-3 on PGL condensates depends on the MEG-3 C-terminus and does not require RNA *in vitro*.

The MEG-3 IDR is necessary and sufficient for RNA binding *in vitro*

Using fluorescence polarization and gel shift assays, we previously showed that the MEG-3 IDR binds an RNA oligo (poly-U30) with near nanomolar affinity *in vitro* (Smith et al., 2016). We repeated these observations using a filter binding assay where proteins are immobilized on a filter to minimize possible interference due to condensation of MEG-3 in solution (Methods, Figure 2D-G). Consistent with previous observations (Smith et al., 2016), we found that the MEG-3_{IDR} exhibits high affinity for RNA (Kd=105 nM; Figure 2F). MEG-3_{698} also exhibited high affinity (Kd=95 nM; Figure 2 – supplement 1B). Wild-type MEG-3 bound RNA efficiently (Figure 2D), albeit at a lower affinity than MEG-3_{IDR} and MEG-3_{698}. In contrast, MEG-3_{Cterm} exhibits negligible RNA

binding (Figure 2E). HMG domains are common in DNA-binding proteins and have been shown to mediate protein:nucleic acid interactions *in vivo* (Genzor and Bortvin, 2015; Reeves, 2001; Thapar, 2015), raising the possibility that the HMG-like domain in MEG-3 might contribute to RNA binding. We found, however, that the MEG-3_{HMGL-} bound to RNA with high affinity, similar to wild-type MEG-3 (Figure 2G). We conclude that the HMG-like domain does not contribute to RNA binding, which is driven primarily by the IDR.

The HMG domain is required for high affinity binding to PGL proteins *in vitro*

HMG domains have also been implicated in protein-protein interactions (Reeves, 2001; Stros et al., 2007; Wilson and Koopman, 2002). We reported previously that MEG-3 binds directly to PGL-1, as determined in a GST-pull down assay using partially purified recombinant proteins (Jennifer T Wang et al., 2014). We repeated this assay using fusion proteins of GST::MEG-3_{Cterm} and MBP::PGL-1 and PGL-3. GST::MEG-3_{IDR} fusions were not expressed and thus could not be tested in this assay. We found that the GST:MEG-3_{Cterm} binds efficiently to PGL-1 and PGL-3, but not to MBP or to an unrelated control protein PAA-1. Remarkably, we found that the HMG-like motif contributes to these interactions. A GST::MEG-3_{Cterm} fusion with mutations in the HMG-like domain bound less efficiently to PGl-1 and PGL-3 (Figure 2H, Figure 2 – supplement 1C). We conclude that the MEG-3_{Cterm} is sufficient to bind to PGL proteins *in vitro* and that these interactions require the HMG-like motif for high efficiency binding.

The MEG-3 C-terminus is the primary driver of MEG-3 condensation *in vivo*

To test the functionality of MEG-3 domains *in vivo*, we used CRISPR genome editing to re-create at the *meg-3* locus the same variants analyzed *in vitro*. We used a *C. elegans* strain line with the *meg-4* locus deleted to avoid possible complementation by MEG-4. To allow visualization of MEG-3 protein by immunofluorescence, each variant (and wild-type *meg-3*) was tagged with a C-terminal OLLAS peptide. We avoided the use of fluorescent tags as fluorescent tags have been reported to affect the behavior of proteins in P granules (Uebel and Phillips, 2019).

As reported previously for untagged MEG-3 (Jennifer T Wang et al., 2014), MEG-3 tagged with OLLAS (JH3477) could be detected diffusively in the cytoplasm and in condensates. Before polarization, MEG-3 was uniformly distributed throughout the zygote. After polarization, MEG-3 in the cytoplasm and in condensates became enriched in the posterior half of the zygote destined for the germline blastomere P_1 ("germ plasm"). MEG-3 continued to segregate preferentially with P blastomeres in subsequent divisions (P_1 through P_4) (Figure 3A).

All four MEG-3 variants exhibited unique localization patterns distinct from wild-type. MEG-3_{IDR} (JH3479) enriched in posterior cytoplasm and segregated preferentially to P blastomeres but did not appear robustly in condensates until the 4-cell stage (P_2 blastomere, Figure 3A). MEG-3_{698} (JH3630) behaved similarly to MEG-3_{IDR} (Figure 3 – supplement 1A). MEG-3_{Cterm} (JH3553) did not enrich asymmetrically in the cytoplasm but formed condensates in the zygote posterior and continued to form condensates only in P blastomeres despite being present in the cytoplasm of all cells (Figure 3A).

MEG-3_{HMGL-} (JH3861) behaved most similarly to wild-type MEG-3 enriching in the zygote posterior and forming condensates as early as the 1-cell stage, although the condensates appeared smaller at all stages (Figure 3A).

For each MEG-3 derivative, we quantified the number of condensates and the degree of enrichment in the P blastomere over somatic blastomeres and in condensates over the cytoplasm. Wild-type MEG-3 and MEG-3_{HMGL-} formed a similar number of condensates, while MEG-3_{Cterm} formed fewer and MEG-3_{IDR} the least in the 4-cell stage (Figure 3B). The MEG-3_{Cterm} did not enrich in the P_2 blastomere, whereas MEG-3_{IDR} and MEG-3_{HMGL-} enriched as efficiently as wild-type (Figure 3C). Finally, none of MEG-3 derivatives enriched in condensates as efficiently as wild-type (Figure 3D).

After the four-cell stage, the low levels of wild-type MEG-3 and MEG-3_{HMGL-} inherited by somatic blastomeres were rapidly cleared. In contrast, MEG-3_{IDR} and MEG-3_{Cterm} persisted in somatic blastomeres at least until the 28-cell stage (Figure 3 – supplement 1B). Western analyses revealed that MEG-3 and MEG-3_{HMGL-} accumulate to similar levels, whereas MEG-3_{IDR} and MEG-3_{Cterm} were more abundant in mixed-stage embryo lysates, consistent with slower turnover in somatic lineages (Figure 3 – supplement 1C).

The condensation, segregation, and turnover patterns of MEG-3, MEG-3_{IDR}, MEG-3_{Cterm} MEG-3_{HMGL-} are summarized in Figure 3E. From this analysis, we conclude that: 1) the MEG-3 IDR is necessary and sufficient for enrichment of cytoplasmic MEG-3 in germ plasm, 2) the MEG-3 C-terminus is necessary and sufficient for condensation of MEG-3 in germ plasm starting in the zygote stage, 3) the HMG-like motif is required for efficient

MEG-3 condensation, and 4) both the C-terminus and the IDR are required for timely turn-over of MEG-3 in somatic lineages.

Co-assembly of MEG-3/PGL-3 condensates *in vivo* is driven by the MEG-3 C-terminus and requires the HMGL motif

MEG-3 and MEG-4 are required redundantly to localize PGL condensates to the posterior of the zygote for preferential segregation to the P lineage (Smith et al., 2016; Jennifer T Wang et al., 2014). To examine the distribution of PGL condensates relative to MEG-3 condensates, we utilized the KT3 and OLLAS antibodies for immunostaining of untagged endogenous PGL-3 and OLLAS-tagged MEG-3. In embryos expressing wild-type MEG-3, MEG-3 and PGL-3 co-localize in posterior condensates that are segregated to the P_1 blastomere. (Figure 4A). In embryos lacking *meg-3* and *meg-4*, PGL-3 condensates distributed throughout the cytoplasm of the zygote and segregated equally to AB and P_1 (Figure 4A). We observed a similar pattern in embryos expressing MEG-3_{IDR}, MEG-3_{698} and MEG-3_{HMGL-} indicating that none of these MEG-3 derivatives are sufficient to localize PGL condensates (Figure 4A, Figure 3 – supplement 1A). In contrast, in embryos expressing MEG-3_{Cterm}, PGL-3 condensates localized properly in P_1, although they were smaller and fewer than in wild-type (Figure 4A and B). Embryos expressing MEG-3_{Cterm} enriches PGL-3 in P_1, though not as efficiently as wild-type, while PGL-3 is not enriched in *meg-3 meg-4*, or embryos expressing MEG-3_{IDR} or MEG-3_{HMGL-} (Figure 4C). In wild-type 28-cell stage embryos, PGL-3 condensates are highly enriched in P_4. No such enrichment was observed in embryos expressing the MEG-3_{Cterm} or any other MEG-

3 variant (Figure 4 – supplement 1). We conclude that the MEG-3_{Cterm} is sufficient to enrich PGL-3 condensates in P blastomeres in early stages, but not sufficient to support robust PGL-3 localization through P_4.

Wild-type MEG-3 condensates associate closely with the surface of PGL condensates (Putnam et al., 2019; Jennifer T Wang et al., 2014). With the resolution afforded by immunostaining, this configuration appears as co-localized MEG and PGL puncta in fixed embryos (Wang et al., 2014, Figure 4B). We found that PGL-3 condensates co-localized with MEG-3_{Cterm} condensates (37/37 PGL-3 condensates scored in P_1; Figure 4B) as in wild-type. In contrast, we observed no such colocalization with MEG-3_{IDR} or MEG-3_{HMGL-}. The MEG-3_{IDR} is mostly cytoplasmic and forms only rare condensates in P_2. We occasionally observed PGL condensates with an adjacent MEG-3_{IDR} condensate (5/19 PGL-3 condensates scored in P_1, Figure 4B), but these were not co-localized. Unlike the MEG-3_{IDR}, MEG-3_{HMGL-} forms many condensates in P_2, although these tended to be smaller than wild-type (Figure 3A,B). Still, although we occasionally observed PGL condensates with an adjacent MEG-3_{HMGL-} condensate (12/30 PGL-3 condensates scored in P_1; Figure 4B), we never observed fully overlapping PGL/MEG-3_{HMGL-} co-condensates. We conclude that, despite forming many condensates in P blastomeres, MEG-3_{HMGL-} condensates do not associate efficiently with, and do not support the localization of, PGL-3 condensates.

Efficient recruitment of mRNA to P granules requires the MEG-3 IDR, C-terminus and HMG-like motif

MEG-3 recruits mRNAs to P granules by direct binding which traps mRNA into the non-dynamic MEG-3 condensates (Lee et al., 2020). To determine which MEG-3 domain is required for mRNA recruitment to MEG-3 condensates *in vivo*, we performed *in situ* hybridization against the MEG-3-bound mRNA *Y51F10.2.* Prior to polarization, *Y51F10.2* is uniformly distributed throughout the zygote cytoplasm (Figure 5A). *Y51F10.2* becomes progressively enriched in P granules starting in the late 1-cell stage and forms easily detectable micron-sized foci by the 4-cell stage ((Lee et al., 2020), Figure 5A). In contrast, in *meg-3 meg-4* embryos, *Y51F10.2* remains uniformly distributed in the cytoplasm at all stages. Strikingly, we observed the same failure to assemble *Y51F10.2* foci in embryos expressing MEG-3_{IDR}, MEG-3_{Cterm} and MEG-3_{HMGL-} (Figure 5A). This was surprising since all three MEG-3 variants form visible condensates by the 4-cell stage (Figure 3A). We note that lack of PGL enrichment in posterior cytoplasm is unlikely to cause this RNA defect since *pgl-1;pgl-3* mutants still assemble *Y51F10.2* clusters (Lee et al., 2020).

To characterize the fate of *Y51F10.2* transcripts in *meg-3 meg-4* mutants, we compared the intensity of the *Y51F10.2 in situ* hybridization signal relative to a control RNA in 1-cell and 4-cell stage embryos (Methods, Figure 5 – supplement 1A,B). In wild-type, *Y51F10.2* RNA levels do not change significantly from the 1-cell to the 4-cell stage. In contrast, in *meg-3meg-4* embryos, *Y51F10.2* levels decreased by ~50% by the 4-cell stage, despite starting at levels similar to wild-type in the 1-cell stage. This finding is consistent with RNAseq results, which indicated lower levels of P granule mRNAs in *meg-3 meg-4* embryos (Lee et al., 2020). We observed a similar loss of *Y51F10.2* RNA in

embryos expressing MEG-3_{IDR}, MEG-3_{Cterm} and MEG-3_{HMGL-} (Figure 5B). We repeated this analysis with probes recognizing an additional MEG-3 bound mRNA, *nos-2.* Similar to *Y51F10.2* RNA, *nos-2* RNA levels remained constant between one- and four-cell stages of embryos expressing wild-type MEG-3, but decreased between the one- and four-cell stages of *meg-3 meg-4* embryos and those expressing MEG-3_{IDR}, MEG-3_{Cterm} and MEG-3_{HMGL-} (Figure 5 – supplement 2).These results suggest that failure to recruit *Y51F10.2* and *nos-2* in granules leads to premature degradation.

After the 4-cell stage, as has been reported for other maternal RNAs (Baugh et al., 2003; Seydoux and Fire, 1994), *Y51F10.2* is rapidly turned over in somatic blastomeres. At the four cell stage, Y*51F10.2* mRNA levels are ~2-fold higher P_2 than in somatic blastomeres in wild-type embryos, and ~1.2 fold higher in *meg-3 meg-4* embryos and in embryos expressing MEG-3_{IDR}, MEG-3_{Cterm} and MEG-3_{HMGL-} (Figure 5C). By the 28-cell stage, in wild-type embryos, Y*51F10.2* levels are ~10-fold higher in the germline founder cell P_4 compared to somatic blastomeres. In contrast, in *meg-3 meg-4* embryos, *Y51F10.2* mRNA levels were only ~2-fold enriched over somatic levels. Similarly, in embryos expressing the MEG-3_{IDR}, MEG-3_{Cterm} and MEG-3_{HMGL-}, *Y51F10.2* enrichment in P_4 averaged around ~2-fold (Figure 5A, D).

Enrichment of mRNAs in P granules can also be detected using an oligo-dT probe to detect polyadenylated mRNAs (Seydoux and Fire, 1994). In wild-type 28-cell stage embryos, strong poly-A signal is detected around the nucleus of the P_4 blastomere (Figure 5 – supplement 1C). This perinuclear signal was absent in *meg-3 meg-4* mutants as well as in embryos expressing MEG-3_{IDR}, MEG-3_{Cterm} and MEG-3_{HMGL-}. The lack of

polyA signal was particularly striking in the case of MEG-3_{IDR} and MEG-3_{HMGL-} since those variants assemble robust perinuclear condensates at this stage (Figure 3A).

Failure to efficiently segregate and stabilize maternal mRNAs in P blastomeres has been linked to the partial penetrance maternal effect sterility (~30%) of *meg-3meg-4* mutants (Lee et al., 2020). We observed similar levels of sterility in hermaphrodites derived from mothers expressing the MEG-3_{IDR}, MEG-3_{Cterm} and MEG-3_{HMGL-} (Figure 5 – supplement 1D). We conclude that the MEG-3 C-terminus, IDR and HMG-like motif are all required for efficient mRNA recruitment to P granules, which in turn is required for enrichment and stabilization in the P lineage and robust germ cell fate specification.

2.3 Discussion

In this study, we have examined the function of the MEG-3 IDR and C-terminus in P granule assembly using recombinant proteins *in vitro* and genome editing *in vivo*. Our main findings (summarized in Figure 6) suggest the following model for germ granule assembly: the MEG-3 C-terminus including the HMGL domain mediates MEG:PGL protein interactions that stimulate MEG-3 condensation on the surface of PGL condensates. The MEG-3 IDR recruits RNA and amplifies MEG-3 condensation. MEG-3 condensation in turn stabilizes PGL condensates in the posterior and protects mRNAs from degradation ensuring their efficient segregation to the germline founder cell P_4. Our findings suggest that germ granule assembly depends at least in part on protein-protein interactions that drive protein condensation independent of RNA.

Similarities and differences between *in vitro* and *in vivo* observations

In vitro condensation assays using purified proteins and RNAs are powerful tools to identify domains and molecular interactions that drive condensate self-assembly (Li et al., 2018; Lin et al., 2015; Saha et al., 2016). Because these assays do not reconstitute the cytoplasmic environment, however, results need to be interpreted with caution. In this study, we compared the *in vitro* and *in vivo* behavior of wild-type MEG-3 and derivatives. *In vitro* and *in vivo* observations were mostly consistent with some notable exceptions. For example, the MEG-3 C-terminus was more efficient at condensation than the MEG-3 IDR *in vivo*. This difference could also be observed *in vitro* when MEG-3 condensation was assayed in the presence of PGL-3, which solubilizes the MEG-3 IDR (Figure 2C). When MEG-3 was assayed alone, however, a difference between the MEG-3 C-terminus and IDR condensation could only be seen at the lowest concentration tested (Figure 2A). A second difference between *in vitro* and *in vivo* assays was observed when examining the HMGL motif. Mutations in this domain greatly disrupted MEG/PGL co-assembly *in vivo* but had no apparent effect in the *in vitro* co-assembly assay. Mutations in the HMGL domain did, however, lower MEG-3's affinity for the PGL proteins when assayed by GST pull down. The GST pull down assay is done under more stringent conditions (SDS and high salt) than the condensation assays and may therefore be better suited to reveal affinity differences sufficient to disrupt protein interactions in the crowded cellular milieu. We conclude that, while *in vitro* experiments are excellent tools to reveal self-assembly principles, condensation assays can lead to conclusions (e.g. HMGL is dispensable for MEG-3/PGL co-assembly) that do not necessarily hold *in vivo*.

Assembly of MEG-3/PGL co-condensates depends on interactions between MEG and PGL proteins and does not require RNA

The MEG-3 C-terminus is a 318 aa sequence with regions of predicted low disorder including an HMG-like motif. We have found that the MEG-3 C-terminus is sufficient to form condensates that dock on PGL droplets *in vitro* and *in vivo*. Docking of P bodies on stress granules has been proposed to involve RNA:RNA duplexes (Tauber et al., 2020). In contrast, we find that docking of MEG-3 condensates on PGL condensates does not require RNA *in vitro* and can occur in the absence of any visible RNA enrichment *in vivo*. Mutations in the HMGL domain prevent the association of MEG-3 and PGL condensates *in vivo* and lower the affinity of the MEG-3 C-terminus PGL proteins *in vitro*. Together, these observations strongly suggest that the association between MEG-3 and PGL condensates depends primarily on protein-protein interactions.

We previously showed that PGL-3 condensates stimulate MEG-3 condensation *in vitro* and *in vivo* (Wang et al., 2014, Putnam et al., 2019). Consistent with this, we report here that mutations in the HMGL domain that prevent MEG-3/PGL co-assembly also reduce MEG-3 condensation efficiency *in vivo*. An attractive possibility is that high affinity MEG-3/PGL binding, mediated in part by the HMGL motif, recruits MEG-3 molecules from the cytoplasm to the surface of PGL droplets, driving their condensation. We note that PGL molecules are unlikely to be the only binding partners that stimulate MEG condensation, since *pgl-1;pgl-3* mutants embryos still assemble

MEG granules that support RNA assembly (although not as robustly as wild-type; Lee et al., 2020).

Efficient MEG-3/PGL co-assembly correlates with stabilization of PGL droplets in germ plasm

We previously reported that enrichment of PGL droplets to the posterior of the zygote requires *meg-3* (Smith et al., 2016; Jennifer T Wang et al., 2014). Our new findings suggest that this activity is linked to MEG-3's ability to associate stably with the PGL interface. MEG-3_{Cterm}, which is sufficient for MEG-3/PGL co-assembly, is sufficient to localize PGL in zygotes. Conversely, MEG-3_{HMGL} condensates, which do not interact stably with PGL-3 condensates, fail to enrich PGL condensates in the posterior. PGL localization involves preferential growth and dissolution of PGL droplets in the anterior and posterior, respectively. One possibility is that tight binding of MEG condensates lowers the surface tension of PGL droplets allowing MEG/PGL co-assemblies in the posterior to grow at the expense of the less stable, "naked" PGL droplets in the anterior.

What enriches MEG-3 condensates in the posterior? We previously hypothesized that MEG-3 asymmetry is driven by a competition for RNA between the MEG-3 IDR and MEX-5, an RNA-binding protein that acts as an RNA sink in the anterior (Smith et al., 2016). Our finding that condensation of MEG-3_{Cterm} is restricted to the zygote posterior despite uniform distribution in the cytoplasm suggest that additional mechanisms acting on the MEG-3 C-terminus contribute to MEG-3 regulation in space. Consistent with this view, a recent study examining MEG-3 dynamics by single-molecule imaging (Wu et al.,

2019) found that the slowly-diffusing MEG-3 molecules that populate the MEG-3 gradient in the cytoplasm represent a distinct population of MEG-3 molecules from those that associate with PGL droplets. Although the MEG-3 cytoplasmic gradient does not contribute to P granule asymmetry directly, it may serve to maintain high levels of MEG-3 in P blastomeres to sustain PGL asymmetry through the P_4 stage. Consistent with this view, the MEG-$3_{Cterm,}$ which does not enrich in a gradient, is not sufficient to localize PGL in P blastomeres past the 4-cell stage.

MEG-3 condensation on PGL droplets creates a platform for RNA recruitment

The MEG-3 IDR binds RNA with high affinity *in vitro* but is not sufficient to enrich RNA *in vivo* despite forming condensates. RNA recruitment also requires the MEG-3 C-terminus including the HMG-like motif. These observations suggest that condensation of the MEG-3 C terminus is essential to build a protein scaffold that can support RNA recruitment *in vivo*. Separate domains for RNA binding and protein condensation have also been observed for other germ granule scaffolds. For example, the Balbiani body protein Xvelo uses a prion-like domain to aggregate and a separate RNA-binding domain to recruit RNA (Boke et al., 2016). Similarly, condensation of Drosophila Oskar does not require the predicted Oskar RNA-binding domain, although this domain augments condensation (Kistler et al., 2018). These observations parallel our findings with MEG-3 and contrast with recent findings reported for the stress granule scaffold G3BP. Condensation of G3BP *in vitro* requires RNA and two C-terminal RNA-binding domains. A N-terminal dimerization domain is also required but, unlike the prion-like domain of

Xvelo or the C-terminus of MEG-3, is not sufficient to drive condensation on its own. Dimerization of G3BP is thought to enhance LLPS indirectly by augmenting the RNA-binding valency of G3BP complexes. G3BP also contains an inhibitory domain that gates its RNA-binding activity and condensation at low RNA concentrations. This modular organization ensures that G3BP functions as a sensitive switch that initiates LLPS when sufficient RNA molecules are available to cross-link G3BP dimers into a large network (Guillén-Boixet et al., 2020; Yang et al., 2020). Stress granules are transient structures that form under conditions of general translational arrest where thousands of transcripts are released from ribosomes. In contrast, germ granules are long-lived structures that assemble in translationally-active cytoplasm and recruit only a few hundred specific transcripts (~500 in *C. elegans* embryos) (Jamieson-Lucy and Mullins, 2019; Lee et al., 2020; Trcek and Lehmann, 2019; Updike and Strome, 2010). One possibility is that protein-based condensation mechanisms may be better suited to assemble long-lived granules able to capture and retain rare transcripts. By concentrating IDRs with affinity for RNA, protein scaffolds could act as seeds for localized LLPS to amplify protein and RNA condensation. Consistent with this view, IDRs have been observed to undergo spontaneous LLPS in cells when artificially tethered to protein modules that self-assemble into large multimeric structures (Nakamura et al., 2019). A challenge for the future will be to understand the mechanisms that regulate the assembly and disassembly of protein scaffolds at the core of germ granules.

2.4 Methods

Worm handling, maternal-effect sterility counts - *C. elegans* was cultured at 20˚ C according to standard methods (Brenner, 1974). To measure maternal-effect sterility, ten gravid adults were picked to an OP50 plate and allowed to lay eggs for ~2 hours, then removed. Adult progeny were scored for empty uteri (white sterile phenotype) under a dissecting microscope.

Identification of MEG-3 HMG-like region - MEG-3 and MEG-4 protein sequences were aligned with HMG boxes from GCNA proteins of *Caenorhabditis* and example vertebrates along with the canonical HMG box of mouse SOX3 using MUSCLE (Edgar, 2004). Alignment was manually adjusted according to the published CGNA HMG Hidden Markov Model (Carmell et al., 2016). Amino acids were chosen for mutation based on conservation in nematodes.

CRISPR genome editing - Genome editing was performed in *C. elegans* using CRISPR/Cas9 as described in (Paix et al., 2017b). Strains used in this study along with guides and repair templates are listed in Supplementary Table 1. Some strains were generated in two steps. For example, MEG-3_{HMGL-} was generated by deleting the entire HMGL-like motif in a first step (JH3632), and inserting a modified HMG-like motif with the desired mutations in a second step (JH3861). Genome alterations were confirmed by Sanger sequencing and expression of tagged strains was verified by immunostaining and western blotting (Sup. Figure 3B).

Statistical Analysis and plotting - On all scatterplots, central bars indicate the mean and error bars indicate one standard deviation. Unless otherwise indicated,

differences within three or more groups were evaluated using a one-factor ANOVA and differences between two groups using an unpaired Student's t-test.

Confocal Imaging - Fluorescence confocal microscopy for figure 2C, supplementary figures 2A, 3B and 4A performed using a Zeiss Axio Imager with a Yokogawa spinning-disc confocal scanner. Fluorescence confocal microscopy for all other figures was performed using a custom built inverted Zeiss Axio Observer with CSU-W1 Sora spinning disk scan head (Yokogawa), 1X/2.8x relay lens (Yokogawa), fast piezo z-drive (Applied Scientific Instrumentation), and a iXon Life 888 EMCCD camera (Andor). Samples were illuminated with 405/488/561/637nm solid-state laser (Coherent), using a 405/488/561/640 transmitting dichroic (Semrock) and 624-40/692-40/525-30/445-45nm bandpass filter (Semrock) respectively. Images from either microscope were taken with using Slidebook v6.0 software (Intelligent Imaging Innovations) using a 40x-1.3NA/63X-1.4NA objective (Zeiss) depending on sample.

Immunostaining **-** Adult worms were placed into M9 on poly-l-lysine (0.01%) coated slides and squashed with a coverslip to extrude embryos. Slides were frozen by laying on aluminum blocks pre-chilled with dry ice for >5 min. Embryos were permeabilized by freeze-cracking (removal of coverslips from slides) followed by incubation in methanol at -20˚C for >15 min, and in acetone -20˚C for 10 min. Slides were blocked in PBS-Tween (0.1%) BSA (0.5%) for 30min at room temperature, and incubated with 50 ul primary antibody overnight at 4˚C in a humid chamber. For co-staining experiments, antibodies were applied sequentially (OLLAS before KT3, K76) to avoid cross-reaction. Antibody dilutions (in PBST/BSA): KT3 (1:10, DSHB), K76 (1:10

DSHB), Rat αOLLAS-L2 (1:200, Novus Biological Littleton, CO), Secondary antibodies were applied for 2 hr at room temperature. Samples were mounted Prolong Diamond Antifade Mountant or VECTASHIELD Antifade Mounting Media with DAPI. Embryos were staged using DAPI stained nuclei and 25 confocal slices spaced 0.18 microns apart and centered on the P cell nucleus were taken using a 63x objective. Unless otherwise indicated, images presented in figures are maximum projections.

Quantification of immunostaining images **-** All analysis was performed in ImageJ. For measurements of embryos/cells, confocal stacks were sum projected and the integrated density was measured within a region of interest. For measurements of condensate intensity, the 3D objects counter function was used on the full confocal stack confined to a region of interest drawn around the P cell and including objects on edges. The integrated density for all identified particles was summed to give the total intensity in condensates.

Single molecule fluorescence in situ hybridization (smFISH) **-** smFISH probes were designed using Biosearch Technologies's Stellaris Probe Designer, with the fluorophor Quasar670. For sample preparation, embryos were extruded from adults on poly-l-lysine (0.01%) slides and subjected to freeze-crack followed by methanol fixation at - 20˚ C for >15minutes. Samples were washed five times in PBS-Tween (0.1%) and fixed in 4% PFA (Electron Microscopy Science, No.15714) in PBS for one hour at room temperature. Samples were again washed four times in PBS-Tween (0.1%), twice in 2x SCC, and once in wash buffer (10% formamide, 2x SCC) before blocking in hybridization buffer (10% formamide, 2x SCC, 200 ug/mL BSA, 2 mM Ribonucleoside Vanadyl Complex, 0.2 mg/mL

yeast total RNA, 10% dextran sulfate) for >30 min at 37˚ C. Hybridization was then conducted by incubating samples with 50nM probe solutions in hybridization buffer overnight at 37˚ C in a humid chamber. Following hybridization, samples were washed twice in wash buffer at 37˚ C, twice in 2x SCC, once in PBS-Tween (0.1%) and twice in PBS. Samples were mounted Prolong Diamond Antifade Mountant.

Quantification of in situ hybridization images **-** All measurements were performed on a single confocal slice centered on the P cell nucleus in ImageJ. For early embryos where there is distinct punctate signal (1 and 4 cell stage Figure 5B,C, Figure 5 – figure 1 B), a region of interest was drawn, the Analyze Particles feature was used with a manual threshold to identify and measure the integrated density of the puncta. The raw integrated density for all particles in the region of interest was summed to give the total intensity of the mRNA in that region. For 28 cell embryos (Fig, 5D) a region of interest was drawn around the P_4 blastomere and the intensity of that region was divided by the intensity of a region of the same size in the anterior soma.

Western blotting of embryonic lysates - Worms were synchronized by bleaching to collect embryos, shaken approximately 20hrs in M9, then plating on large enriched peptone plates with a lawn of *E. Coli* NA22 bacteria. Embryos were harvested from young adults (66 hours after starved L1 plating) and sonicated in 2% SDS, 65 mM Tris pH 7, 10% glycerol with protease and phosphatase inhibitors. Lysates were spun at 14,000 rpm for 30 min at 4˚ C and cleared supernatants were transferred to fresh tubes. Lysates were run on 4-12% Bis-Tris pre-cast gels (Bio-Rad Hercules, CA). Western blot transfer was performed for 1 hr at 4°C onto PVDF membranes. Membranes were blocked

overnight and washed in 5% milk, 0.1% Tween-20 in PBS; primary antibodies were incubated overnight at 4˚ C; secondary antibodies were incubated for two hours at room temperature. Membranes were first probed for OLLAS then stripped by incubating in 62.5mM Tris HCl pH6.8, 2% SDS, 100mM ß-mercaptoethanol at 42˚ C. Membranes were then washed, blocked and probed for α-tubulin. Antibody dilutions in 5% milk/PBST: Rat α OLLAS-L2 (1:1000, Novus Biological Littleton, CO), Mouse α tubulin (1:1000, Sigma St. Louis, MO).

Expression and purification of MEG-3 His-tagged fusion proteins: MEG-3 full-length (aa1-862), IDR (aa1-544), Cterm (aa545-862), and HMGL- proteins were fused to an N-terminal 6XHis tag in pET28a and expressed and purified from inclusion bodies using a denaturing protocol (Lee et al., 2020)

Purification of MBP-tagged fusion proteins - MBP-TEV-PGL-3 was expressed and purified as described (Putnam et al., 2019) with the following modifications: MBP was cleaved using homemade TEV protease instead of commercial. A plasmid expressing 8X-His-TEV-8X-Arg tag protease was obtained from Addgene and purified according to the published protocol (Tropea et al., 2009). Before loading cleaved PGL-3 protein on to a heparin affinity matrix, cleaved MBP-6X-His and 6X-His-TEV protease were removed using a HisTRAP column (GE Healthcare).

Protein labeling - Proteins were labeled with succinimidyl ester reactive fluorophores from Molecular Probes (Alexa Fluor™ 647 or DyLight™ 488 NHS Ester) following manufacturer instructions. Free fluorophore was eliminated by passage through three Zeba™ Spin Desalting Columns (7K MWCO, 0.5 mL) into protein storage

buffer. The concentration of fluorophore-labeled protein was determined using fluorophore extinction coefficients measured on a Nanodrop ND-1000 spectrophotometer. Labeling reactions resulted in ~ 0.25-1 label per protein. Aliquots were snap frozen and stored. In phase separation experiments, fluorophore-labeled protein was mixed with unlabeled protein for final reaction concentrations of 25-100 nM of fluorophore labeled protein.

In vitro transcription and labeling of RNA - mRNAs were transcribed using T7 mMessageMachine (Thermofisher) using manufacturer's recommendation as described (Lee et al., 2020). Template DNA for transcription reactions was obtained by PCR amplification from plasmids. Free NTPs and protein were removed by lithium chloride precipitation. RNAs were resuspended in water and stored at −20°C. The integrity of RNA products was verified by agarose gel electrophoresis.

In vitro condensation experiments and analysis - Protein condensation was induced by diluting proteins out of storage buffer into condensation buffer containing 25 mM HEPES (pH 7.4), salt adjusted to a final concentration of 150 mM (37.5 mM KCl, 112.5 mM NaCl), and RNA. For MEG-3 and PGL-3 co-condensate experiments with RNA, we used 150 nM MEG-3, 1.8 µM PGL-3 and 20 ng/µL RNA. For co-assembly experiments in the absence of RNA, we used 150 nM MEG-3, 5 µM PGL-3. MEG-3 and PGL-3 solutions contained 25 nM fluorescent trace labels with either 488 or 647 (indicated in figure legends). MEG-3 condensation reactions were incubated at room temperature for 30 min before spotting onto a No. 1.5 glass bottom dish (Mattek) and imaged using a 40x oil objective (Figure 2A). MEG-3 and PGL-3 co-condensate were imaged using thin

chambered glass slides (Erie Scientific Company 30-2066A) with a coverslip (Figure 2C). Images are single planes acquired using a 40x oil objective over an area spanning 171 x 171 µm.

To quantify the relative intensity of MEG-3 in condensates, a mask was created by thresholding images, filtering out objects of less than 4 pixels to minimize noise, applying a watershed filter to improve separation of objects close in proximity, and converting to a binary image by the Otsu method using the nucleus counter cookbook plugin. Minimum thresholds were set to the mean intensity of the background signal of the image plus 1-2 standard deviations. The maximum threshold was calculated by adding 3-4 times the standard deviation of the background. Using generated masks, the integrated intensity within each object was calculated. To remove non-specific background signal the mean intensity of an image field in the absence of the labeled component was subtracted from each pixel yielding the total intensity of each object. The relative intensity in each condensate was normalized to the mean intensity of WT MEG-3. Each data point represents the average of 3 experimental replicates. Each replicate contained 4 images each spanning an area of 316.95 x 316.95 µm.

RNA binding by fluorescence filter binding - Proteins were step-dialyzed from 6M Urea into 4.5M Urea, 3M Urea, 1.5M Urea, and 0M Urea in MEG-3 Storage Buffer (25 mM HEPES, pH 7.4, 1M NaCl, 6 mM ß-mercaptoethanol, 10% Glycerol). RNA binding reactions consisted of 50 nM 3' Fluorescein-labeled 30U RNA oligonucleotides incubated with protein for 30 min at room temperature (final reaction conditions 3.75 mM HEPES, 150mM NaCl, 0.9mM, 0.9mM ß-mercaptoethanol, 1.5% glycerol, 10mM Tris HCl).

Fluorescence filter binding protocol was adapted from a similar protocol using radiolabeled RNA (Rio, 2012). Briefly, a pre-wet nitrocellulose was placed on top of Hybond-N+ membrane in a dot-blot apparatus, reactions were applied to the membranes, then washed 2x with 10mM Tris HCl. Membranes were briefly dried in air, then imaged using a typhoon FLA-9500 with blue laser at 473 nm. Fraction of RNA bound for each reaction was calculated by dividing the fluorescence signal on the nitrocellulose membrane by the total signal from both membranes. K_d was calculated by plotting the bound fraction of RNA as a function of protein concentration and fitting to the following equation in Prism8 where P is the protein concentration in nM, B is the bound fraction of RNA with non-specific binding subtracted, B_{max} is the maximum specific binding, K_d is the concentration needed to achieve a half-maximum binding at equilibrium, and h is the Hill slope.

$$B = \frac{B_{max} \times P^h}{K_d^h + P^h}$$

GST pull-downs - GST fusion proteins were cloned into pGEX6p1 (GE Healthcare, Pittsburgh, PA). MBP fusion proteins were cloned into pJP1.09, a Gateway-compatible pMAL-c2x (Pellettieri et al., 2003). Proteins were expressed in Rosetta™ *E. coli* BL21 cells grown for approximately four hours at 37˚ C then induced with 1mM IPTG and grown overnight at 16˚ C. 200 mg of bacterial pellet of GST fusion proteins was resuspended in 50mM HEPES, 1 mM EGTA, 1 mM $MgCl_2$, 500 mM KCl, 0.05% NP40, 10% glycerol, pH 7.4 with protease and phosphatase inhibitors, lysed by sonication, and bound to magnetic GST beads. Beads were washed and incubated with MBP fusion proteins at 4°C for 1 hr

in the same buffer as for lysis. After washing, beads were eluted by boiling and eluates were loaded on SDS-PAGE. Western blot transfer was performed for 1 hr at 4°C onto PVDF membranes. Membranes were blocked and washed in 5% milk, 0.1% Tween-20 in PBS and incubated with HRP conjugate antibodies. Antibody dilutions in 5% milk/PBST: anti-MBP HRP conjugated, 1:50,000 (NEB, and anti-GST HRP conjugates, 1:2,000 (GE Healthcare). Scanned western blot films were quantified using the gel analysis tool in ImageJ.

2.5 Acknowledgements

I would like to thank Andrea Putnam for contributing Figure 2 A-C and Dominique Rasoloson for contributing Figure 2 H and Figure 2 – figure supplement 1 D. I have also greatly appreciated their feedback and insight throughout many discussions and the writing of this work.

2.5 Figures

Figure 1 - Domain organization of MEG-3

A. MEG-3 amino-acid sequence (N to C-terminus) on the X-axis is plotted against disorder score on the Y-axis as predicted by ANCHOR2 (blue) and IUPred2 (red) (Mészáros et al., 2018)with a range from zero to one, where one is the most disordered.

B. Schematics of wild-type MEG-3 and four MEG-3 variants analyzed in this study. Amino acid positions are aligned with A. The disordered region (blue), C-terminus (grey), and HMG-like motif (green) are indicated. Magenta bars (alanine substitutions) correspond to four conserved residues in the HMG-like motif shaded in magenta in C.

C. Alignment of the HMG-like motif in MEG-3 and MEG-4 with the HMG-like motif in GCNA proteins Carmell et al., 2016 and the canonical HMG box of mouse SOX3. Amino acids predicted to form alpha-helices are highlighted in yellow (Drozdetskiy et al., 2015). Bold indicates positions with greater than 70% amino acid similarity. Magenta bars indicate residues mutated to alanine in MEG-3_{HMGL-}.

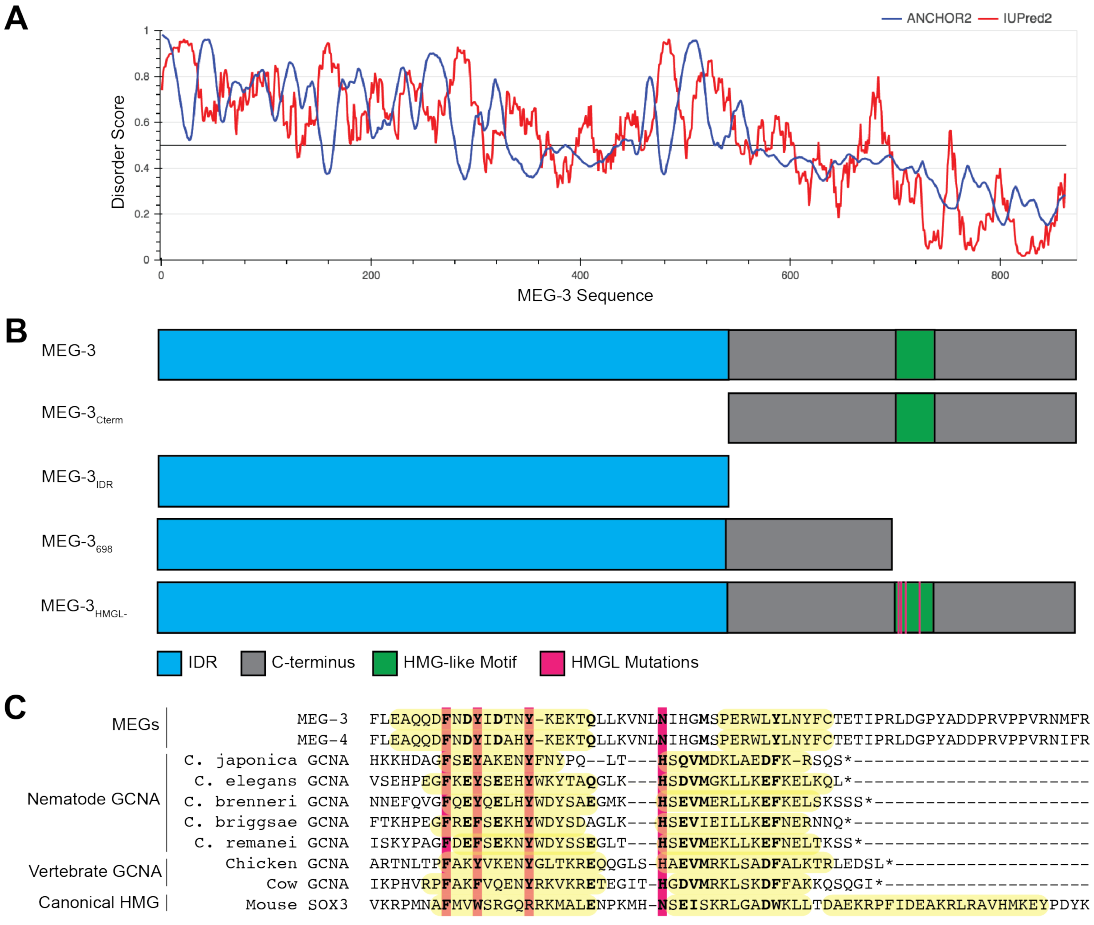
A
ANCHOR2
IUPred2
Disorder Score
MEG-3 Sequence
B
MEG-3
MEG-3Cterm
MEG-3IDR
MEG-3698
MEG-3HMGL-
IDR
C-terminus
HMG-like Motif
HMGL Mutations
C
MEGs
Nematode GCNA
Vertebrate GCNA
Canonical HMG
MEG-3 FLEAQQDFNDYIDTNY-KEKTQLLKVNLNIHGMSPERWLYLNYFCTETIPRLDGPYADDPRVPPVRNMFR
MEG-4 FLEAQQDFNDYIDAHY-KEKTQLLKVNLNIHGMSPERWLYLNYFCTETIPRLDGPYADDPRVPPVRNIFR
C. japonica GCNA HKKHDAGFSEYAKENYFNYPQ--LT---HSQVMDKLAEDFK-RSQS*----------
C. elegans GCNA VSEHPEGFKEYSEEHYWKYTAQGLK---HSDVMGKLLKEFKELKQL*----------
C. brenneri GCNA NNEFQVGFQEYQELHYWDYSAEGMK---HSEVMERLLKEFKELSKSSS*----------
C. briggsae GCNA FTKHPEGFREFSEKHYWDYSDAGLK---HSEVIEILLKEFNERNNQ*----------
C. remanei GCNA ISKYPAGFDEFSEKNYWDYSSEGLT---HSEVMEKLLKEFNELTKSS*----------
Chicken GCNA ARTNLTPFAKYVKENYGLTKREQQGLS-HAEVMRKLSADFALKTRLEDSL*----------
Cow GCNA IKPHVRPFAKFVQENYRKVKRETEGIT-HGDVMRKLSKDFFAKKQSQGI*----------
Mouse SOX3 VKRPMNAFMVWSRGQRRKMALENPKMH-NSEISKRLGADWKLLTDAEKRPFIDEAKRLRAVHMKEYPDYK

Figure 2 - *in vitro* characterization of wild-type MEG-3 and variants

A. Representative photomicrographs of Alexa647 trace-labeled MEG-3 and MEG-3 variants, at increasing concentration from left to right, in condensation buffer with 20 ng/µL nos-2 mRNA. Quantification of MEG-3 in condensates is shown in B.

B. Total intensity of MEG-3 in condensates (Y axis, normalized to 1 µM full length MEG-3) plotted against MEG-3 concentration (X axis). Condensates were assembled as in A. Dots indicate the mean of 3 replicates and errors bars the standard deviation.

C. Representative photomicrographs of MEG-3 and MEG-3 derivatives (trace labeled with Alexa647) incubated for 30 mins with PGL-3 (trace labeled with Alexa488) with and without *nos-2* mRNA in condensation buffer.

D-G. RNA binding curves for MEG-3 (D), MEG-3_{Cterm} (E), MEG-3_{IDR} (F), and MEG-3_{HMGL-} (G). Protein concentration is plotted on the X-axis. The ratio of bound RNA to total RNA, normalized to the ratio at the maximum concentration is plotted on the Y-axis. Dots indicate the mean of four replicates and the error bars the standard deviation (not shown when <0.06). Curve fit and K_d calculation based on specific binding with Hill slope (Methods).

H. Analysis of GST::MEG-3_{Cterm} and MBP::PGL-1 and MBP::PGL-3 interactions by GST-pull down assay with MBP and MBP::PAA-1 as negative controls. Western blots of E. coli lysates expressing the indicated MBP-fusions before (Input) and after immobilization on magnetic beads with the indicated GST-fusions. Western blot of GST-fusions is shown below. See Figure 2 - supplement 1C for quantification of additional replicates.

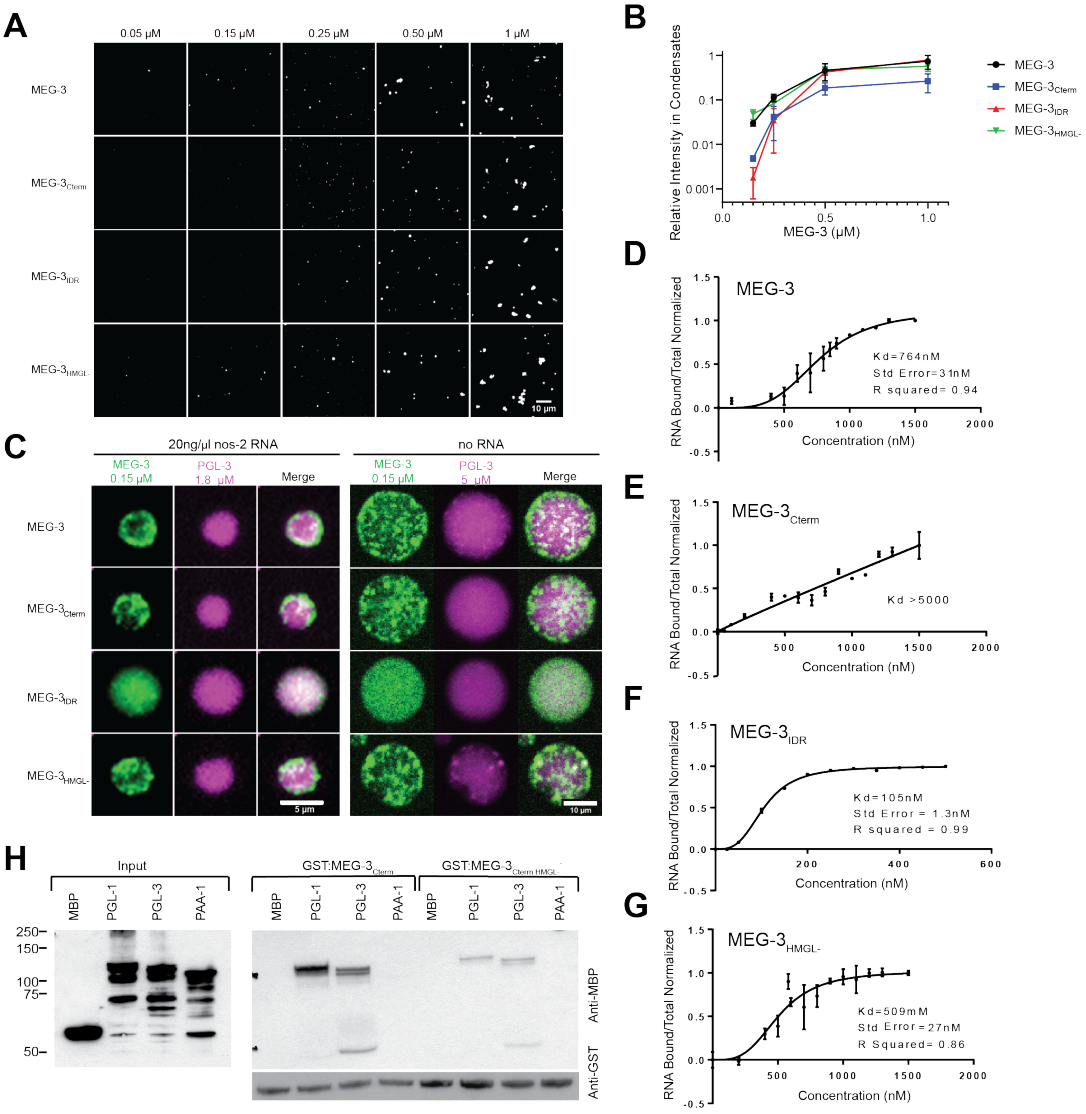
A
0.05 µM
0.15 µM
0.25 µM
0.50 µM
1 µM
MEG-3
MEG-3Cterm
MEG-3IDR
MEG-3HMGL-
10 µm
B
Relative Intensity in Condensates
MEG-3 (µM)
MEG-3
MEG-3Cterm
MEG-3IDR
MEG-3HMGL-
C
20ng/µl nos-2 RNA
no RNA
MEG-3 0.15 µM
PGL-3 1.8 µM
PGL-3 5 µM
Merge
5 µm
10 µm
D
MEG-3
Kd=764nM
Std Error=31nM
R squared= 0.94
RNA Bound/Total Normalized
Concentration (nM)
E
MEG-3Cterm
Kd >5000
F
MEG-3IDR
Kd=105nM
Std Error = 1.3nM
R squared = 0.99
G
MEG-3HMGL-
Kd=509mM
Std Error=27nM
R Squared= 0.86
H
Input
GST:MEG-3Cterm
GST:MEG-3Cterm HMGL-
MBP
PGL-1
PGL-3
PAA-1
250
150
100
75
50
Anti-MBP
Anti-GST

Figure 2 - supplement 1 – Supplementary *in vitro* characterization of wild-type MEG-3 and variants

A. Representative photomicrographs of Alexa488 trace-labeled MEG-3 and MEG-3 derivatives in condensation buffer with 20 ng/µL *Y51F10.2* mRNA.

B. RNA binding curve for MEG-3_{698}. Protein concentration is plotted on the X-axis. The ratio of bound RNA to total RNA, normalized to the ratio at the maximum concentration is plotted on the Y-axis. Dots indicate the mean of three replicates and the error bars the standard deviation. Curve fit and K_d calculation based on specific binding with Hill slope (Methods)

C. Scatterplot showing the ratio of the indicated MBP fusions to GST:MEG-$3_{Cterm\ HMGL-}$ normalized to the ratio of the same MBP fusion to GST:MEG-3_{Cterm} from the same experiment. Each dot represents an independent pull-down experiment. P values indicated above were calculated by a paired ratio t-test of the GST:MEG-3_{Cterm} and GST:MEG-$3_{Cterm\ HMGL-}$ ratios before normalization.

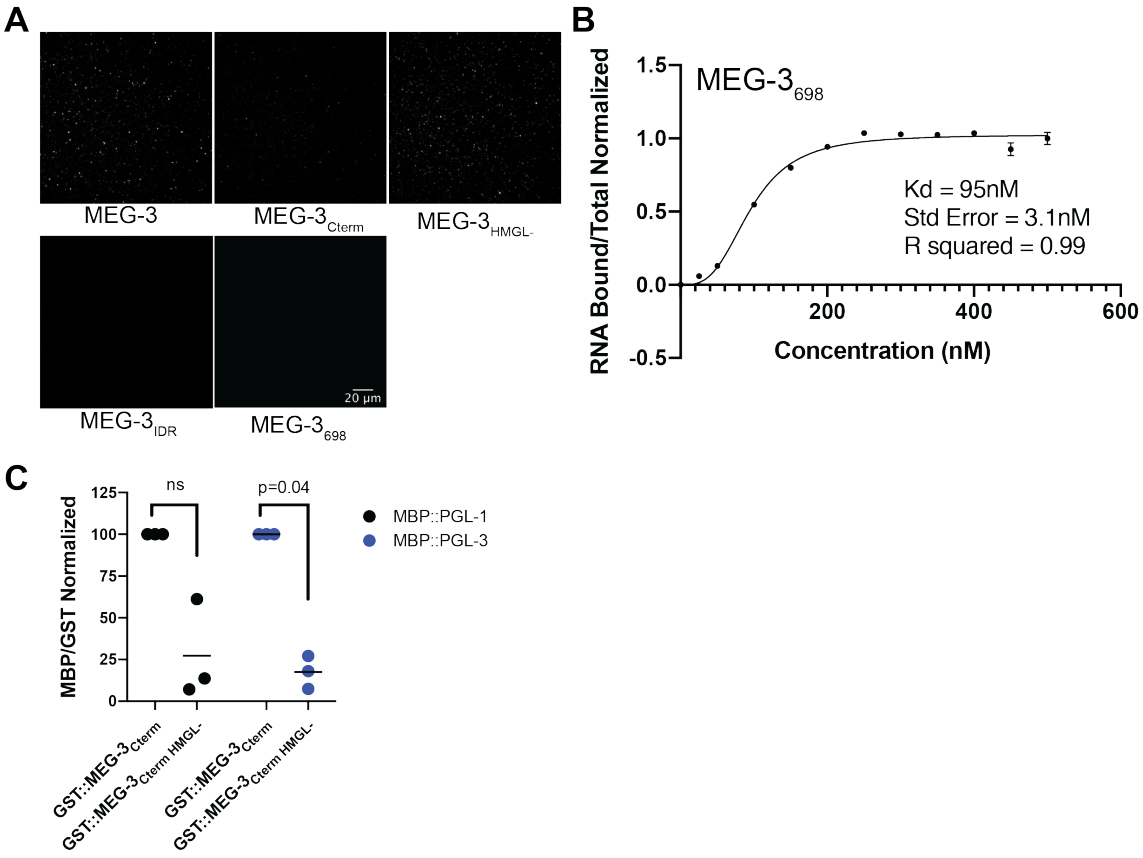
A
MEG-3
MEG-3Cterm
MEG-3HMGL-
MEG-3IDR
MEG-3698
20 µm
B
MEG-3698
RNA Bound/Total Normalized
1.5
1.0
0.5
0.0
-0.5
200
400
600
Concentration (nM)
Kd = 95nM
Std Error = 3.1nM
R squared = 0.99
C
MBP/GST Normalized
125
100
75
50
25
0
ns
p=0.04
MBP::PGL-1
MBP::PGL-3
GST::MEG-3Cterm
GST::MEG-3Cterm HMGL-
GST::MEG-3Cterm
GST::MEG-3Cterm HMGL-

Figure 3 - Localization of wild-type MEG-3 and variants in early embryos

A. Representative photomicrographs of embryos immunostained for OLLAS and expressing the indicated OLLAS-tagged MEG-3 derivatives. Last row shows *meg-3 meg-4* embryos as negative control for OLLAS staining. Images are representative of each stage as indicated (Before and after polarization are 1-cell stage zygotes). A minimum of 3 embryos from two independent experiments were analyzed for each stage. Scale bars are 1µm. All images are normalized to same fluorescent intensity range except for the last column showing high magnification views of P_4 from 28-cell stage image adjusted to highlight MEG-3 granules.

B. Scatterplot showing the number of MEG-3 condensates in P_2 in embryos expressing the indicated MEG-3 derivatives. Each dot represents an embryo.

C. Scatterplot showing enrichment of MEG-3 in P_2 over the somatic blastomere EMS, calculated by dividing the average intensity in P_2 by the average intensity in EMS. Each dot represents an embryo also included in the analysis shown in B.

D. Scatterplot showing the fraction the MEG-3 signal localized to condensates over total signal in P_2. Each dot represents an embryo also included in the analysis in B.

E. Summary of MEG-3 (green) distribution derived from data presented in A. Horizontal lines and arrows denote one cell division. Note that wild-type MEG-3 and MEG-3_{HMGL-} are rapidly turned over in somatic cells after the 4-cell stage (grey cells) as shown in Figure 3 - supplement 1C.

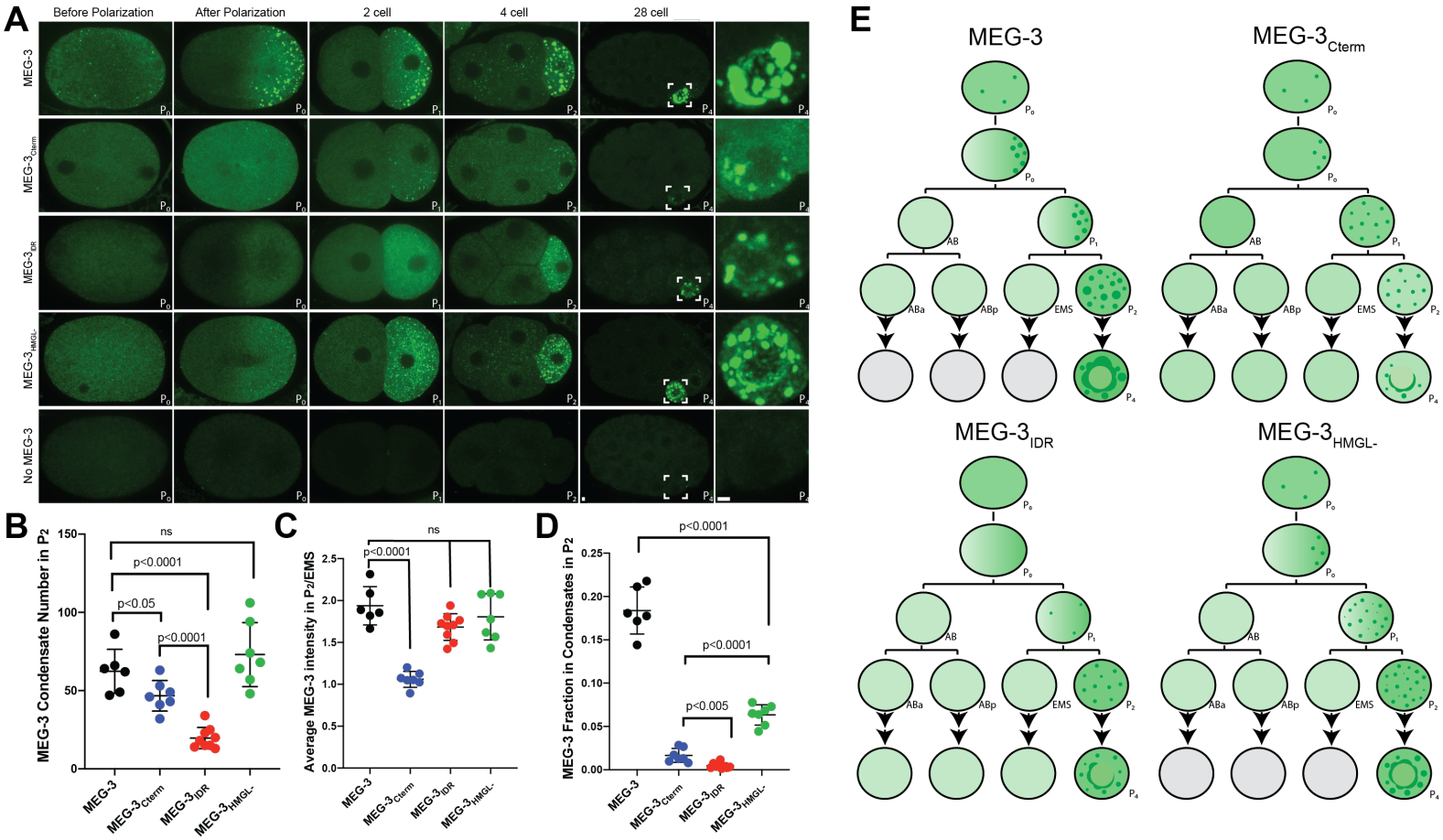
A
Before Polarization
After Polarization
2 cell
4 cell
28 cell
MEG-3
MEG-3Cterm
MEG-3IDR
MEG-3HMGL-
No MEG-3
B
MEG-3 Condensate Number in P2
ns
p<0.0001
p<0.05
p<0.0001
C
Average MEG-3 intensity in P2/EMS
ns
p<0.0001
D
MEG-3 Fraction in Condensates in P2
p<0.0001
p<0.0001
p<0.005
E
MEG-3
MEG-3Cterm
MEG-3IDR
MEG-3HMGL-
AB
P1
ABa
ABp
EMS
P2
P4

Figure 3 - supplement 1 – Additional characterization of wild-type MEG-3 and variants in embryos

A. Representative photomicrographs of two-cell embryos expressing the indicated MEG-3 derivatives and immunostained for MEG-3 (anti-OLLAS antibody) and PGL-1 (anti-PGL-1 antibody).

B. Representative photomicrographs of sum projections of 28-cell stage embryos expressing the indicated MEG-3 derivatives and immunostained for MEG-3.

C. Westerns of mixed-stage embryos (1-100 cell stage) harvested from synchronized worms expressing the indicated OLLAS-tagged MEG-3 derivatives.

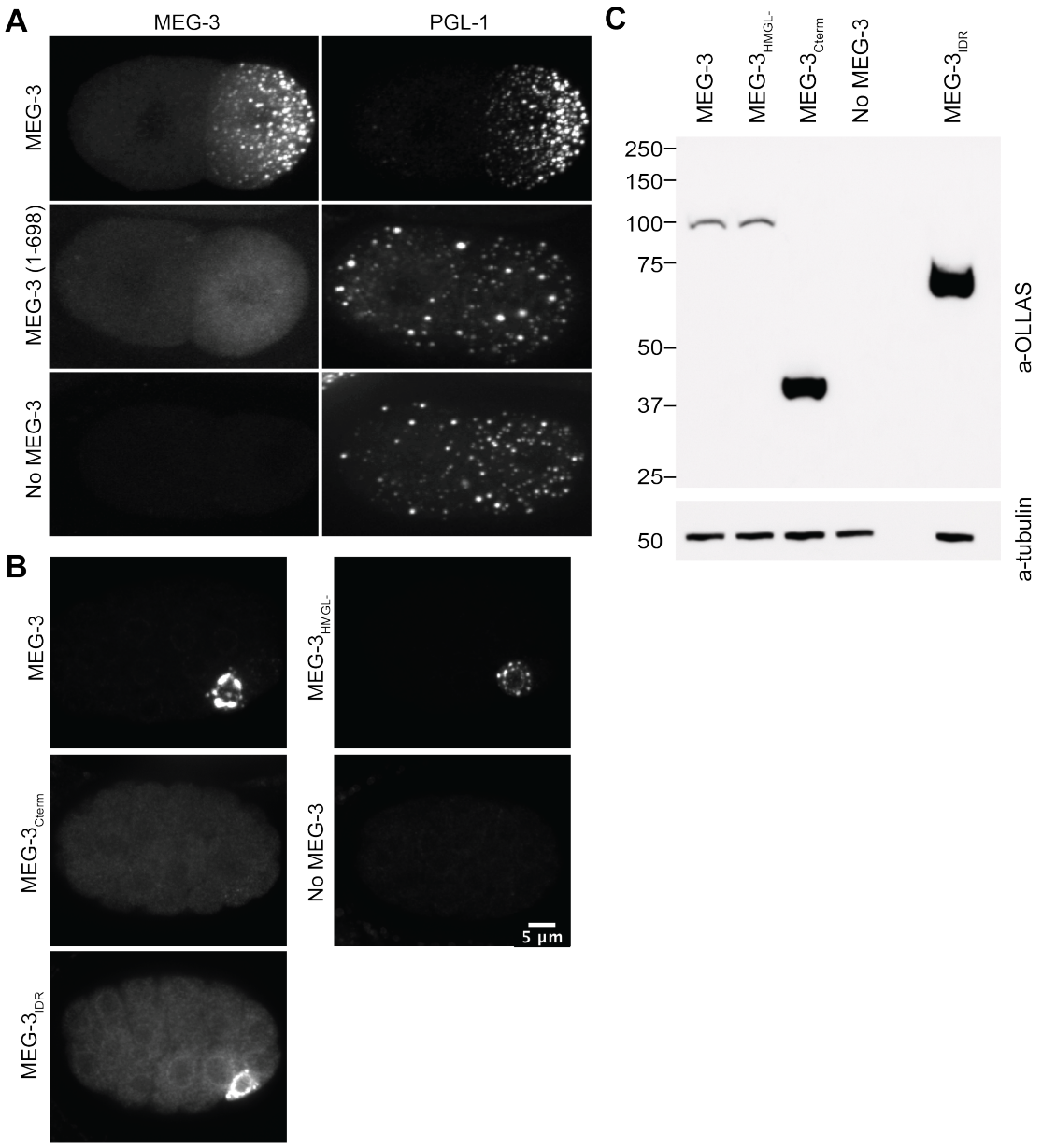
A
MEG-3
PGL-1
MEG-3
MEG-3 (1-698)
No MEG-3
B
MEG-3
MEG-3HMGL-
MEG-3Cterm
No MEG-3
MEG-3IDR
5 µm
C
MEG-3
MEG-3HMGL-
MEG-3Cterm
No MEG-3
MEG-3IDR
250
150
100
75
50
37
25
50
a-OLLAS
a-tubulin

Figure 4 - Localization of PGL-3 relative to wild-type MEG-3 and variants in two cell embryos

A. Representative photomicrographs of two-cell embryos expressing the indicated MEG-3 mutants and immunostained for MEG-3 (anti-OLLAS antibody) and PGL-3 (anti-PGL-3 antibody). Scale bar is 5 μm.

B. High magnification photomicrographs of individual MEG-3/PGL-3 assemblies in embryos expressing the indicated MEG-3 derivatives. White color in the merge indicates overlap. Scale bar is 1μm.

C. Scatterplot of the enrichment of PGL-3 in P_1 calculated by dividing the average intensity in P_1 by the average intensity in AB. Each dot represents an embryo.

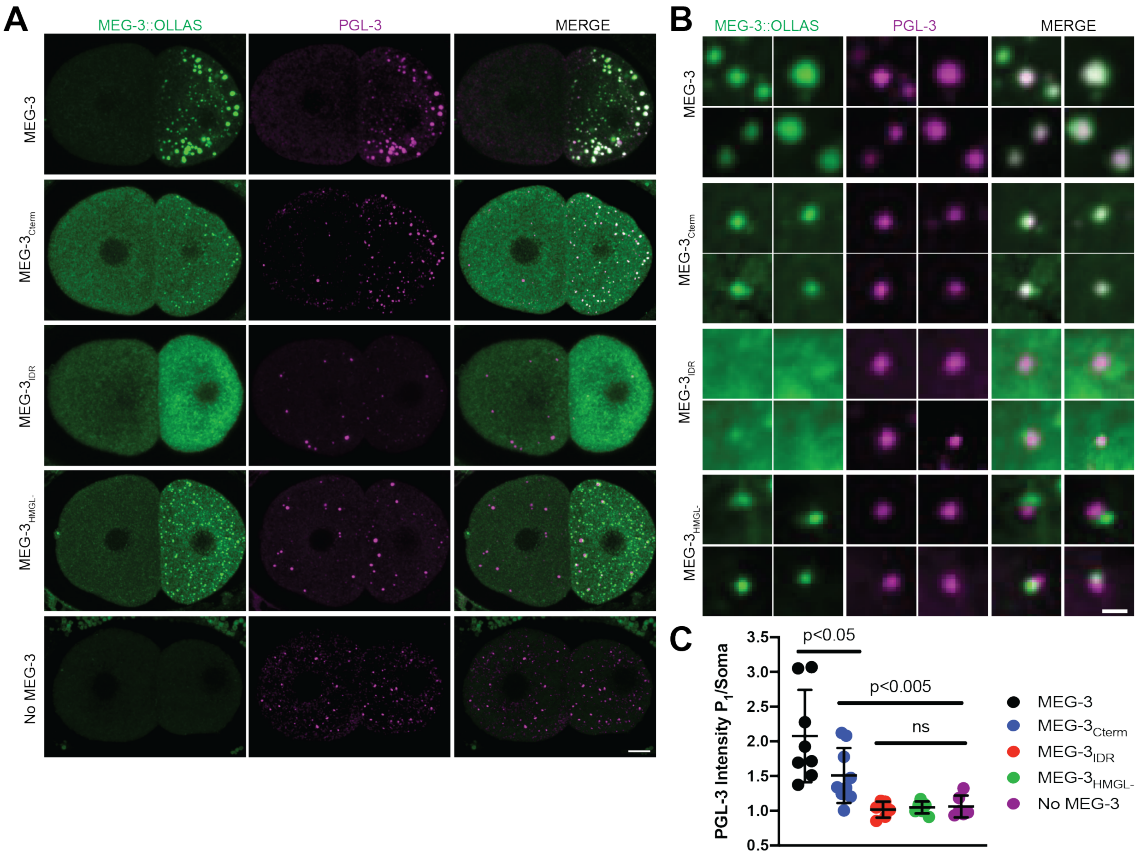
A
MEG-3::OLLAS
PGL-3
MERGE
MEG-3
MEG-3Cterm
MEG-3IDR
MEG-3HMGL-
No MEG-3
B
MEG-3::OLLAS
PGL-3
MERGE
MEG-3
MEG-3Cterm
MEG-3IDR
MEG-3HMGL-
C
PGL-3 Intensity P1/Soma
3.5
3.0
2.5
2.0
1.5
1.0
0.5
p<0.05
p<0.005
ns
MEG-3
MEG-3Cterm
MEG-3IDR
MEG-3HMGL-
No MEG-3

Figure 4 - supplement 1 - Localization of PGL-3 relative to wild-type MEG-3 and variants in P_4 blastomeres

A. Representative photomicrographs of a single confocal slice centered on the P_4 blastomere nucleus of embryos expressing the indicated MEG-3 mutants and immunostained for MEG-3 (anti-OLLAS antibody) and PGL-3 (anti-PGL-3 antibody). Note colocalization of MEG-3_{Cterm} and PGL-3. MEG-3_{Cterm} is present at lower level in P_4 compared to other MEG-3 derivatives, consistent with lack of enrichment in germ plasm starting in the 1-cell stage (Figure 3).

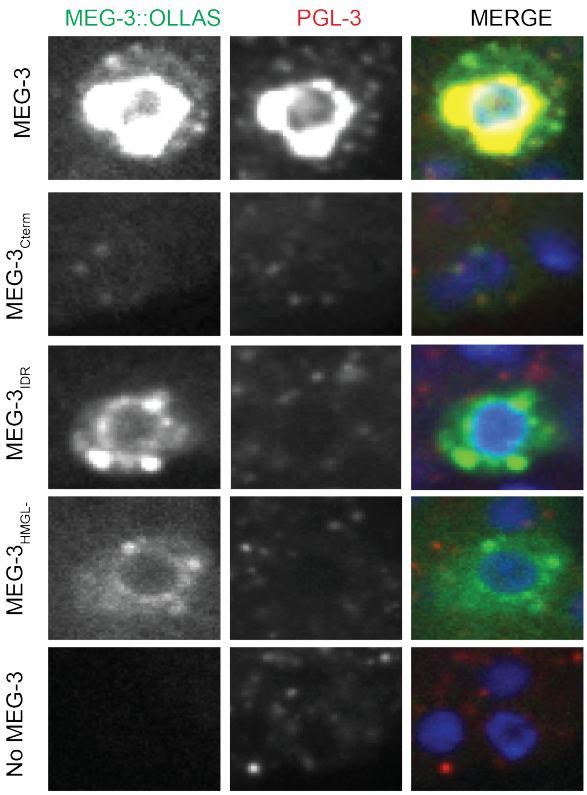
MEG-3::OLLAS
PGL-3
MERGE
MEG-3
MEG-3Cterm
MEG-3IDR
MEG-3HMGL-
No MEG-3

Figure 5 - Distribution of *Y51F10.2* mRNA in embryos expressing wild-type MEG-3 and variants

A. Representative photomicrographs of single confocal slices of fixed embryos expressing the indicated MEG-3 variants and hybridized to fluorescent probes complementary to the P granule-enriched mRNA *Y51F10.2* (white signal).

B. Scatterplot showing the ratio of *Y51F10.2* to *T26A5.2* mRNA signal in P_0 and P_2 embryos expressing the indicated MEG-3 derivatives. Each dot represents an embryo. See Figure 5 – supplement 1 for *T26A5.2* mRNA localization and levels

C. Scatterplot showing enrichment of *Y51F10.2* mRNA in P_2 relative to somatic blastomeres in embryos expressing the indicated MEG-3 derivatives. Each dot represents an embryo (Methods).

D. Scatterplot showing enrichment of *Y51F10.2* mRNA in P_4 relative to somatic blastomeres in embryos expressing the indicated MEG-3 derivatives. Each dot represents an embryo (Methods).

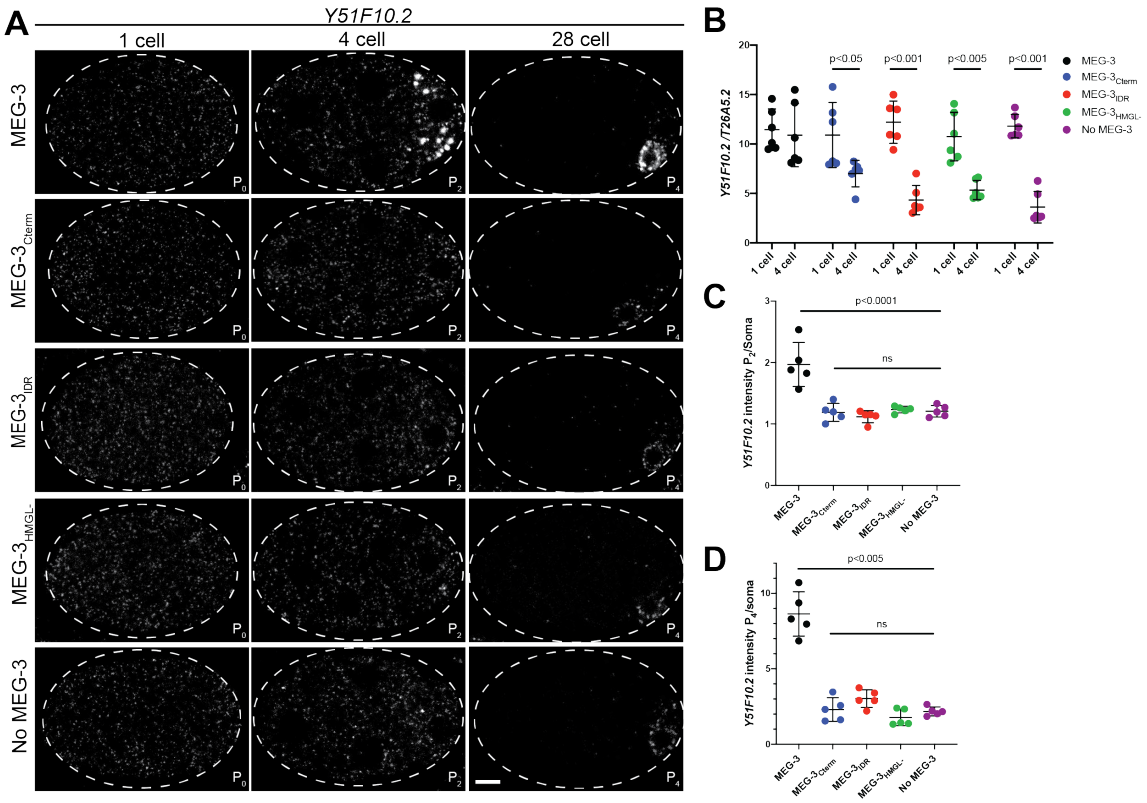
A
Y51F10.2
1 cell
4 cell
28 cell
MEG-3
MEG-3Cterm
MEG-3IDR
MEG-3HMGL-
No MEG-3
P0
P2
P4
B
Y51F10.2 /T26A5.2
p<0.05
p<0.001
p<0.005
p<0.001
MEG-3
MEG-3Cterm
MEG-3IDR
MEG-3HMGL-
No MEG-3
1 cell
4 cell
C
Y51F10.2 intensity P2/Soma
p<0.0001
ns
D
Y51F10.2 intensity P4/Soma
p<0.005
ns

Figure 5 - supplement 1 - Distribution of T26A5.2 and polyadenylated mRNAs in embryos expressing wild-type MEG-3 and variants

A. Representative photomicrographs of single confocal slices of fixed embryos expressing the indicated MEG-3 variants and hybridized to fluorescent probes complementary to the mRNA *T26A5.2*. Images are of the same embryo and confocal slice as Figure 5A.

B. Scatterplot of the intensity the *T26A5.2* mRNA signal in P_0 and P_2 embryos expressing the indicated MEG-3 derivatives. Each dot represents an embryo analyzed in Figure 5B.

C. Representative photomicrographs of single confocal slices of fixed embryos expressing the indicated MEG-3 variants and hybridized to oligo-dT fluorescent probes to detect polyadenylated mRNAs.

D. Plot of the percentage of sterile worms from mothers expressing the indicated MEG-3 derivatives raised at 20˚. Each dot represents the 2-hour brood of 10 mothers (Methods). Total number of worms scored is shown above.

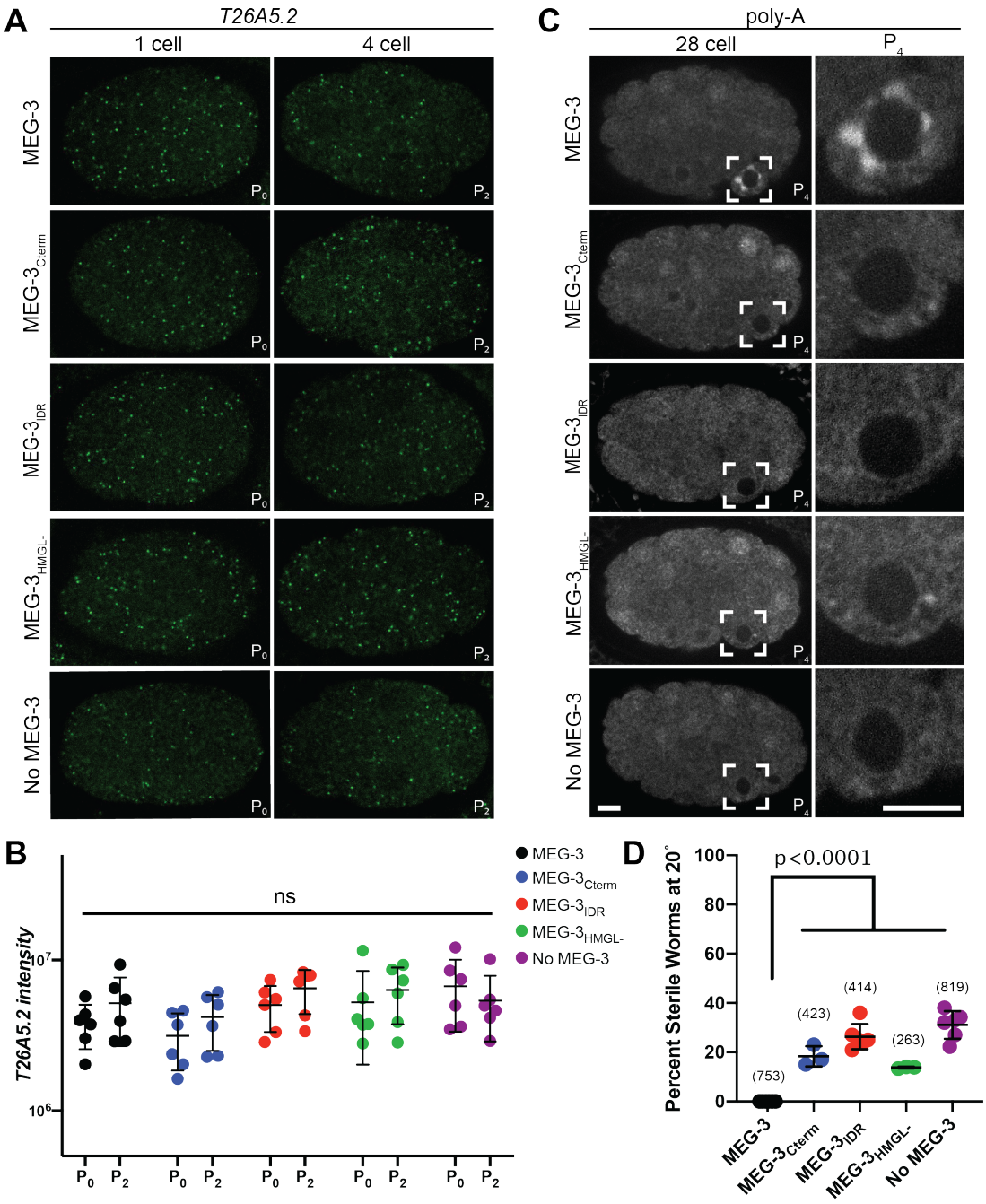
A
T26A5.2
1 cell
4 cell
MEG-3
MEG-3Cterm
MEG-3IDR
MEG-3HMGL-
No MEG-3
P0
P2
C
poly-A
28 cell
P4
B
ns
T26A5.2 intensity
10^7
10^6
MEG-3
MEG-3Cterm
MEG-3IDR
MEG-3HMGL-
No MEG-3
D
p<0.0001
Percent Sterile Worms at 20˚
100
80
60
40
20
0
(753)
(423)
(414)
(263)
(819)
MEG-3
MEG-3Cterm
MEG-3IDR
MEG-3HMGL-
No MEG-3

Figure 5 - supplement 2 - Distribution of *nos-2* mRNA in embryos expressing wild-type MEG-3 and variants

A. Representative photomicrographs of single confocal slices of fixed embryos expressing the indicated MEG-3 variants and hybridized to fluorescent probes complementary to the P granule-enriched mRNA *nos-2* (white signal).

B. Scatterplot showing the ratio of *nos-2* to *T26A5.2* mRNA signal in P_0 and P_2 embryos expressing the indicated MEG-3 derivatives. Each dot represents an embryo.

C. Scatterplot of the intensity the *T26A5.2* mRNA signal in P_0 and P_2 embryos expressing the indicated MEG-3 derivatives. Each dot represents an embryo analyzed in B

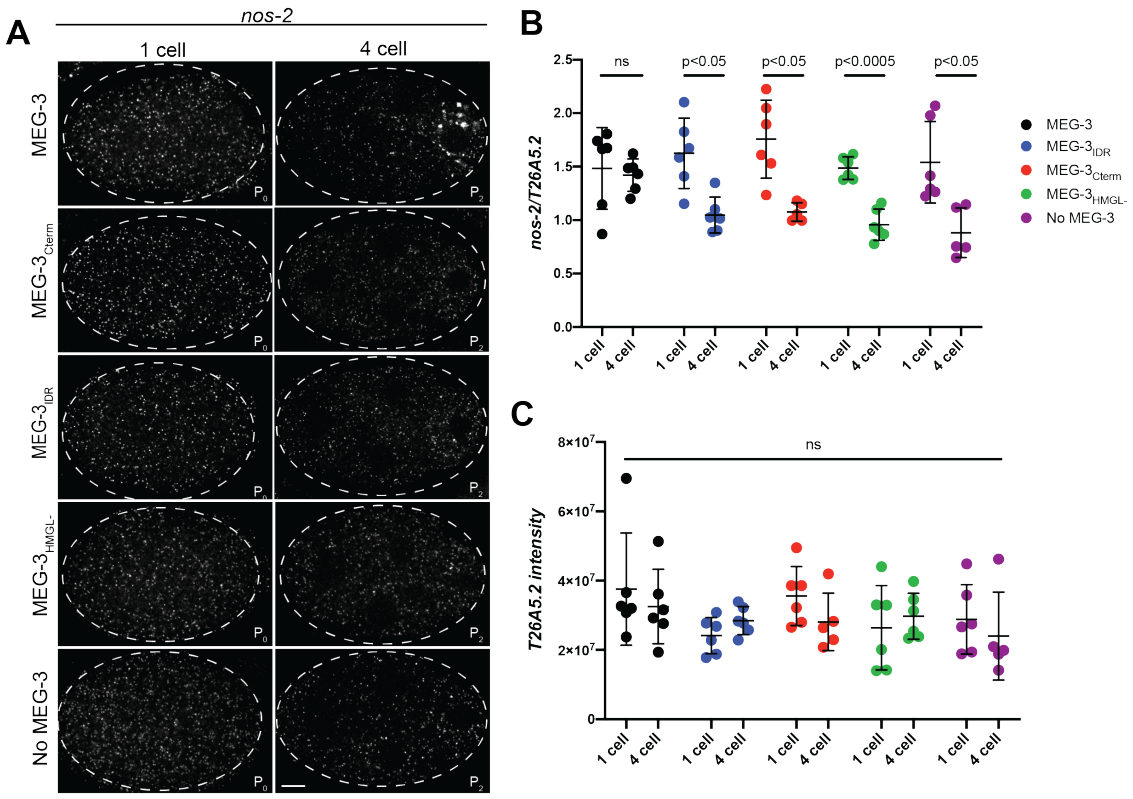
A
nos-2
1 cell
4 cell
MEG-3
MEG-3Cterm
MEG-3IDR
MEG-3HMGL-
No MEG-3
P0
P2
B
nos-2/T26A5.2
ns
p<0.05
p<0.05
p<0.0005
p<0.05
1 cell
4 cell
MEG-3
MEG-3IDR
MEG-3Cterm
MEG-3HMGL-
No MEG-3
C
T26A5.2 intensity
ns

Figure 6 - Diagram summarizing the distributions of MEG-3 and PGL-3 condensates and Y51F10.2 mRNA in P blastomeres.

A. In wild-type, MEG-3 is recruited to the surface of PGL droplets by its C-terminus while the MEG-3 IDR enriches RNA to the condensates. MEG-3_{IDR} does not interact with PGL efficiently and forms fewer condensates that do not enrich RNA. The MEG-3_{Cterm} is recruited to the surface of PGL droplets but, lacking the IDR, cannot enrich RNA. MEG-3_{HMGL-} does not interact with PGL efficiently and forms fewer condensates that do not enrich RNA.

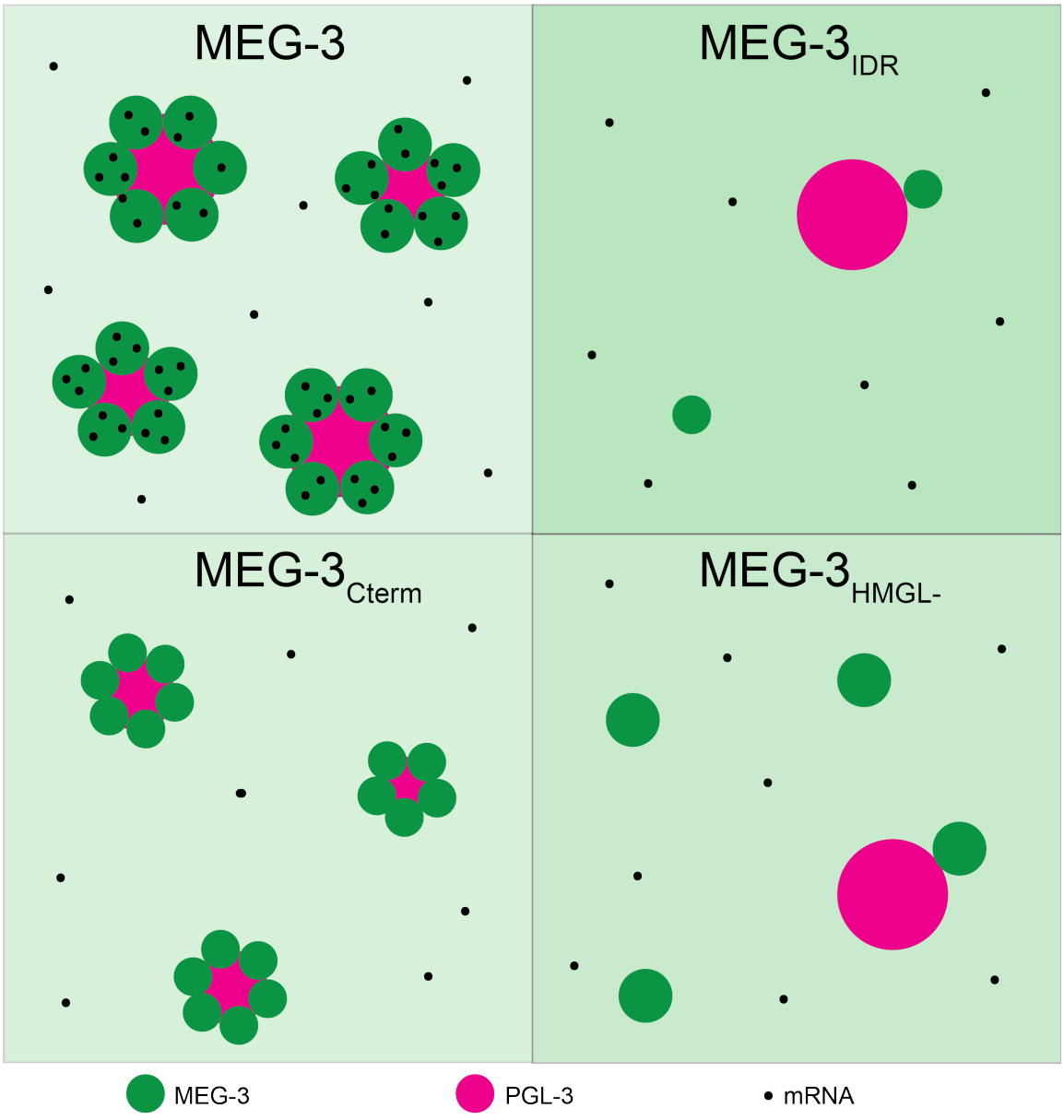
MEG-3
MEG-3IDR
MEG-3Cterm
MEG-3HMGL-
MEG-3
PGL-3
mRNA

Chapter 3

Conclusions and Final Thoughts

3.1 Summary

In this study we have examined the role of MEG-3 in the assembly of P granules. To understand how MEG-3 coordinates PGL and RNA condensation, we used *in vitro* reconstitution experiments and genome editing of the *meg-3* locus to define functional domains in MEG-3. We find that MEG-3 is a bifunctional protein with separate domains for RNA recruitment and protein condensation. We identify a predicted ordered motif in the MEG-3 C-terminus required for high affinity binding to PGL-3 *in vitro* and find that this domain is essential to build MEG-3/PGL-3 co-assemblies that recruit RNA *in vivo*. The MEG-3 IDR binds RNA and enriches MEG-3 in germ plasm but is not sufficient on its own to assemble RNA-rich condensates. Our observations highlight the importance of condensation driven by protein-protein interactions in the assembly of germ granules.

There are still questions that remain about the regulation of P granules. In this chapter we consider some of those questions and how best to address them.

How do P granules protect mRNA from degradation?

We found that MEG-3/4 are required redundantly to protect P granule mRNAs from degradation. This activity requires both the RNA binding and condensate formation functions of MEG-3. However it is not clear how condensation with MEG-3 protects mRNAs. One possible mechanism is that P granules protect RNA from the degradation machinery found in P bodies.

In wild-type embryos, P granules and P bodies are in contact with each other but remain separate bodies (Gallo et al., 2008). It is possible that this separation requires MEG-3 and is disrupted in the MEG-3 derivatives analysed in Chapter 2. Alternatively, P

granules and P bodies may be in competition for condensation with mRNAs, and when the ability of MEG-3 to condense is reduced, mRNAs may be increasingly recruited to P bodies. Interestingly, a similar competition for RNA has also been proposed to exist between stress granules and P bodies (Sanders et al., 2020). Examining the localization of key P body proteins, especially in conjunction with mRNA in embryos expressing the MEG-3 derivatives in this study could provide insight into the interplay between P bodies and P granules in RNA regulation.

What is the role of MEG-3 phosphorylation in P granule assembly?

Previously our lab demonstrated that MEG-3 is a substrate of the kinase MBK-2 and the phosphatase $PP2A^{PPTR1/2}$ and that MEG-3 functions downstream of the kinase and phosphatase to regulate assembly of PGL-1 to P granules (Wang et al., 2014). These observations suggest that phosphorylation of MEG-3 in the anterior of the zygote promotes localized disassembly of P granules and dephosphorylation promotes assembly in the posterior. A prediction of this model is that mutation of the MBK-2 phosphorylation sites in MEG-3 would lead to ectopic P granules in the anterior of the zygote. We tested this prediction in Appendices B-D of this study. While loss of MBK-2 activity did cause MEG-3 to form granules in the anterior of the zygote, none of the mutations in putative phosphorylation sites produced the same result. Interestingly, while mutating 14 of these sites simultaneously in MEG-3 had no effect on MEG-3 localization, it did appear to increase the level of PGL-1 globally and on granules (see Appendix C).

One possible reason for why MEG-3 phosphomutants do not replicate the *mbk-2* mutant phenotype may be that there may be additional yet to be identified phosphorylation sites on MEG-3. Another possibility is that phosphorylation affects MEG-3's ability to bind RNA. The MEG-3 IDR is responsible both for RNA binding *in vitro* and asymmetric enrichment of MEG-3 protein in the P cell *in vivo.* MBK-2 phosphorylation might be affecting the localization of MEG-3 by modulating the RNA binding activity of the IDR. Full length MEG-3, MEG-3_{IDR} and MEG-3_{698} are positively charged (theoretical pI >9). MEG-3 likely binds RNA through electrostatic interactions (Putnam et al., 2019; Smith et al., 2016). If so, phosphorylation of the IDR would be predicted to reduce affinity for RNA. It would be interesting to test this hypothesis using *in vitro* phosphorylated MEG-3.

Another possible mechanism of regulation by MBK-2 is that phosphorylation of MEG-3 controls the assembly of P granule components downstream of MEG-3, rather than the localization of MEG-3 itself. This is consistent with the observation that MEG-3 localization in embryos treated with *mex-5* and *mex-5* RNAi is the same as in an *mbk-2* mutant (Smith et al., 2016). Since MBK-2 priming is required to activate the MEX-5 and MEX-6 (Nishi et al., 2008), the MEG-3 localization defect in *mbk-2* mutants might be caused by the loss of MEX-5/6 activity. Any further generation or characterization of MEG-3 phosphomutants should examine P granule components recruited by MEG-3, such as the PGL-1/3 and mRNA, in addition to the localization of MEG-3 itself.

Final thoughts

While this study has focused specifically on MEG-3 and P granules, the ultimate goal is to provide insight into the assembly and regulation of RNA granules as a whole. As we have expanded our understanding of the variety of RNA granules in cells, it is clear there is no one-size fits all model. Some types of RNA granules, such as stress granules and the nucleolus are more liquid-like (Feric et al., 2016; Guillén-Boixet et al., 2020; Yang et al., 2020). For these compartments, transition to a more solid state has been implicated in disease. For example, mutations in stress granule protein TDP-43 that cause amyotrophic lateral sclerosis cause aggregation *in vitro* (Li et al., 2018). However, for germ granules, a pattern seems to be emerging that the key proteins behave more like gels or solids than liquids (Boke et al., 2016; Kistler et al., 2018; Putnam et al., 2019). While MEG-3, Oskar, and Xvelo are not sequence homologs, they do share a function and some material properties. A critical next step is to mechanism by which these condensates are assembled and disassembled in the developmentally appropriate time and place. Continued study of P granules is an excellent avenue to explore this question.

Appendix A

Insertion of short peptide tags via CRISPR/Cas9 genome editing using single-stranded DNA oligos

This chapter is an edited portion of "Scalable and versatile genome editing using linear DNAs with microhomology to Cas9 Sites in Caenorhabditis elegans" by Paix, A., Wang, Y., Smith, H.E., Lee, C.Y.S., Calidas, D., Lu, T., Smith, J., Schmidt, H., Krause, M.W., Seydoux, G. published in Genetics 198, 1347–1356 in 2014.

A.1 Rationale

Streptococcus pyogenes CRISPR-associated protein 9 (Cas9) is an endonuclease that is targeted to a specific DNA sequence by an associated guide RNA (sgRNA) (Gasiunas et al., 2012; Jinek et al., 2012). In animal models, expression of Cas9/sgRNA complexes in zygotes creates double-strand breaks that are repaired by the cell's repair machineries. Imprecise repair by non-homologous end joining (NHEJ) can create loss-of-function mutations. If a suitable donor molecule is present, homology-dependent repair (HDR) can introduce precise edits at or near Cas9-induced cuts. The donor molecule carries the desired edits flanked by sequences homologous to the targeted locus ("homology arms"). In many systems, HDR is thought to be less efficient than NHEJ, requiring high concentrations of donor molecules or long homology arms to stimulate recombination [(Beumer et al., 2013; Sander and Joung, 2014; Zhang and Glotzer, 2014) for review]. Single-strand oligodeoxynucleotides (ssODNs) can be injected at high concentration, but their relatively small size (~200bp or less) limits the types of edits that can be introduced (micro-edits: point mutations and small deletions/insertions).

Several groups have adapted CRISPR/Cas9 for use in *C. elegans* [(Waaijers and Boxem, 2014) for review]. Additional studies showed that ssODNs can be used to repair Cas9-induced cuts and introduce single-base mutations without selection (ZHAO *et al.* 2014) or by screening worms co-edited at a second locus (Arribere et al., 2014). The latter study reported that ssODN-templated HDR frequently gives rise to partial conversion events where edits >10 bases away from the cut site are not integrated

(Arribere et al., 2014). Whether short homology arms can be used to efficiently introduce gene-sized edits has not yet been evaluated.

Relatively few antibodies recognizing *C. elegans* proteins are available. This makes the addition of short peptide tags such as FLAG, V5, and OLLAS at endogenous loci an attractive target for homology directed repair with ssODN templates. Here we attempted insertion of the V5 tag at the N-terminus of the serine/threonine kinase MBK-2 and the OLLAS tag at the C-terminus of P granule protein MEG-1. These experiments served both as a proof of principle and to allow us to determine the localization of these proteins when expressed form their endogenous locus.

A.2 Results

For the V5::MBK-2 insertions one edit of the correct size detected out of 48 F1s screened (2%, Table 1). This line (JH3196) was isolated as a homozygote and confirmed to be the desired edit by sequencing.

The plates of P0s injected for the MEG-1::OLLAS insertion were contaminated with an unidentified microorganism, resulting in a low brood size. However, 13 F1s were screened and of them 3 had edits of the expected size (23%, Table 1). One of the three lines (JH3274) was isolated as a homozygote and confirmed correct by sequencing. Expression of MEG-1::OLLAS was confirmed by immunostaining (Figure 1).

A.3 Discussion

Together with experiments performed by other lab members, these successful genome edits demonstrated the viability and versatility of linear DNA repair templates

with short (~60bp) homology arms. This method was instrumental in the generation of all the *C. elegans* strains in this study.

The frequencies of editing are not directly comparable between V5::MBK-2 and MEG-1:OLLAS since different guide RNAs were used. However combining this data with experiments performed by other lab members, we hypothesized the V5::MBK-2 insertion had a lower editing frequency due the greater distance between the cut and the insertion site (19 v. 5 bp). This preference for insertions close to the Cas9 cut site was later confirmed (Paix et al., 2017a).

A.4 Methods

CRISPR/Cas9 genome editing – Guide RNA sequences were cloned into the pDD162 Cas9/sgRNA plasmid available from Addgene (Dickinson et al 2013) using the Q5 Site-directed Mutagenesis kit (New England Biolabs). Correct insertion of the guide sequence was confirmed by sequencing (sequencing primer: tatgaaatgcctacaccctctc). Rather than sequence the entire plasmid for each insertion, multiple clones with the correct guide sequence were mixed to ensure at least one expressed Cas9. To easily identify successfully injected worms, we included the plasmid pRF4, which produces a dominant roller phenotype (Mello et al., 1991). The concentration of the final mixture for injection in 15 µl was 120ng/ µl pRF4 and 50ng/µl Cas9/sgRNA plasmid. The injection mix was spun at maximum speed in a tabletop microcentrifuge for 15 minutes before loading into the injection needles.

Following injection, P0s were allowed to lay eggs for one day then transferred to a second plate and allowed to lay the remainder of their brood. F1 progeny were then

grown to young adults (4 days at 20˚C) then screened for rollers. Plates with a high frequency of rollers (jackpot broods) were screened for edits. Both roller and non-roller siblings from jackpot broods were cloned out and allowed to lay eggs for approximately 24 hours. The F1 worms were then transferred to individual tubes and lysed for screening by PCR. A list of all strains produced in this study, including required guide RNAs, repair templates and starting strains is provided in Appendix F – Table 1.

Immunostaining **-** Adult worms were placed into M9 on poly-l-lysine (0.01%) coated slides and squashed with a coverslip to extrude embryos. Slides were frozen by laying on aluminum blocks pre-chilled with dry ice for >5 min. Embryos were permeabilized by freeze-cracking (removal of coverslips from slides) followed by incubation in methanol at -20˚C for >15 min, and in acetone -20˚C for 10 min. Slides were blocked in PBS-Tween (0.1%) BSA (0.5%) for 30min at room temperature, and incubated with 50 ul primary antibody overnight at 4˚C in a humid chamber. Antibody dilutions: Rat αOLLAS-L2 (1:200, Novus Biological Littleton, CO), Secondary antibodies were applied for 2 hr at room temperature. Samples were mounted in VECTASHIELD Antifade Mounting Media with DAPI. Embryos were staged using DAPI stained nuclei.

Confocal Imaging - Fluorescence confocal microscopy was performed using a Zeiss Axio Imager with a Yokogawa spinning-disc confocal scanner. Samples were illuminated with 405/488/561/637nm solid-state laser (Coherent), using a 405/488/561/640 transmitting dichroic (Semrock) and 624-40/692-40/525-30/445-45nm bandpass filter (Semrock) respectively. Images from either microscope were

taken with using Slidebook v6.0 software (Intelligent Imaging Innovations) using a 63X-1.4NA.

A.5 Figures

Table 1 - Summary of V5::MBK-2 and MEG-1::OLLAS genome editing results

Gene	Insertion	Location	Distance from cut to insertion	Length of homology arms	F1s screened	% F1s Edited
mbk-2	V5	N-terminus	19 bp	55, 58 bp	48	2%
meg-1	OLLAS	C-terminus	5 bp	68, 50 bp	13	23%

Figure 1 – MEG-1::OLLAS in the early embryo

A. Representative photomicrographs of embryos expressing MEG-1::OLLAS at the indicated stages immunostained for OLLAS (green signal). Images are maximum projections of 20 z-slices, spaced 1 micron apart.

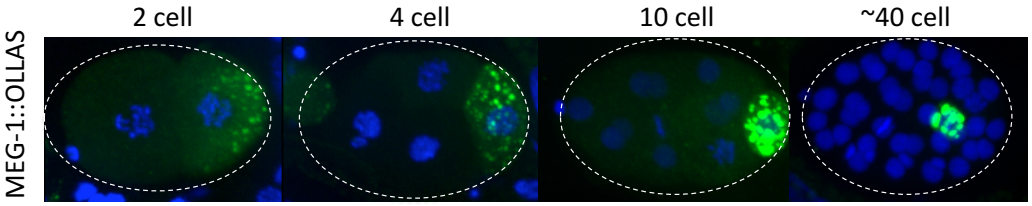
2 cell
4 cell
10 cell
~40 cell
MEG-1::OLLAS

Appendix B

CRISPR/Cas9 replication of *mbk-2(dd5)* temperature sensitive mutant

B.1 Rationale

Loss of DYRK family kinase MBK-2 was known to cause many P granule components to remain symmetrically condensed in the zygote (Pellettieri et al., 2003; Quintin et al., 2003; Jennifer T. Wang et al., 2014). Furthermore, MEG-3 is a substrate of MBK-2 (Jennifer T. Wang et al., 2014). However, we had not yet tested whether MBK-2 affected the localization of any of the MEG proteins. We hypothesized that MEG-3 would behave similar to PGL-1 in the absence MBK-2. We initially sought to test this by performing *mbk-2* RNAi on an endogenously tagged MEG-3::OLLAS strain, however the RNAi did not work well as embryonic lethality was low across multiple genotypes (16% N=402). To avoid this issue, we instead recreated the temperature-sensitive loss of function allele *dd5* in *mbk-2* in the MEG-3::OLLAS strain. The *dd5* allele is a single g>a base change at genomic position IV: 13033544 resulting in the missense mutation in a conserved aspartic acid (D374N in isoform a) in the kinase domain of MBK-2 (Quintin et al., 2003).

B.2 Results

The generation of the *dd5* mutation was successful; 41/90 (45%) F1s screened were edited. Two independent lines (F9-5-5 and F9-6-4, not maintained or assigned a JH number) were isolated and sequence confirmed. Both were 100% embryonic lethal at 25˚ (F9-5-5 N=293, F9-6-4 N=205).

To determine if loss of MBK-2 function affected MEG-3 and PGL-1 localization, wild-type and *mbk-2(dd5);* MEG-3:OLLAS worms were raised from L1s to adults at the restrictive (25˚) temperature. Wild-type embryos formed P granules with both MEG-3

and PGL-1 localized to the posterior. In *mbk-2(dd5)* embryos, MEG-3 and PGL-1 still formed small granules, but they were symmetric (Figure 1).

B.3 Conclusions and further questions

The *mbk-2 (dd5)* temperature sensitive mutation made by CRISPR/Cas9 genome editing replicated the embryonic lethality and symmetry of PGL-1 granules previously observed with *mbk-2* RNAi and the EMS-generated allele. The asymmetric localization of MEG-3 in the early embryo also requires MBK-2. While in many cases RNAi may be sufficient this CRISPR design to make the *mbk-2* temperature sensitive allele would be especially useful in the case of mutants such as *meg-3 meg-4* which are resistant to RNAi.

B.4 Methods

CRISPR/Cas9 genome editing was performed as described in Paix et al., 2017. A list of strains generated in this study along with the required guides, repair templates and starting strains is provided in Appendix F - Table 1. Genome edits were detected by PCR with primers ACAAGTGCATCACGTTTGAGC and GATGTGGCCGTGCAATAACG, followed by restriction enzyme digestion with XmaI. Expected sizes are WT = 573bp arnd *dd5*= 137, 436bp.

Immunostaining **-** Adult worms were placed into M9 on poly-l-lysine (0.01%) coated slides and squashed with a coverslip to extrude embryos. Slides were frozen by laying on aluminum blocks pre-chilled with dry ice for >5 min. Embryos were permeabilized by freeze-cracking (removal of coverslips from slides) followed by

incubation in methanol at -20˚C for >15 min, and in acetone -20˚C for 10 min. Slides were blocked in PBS-Tween (0.1%) BSA (0.5%) for 30min at room temperature, and incubated with 50 ul primary antibody overnight at 4˚C in a humid chamber. Antibody dilutions (in PBST/BSA): Anti-PGL-1 (K76 1:10 DSHB), Rat αOLLAS-L2 (1:200, Novus Biological Littleton, CO), Secondary antibodies were applied for 2 hr at room temperature. Samples were mounted in VECTASHIELD Antifade Mounting Media with DAPI. Embryos were staged using DAPI stained nuclei and 15 confocal slices spaced 1 micron apart and centered on the nucleus.

Confocal Imaging - Fluorescence confocal microscopy was performed using a Zeiss Axio Imager with a Yokogawa spinning-disc confocal scanner. Samples were illuminated with 405/488/561/637nm solid-state laser (Coherent), using a 405/488/561/640 transmitting dichroic (Semrock) and 624-40/692-40/525-30/445-45nm bandpass filter (Semrock) respectively. Images from either microscope were taken with using Slidebook v6.0 software (Intelligent Imaging Innovations) using a 63X-1.4NA.

Embryonic lethality -Embryonic lethality was scored by placing ~10 mothers raised at 25˚C onto a fresh plate and allowing them to lay eggs for ~1 hour. Mothers were then removed and the number of embryos was counted. The number of adults on each plate was then counted after three days. Embryonic lethality for each plate was calculated as [(embryos – adults)/embryos].

B.5 Figures

Table 1 – Embryonic lethality of CRISPR-generated *mbk-2(dd5)* alleles at 25˚ C

Strain	Plate	Embryos	Hatch	Embryonic Lethality
F9-5-5	1	156	0	100.0%
	2	137	0	100.0%
	Total	**293**	**0**	**100.0%**
F9-6-4	1	108	0	100.0%
	2	97	0	100.0%
	Total	**205**	**0**	**100.0%**

Figure 1 – MBK-2 activity is required for MEG-3 and PGL-1 asymmetry in the early embryo

A. Representative photomicrographs of the indicated genotypes raised at 25˚, immunostained for MEG-3 (anti-OLLAS) and PGL-1 (anti-PGL-1).

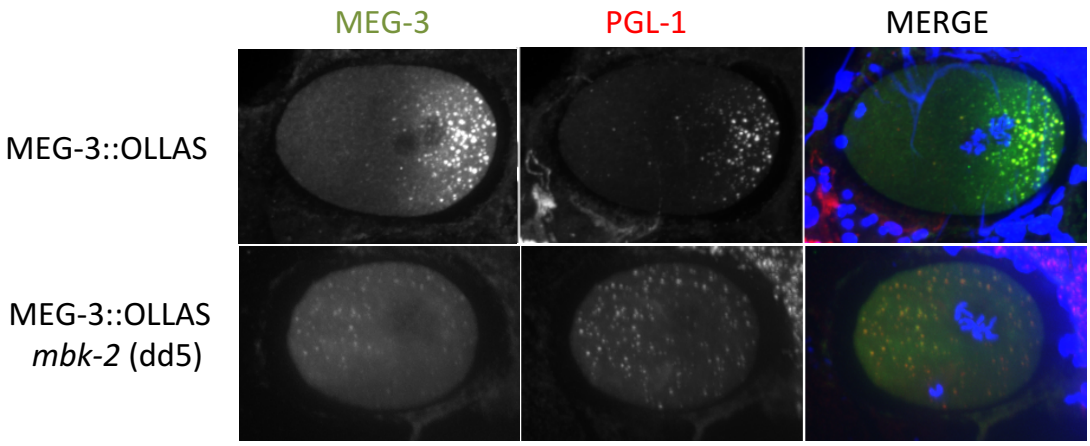
MEG-3
PGL-1
MERGE
MEG-3::OLLAS
MEG-3::OLLAS
mbk-2 (dd5)

Appendix C

Simultaneous alanine substitution of 14 putative phosphorylation sites in MEG-3

C.1 Rationale

MEG-3 is a serine-rich protein and is phosphorylated *in vivo* (Wang et al., 2014). However, detection of phosphorylated sites by mass spectrometry is challenging due to the low concentration of MEG-3, and MBK-2 was still able to phosphorylate MEG-3 *in vitro* even when all three predicted phosphorylation sites had been mutated to alanine (Jennifer T. Wang et al., 2014). We therefore attempted to replace a segment of MEG-3 with a homology template containing multiple alanine substitutions in conserved serines (Methods). Previously we had not been able to directly replace a gene, even when we included many silent mutations to attempt to prevent premature repair of a cut without insertion. We hypothesized that previous failures might have been caused by 1) guide RNAs with poor cutting efficiency or 2) premature template switching during homology directed repair despite the presence of mutations in the repair template. To differentiate between these two possibilities, we attempted this genome edit both as a single step and in two steps; first deleting the region, then cutting again to insert the region with the desired mutations. A diagram of these two strategies is provided in Figure 1, along with DNA and protein alignments of the mutants in Figure 1 – Supplement 1.

C.2 Results

Replacement of large regions by homology directed repair of CRISPR/Cas9 cuts requires two steps when the desired replacement is homologous

The single step replacement did not produce any of the desired edit. Of 45 F1 rollers screened, one had a complete deletion of the region, while three had smaller

than expected insertions, but none were the expected size. The initial deletion step of the two-step process however, had edits of the expected size in 50 out of 62 F1 rollers (81%). We concluded that rHS06 and rHS07 are efficient guides, and therefore the single step replacement likely fails due to short regions of homology within the repair template.

Three homozygous deletions were isolated and were all confirmed by sequencing to have correctly incorporated the engineered guide sequence (HotSpot 1 GGGAAGTTTGTCCAGAGCAG). One of these lines (JH3889) was then used to insert the final MEG-3_{14A} sequence. Of the 69 F1 rollers screened, 16 had insertions of the expected size (23%). From these, five homozygous lines were isolated, and four of those were sequence confirmed to be the expected edit. Two lines 5.11 (JH3890) and 5.18 (JH3891) were maintained.

MEG-3_{14A} localization is similar to wild type MEG-3, but appears fainter on granules

To compare the localization and affect on P granules of wild type MEG-3 and MEG-3_{14A} we performed immunofluorescence using antibodies recognizing MEG-3 (anti-OLLAS) and PGL-1 (K76). In the early embryo, wild-type MEG-3 formed an anterior-oriented gradient and was localized to P granules as expect. MEG-3_{14A} localization was indistinguishable from wild type in the early embryo in both strains (Figure 2A). However MEG-3_{14A} granules were generally less bright than in wild type MEG-3. To determine if MEG-3_{14A} expression was reduced compared to wild-type, we performed a western blot (Figure 2B). MEG-3 protein levels were similar in both wild-type and the two MEG-3_{14A} lines. The difference detected in staining might be due to variations in

immunostaining. Alternatively, MEG-3_{14A} might appear dimmer on granules because a higher fraction of it is in the cytoplasm or a small difference in MEG-3 level might be difficult to detect on a western blot.

PGL-1 levels appear increased in early embryos expressing MEG-3_{14A}

By immunofluorescence, PGL-1 levels appeared to be increased in MEG-3_{14A} relative to wild-type. Additionally, more PGL-1 granules were detected in the anterior of the embryo. This was evident at multiple stages, but is most striking when the one cell embryo is undergoing nuclear envelop breakdown, where PGL-1 granules are only present in embryos expressing MEG-3_{14A} and not in wild type (Figure 2A).

As it is difficult to compare protein levels by immunofluorescence and the PGL-1 antibody is not suitable for western blotting, we crossed in PGL-1::GFP expressed from its endogenous locus. Compared to embryos expressing wild-type MEG-3, embryos expressing MEG-3_{14A} had a greater average intensity of PGL-1::GFP. As seen by immunofluorescence, PGL-1 granules were detected in the anterior of embryos expressing MEG-3_{14A} (Figure2 C,D). However, given the increased PGL-1::GFP signal intensity, it is possible that such granules do exist in wild-type, but are not detectable above the cytoplasmic signal. This apparent increase in PGL-1::GFP expression was not detected on a western blot, however the loading control was only detected in the GFP negative control (Figure 2E). To draw conclusions, this analysis would need to be repeated with more concentrated embryonic lysates.

MEG-3_{14A} is likely still phosphorylated *in vivo*

To determine if these 14 alanine substitutions affected the phosphorylation state of MEG-3 *in vivo,* we analyzed the MEG-3_{14A} and wild type MEG-3 lysates by Phos-tag SDS-PAGE. Phos-tag slows the migration of phosphorylated proteins, such that the phosphorylated species of the protein appear as separate bands or a smear above the non-phosphorylated species (Kinoshita et al., 2006). Similar to previous reports with transgenic GFP::MEG-3, wild-type MEG-3 appeared smeared or occasionally as two fainter bands on the Phos-tag gel, compared to sharper bands with standard SDS-PAGE. Both MEG-3_{14A} lines showed some smearing on the Phos-tag gel as well, though the non-phosphorylated band did sometimes appear increased in intensity (Figure 2F). Given the variability between replicates and that the Phos-tag method does not work well with a loading control, it is difficult to conclude the phosphorylation state of MEG-3_{14A}, but it might still be phosphorylated at some phosphorylation at other sites.

C.3 Conclusions and further questions

When attempting to replace a sequence of DNA with a homologous sequence by CRISPR/Cas9 genome editing, the replacement should be completed in two steps. First delete the region and design the resulting sequence to be cut by a different guide RNA. After isolating the deletion strain, use the new guide to introduce the desired final sequence.

MEG-3_{14A} does not have a strong effect on MEG-3 localization in the early embryo despite removing all three predicted MBK-2 phosphorylation sites and eleven other serines. This strain does have the homolog MEG-4 present, so deleting or knocking *meg-4* by RNAi would be an important first step to rule out complementation.

Additionally, as loss of MBK-2 activity causes symmetric MEG-3 granules, MBK-2 may phosphorylate MEG-3 at additional sites, or may act through other upstream proteins such as MEX-5/6. Unlike MEG-1, MEG-3 phosphorylation is difficult to resolve using Phost-tag SDS-PAGE, so any future experiments should include an alkaline phosphatase treated control.

Most interestingly, MEG-3_{14A} appears to increase PGL-1 levels in the early embryo and increase its recruitment to P granules. Further investigation is needed to determine how this might be occurring. The effect of MEG-3_{14A} on PGL-1 may or may not be due to a change in phosphorylation state relative to wild-type MEG-3. Since MEG-3 binds PGL-1 directly *in vitro,* it would be interesting to see if MEG-3_{14A} has any affect on this binding.

Both MEG-3 and PGL-1 appeared to have changes in their levels in embryos expressing MEG-3_{14A} when visualized in the early embryo, but these changes were not well detected by western blot. The PGL-1 blot should be repeated with more concentrated lysates so the loading control can be detected, however these changes might be masked by the fact that the majority of embryos in a mixed-stage lysate will be later in development. However it might be beneficial in the future to try fluorescence-based detection for the western blots rather than chemiluminescence as there is a better linear correlation between protein level and signal intensity.

Finally, the intermediate strain in the two step replacement in which bp 1399-2052 of the MEG-3 ORF are deleted and replaced with the HotSpot 1 guide sequence (JH3889) was designed to produce an in-frame protein with amino acids 451 to 627 of

MEG-3 deleted. It could be useful to compare the effect of this deletion to that of MEG-3_{14A}.

C.4 Methods

Selection of putative phosphorylation sites- The region of MEG-3 to be replaced was chosen to include the predicted MBK-2 phosphorylation sites T541, S582, and T605 (Wang et al., 2014) . Additional serines were selected based on conservation between MEG-3 and MEG-4 (S456, S457, S459, S461, S482, S486, S487, S492, S520, S526, S543) for a total of 14 sites (MEG-3_{14A}).

CRISPR/Cas9 genome editing - CRISPR/Cas9 genome editing was performed as described in (Paix et al., 2017b). A list of strains generated in this study along with the required guides, repair templates and starting strains is provided in Appendix F - Table 1. A diagram of the two methods of replacement is provided in Figure 1. For the single step replacement, silent mutations were chosen so that the final sequence had a similar codon usage to the endogenous gene using CAIcal (Puigbò et al., 2008) and only a single intron was included to reduce the overall size of the insertion. For the two step insertion, the only changes to the endogenous sequence are the 14 alanine substitutions. Genome edits were detected by PCR with primers CAAGGACGGCACTGAACTCT and TTTCGAAGGGCCATTTCCCA. Expected sizes are wild-type and two step replacement = 985 bp, deletion = 344 bp, single step replacement = 896 bp

Immunostaining **-** Adult worms were placed into M9 on poly-l-lysine (0.01%) coated slides and squashed with a coverslip to extrude embryos. Slides were

frozen by laying on aluminum blocks pre-chilled with dry ice for >5 min. Embryos were permeabilized by freeze-cracking (removal of coverslips from slides) followed by incubation in methanol at -20˚C for >15 min, and in acetone -20˚C for 10 min. Slides were blocked in PBS-Tween (0.1%) BSA (0.5%) for 30min at room temperature, and incubated with 50 ul primary antibody overnight at 4˚C in a humid chamber. Antibody dilutions (in PBST/BSA): Anti-PGL-1 (K76 1:10 DSHB), Rat αOLLAS-L2 (1:200, Novus Biological Littleton, CO), Secondary antibodies were applied for 2 hr at room temperature. Samples were mounted in VECTASHIELD Antifade Mounting Media with DAPI. Embryos were staged using DAPI stained nuclei.

Confocal Imaging - Fluorescence confocal microscopy was performed using a Zeiss Axio Imager with a Yokogawa spinning-disc confocal scanner. Samples were illuminated with 405/488/561/637nm solid-state laser (Coherent), using a 405/488/561/640 transmitting dichroic (Semrock) and 624-40/692-40/525-30/445-45nm bandpass filter (Semrock) respectively. Images from either microscope were taken with using Slidebook v6.0 software (Intelligent Imaging Innovations) using a 63X-1.4NA.

Quantification of mean GFP fluorescence in embryos expressing PGL-1::GFP – Embryos were dissected from mothers into M9. Embryos undergoing nuclear envelope breakdown were identified by bright field microscopy. Sum projections of 20 z-slices spaced 1 micron apart were made using imageJ. An a ROI was drawn around the embryo to measure the mean intensity. The mean background intensity was measured

in an ROI away from the embryo in the same image and subtracted from the embryonic value to give the a background-corrected mean intensity.

Western blotting of embryonic lysates - Worms were synchronized by bleaching to collect embryos, shaken approximately 20hrs in M9, then plating on large enriched peptone plates with a lawn of *E. Coli* NA22 bacteria. Embryos were harvested from young adults (66 hours after starved L1 plating) and sonicated in 2% SDS, 65 mM Tris pH 7, 10% glycerol with protease and phosphatase inhibitors. Lysates were spun at 14,000 rpm for 30 min at 4˚ C and cleared supernatants were transferred to fresh tubes. Lysates were run on 4-12% Bis-Tris pre-cast gels (Bio-Rad Hercules, CA). Western blot transfer was performed for 1 hr at 4°C onto PVDF membranes. Membranes were blocked overnight and washed in 5% milk, 0.1% Tween-20 in PBS; primary antibodies were incubated overnight at 4˚ C; secondary antibodies were incubated for two hours at room temperature. Antibody dilutions in 5% milk/PBST: Rat α OLLAS-L2 (1:1000, Novus Biological Littleton, CO), Mouse α tubulin (1:1000, Sigma St. Louis, MO), Mouse α GFP JL-8 (1:500, Takara Bio, Japan)

Phos-tag gels – Embryonic lysates were prepared as for western blotting. Samples were run in parallel on Phos-tag gels (7% SDS-PAGE with 25 uM Phos-tag and 50 uM MnCl2) and 7% SDS-PAGE at 30 mA for 2.5 hours. Gels were washed in transfer buffer with 1 mM EDTA twice for 10 minutes each, and washed in transfer buffer without EDTA twice for 10 minutes each. Western blot transfer was performed for overnight (approximately 16 hours) at room temperature onto PVDF membranes.

Membranes were blocked and washed in 5% milk, 0.1% Tween-20 in PBS and probed with Rat α OLLAS-L2 antibody (1:1000, Novus Biological Littleton, CO).

C.5 Figures

Figure 1 - Diagram of the generation of MEG-3_{14A} in one (A) or two (B) steps.

A. From top to bottom: the *meg-3* locus in JH3374 is cut by rHS06 and rHS07, a dsDNA repair template is provided with the 14 alanine substitutions (yellow lines) and multiple silent mutations that do not affect DNA sequence (pink region) and MEG-3_{14A} with multiple silent mutations is generated by homology directed repair. The total size of the insertion is 576 bp **(B)** From top to bottom: the *meg-3* locus in JH3374 is cut by rHS06 and rHS07, ssDNA oligomer oHS179 is provided and bp 1399-2052 of the meg-3 ORF are replaced by the HotSpot 1 sequence. The resulting deletion strain is then cut with Hotspot 1 and a dsDNRA repair template is provided with the 14 alanine substitutions to generate MEG-3_{14A} by homology directed repair. Complete DNA and Protein sequences are provided in Figure 1 – supplement 1

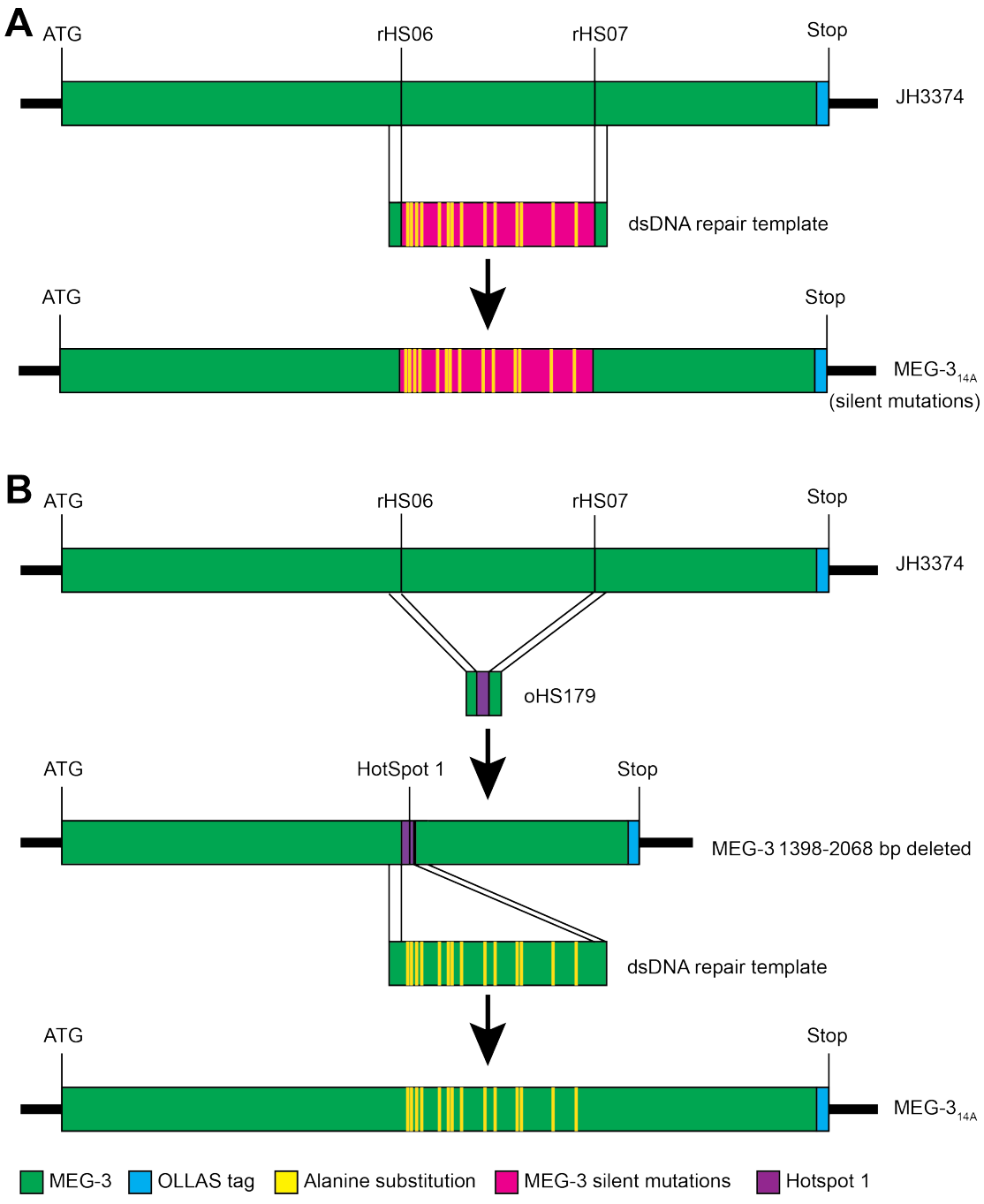
A
ATG
rHS06
rHS07
Stop
JH3374
dsDNA repair template
ATG
Stop
MEG-3 14A
(silent mutations)
B
ATG
rHS06
rHS07
Stop
JH3374
oHS179
ATG
HotSpot 1
Stop
MEG-3 1398-2068 bp deleted
dsDNA repair template
ATG
Stop
MEG-3 14A
MEG-3
OLLAS tag
Alanine substitution
MEG-3 silent mutations
Hotspot 1

Figure 1 – supplement 1 DNA and protein sequences of strains used in generation MEG-3_{14A}

A. Aligned DNA sequences of the coding region of OLLAS-tagged wild-type MEG-3 (MEG-3::OLLAS) and the indicated MEG-3 derivatives. Exons are in uppercase, introns in lowercase. Yellow color indicates alanine substitutions, pink indicates additional silent mutations which do not change the protein sequence, purple indicates the HotSpot-1 DNA sequence and blue indicates the OLLAS sequence. Asterisks below the sequence indicate 100% identity between all sequences

B. Aligned protein sequences of MEG-3 and the indicated derivatives. MEG-3_{14A} with silent mutations is identical to MEG-3_{14A}. Yellow color indicates the alanine substitutions, blue color indicates the OLLAS tag.

Figure 1 –supplement 1 A

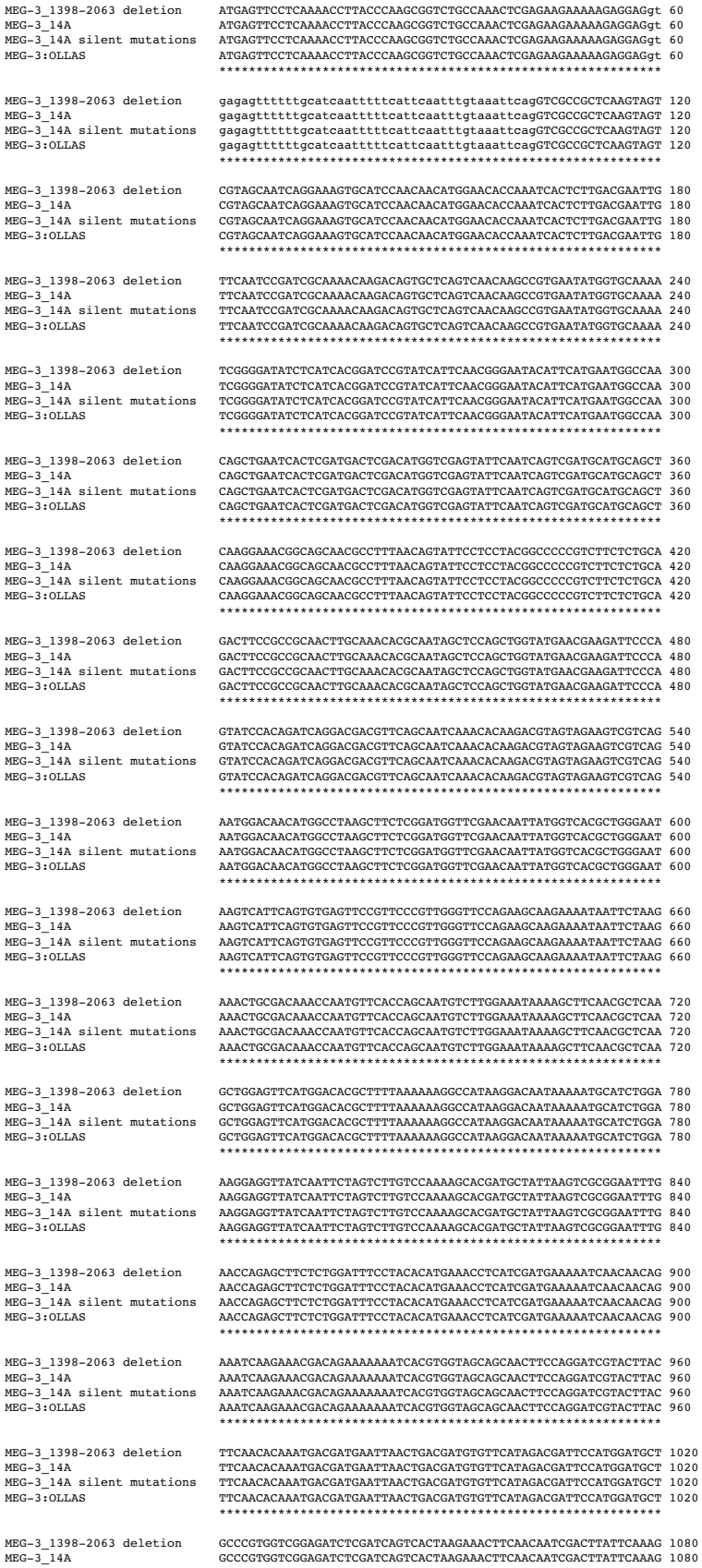

Figure 1 –supplement 1 A continued

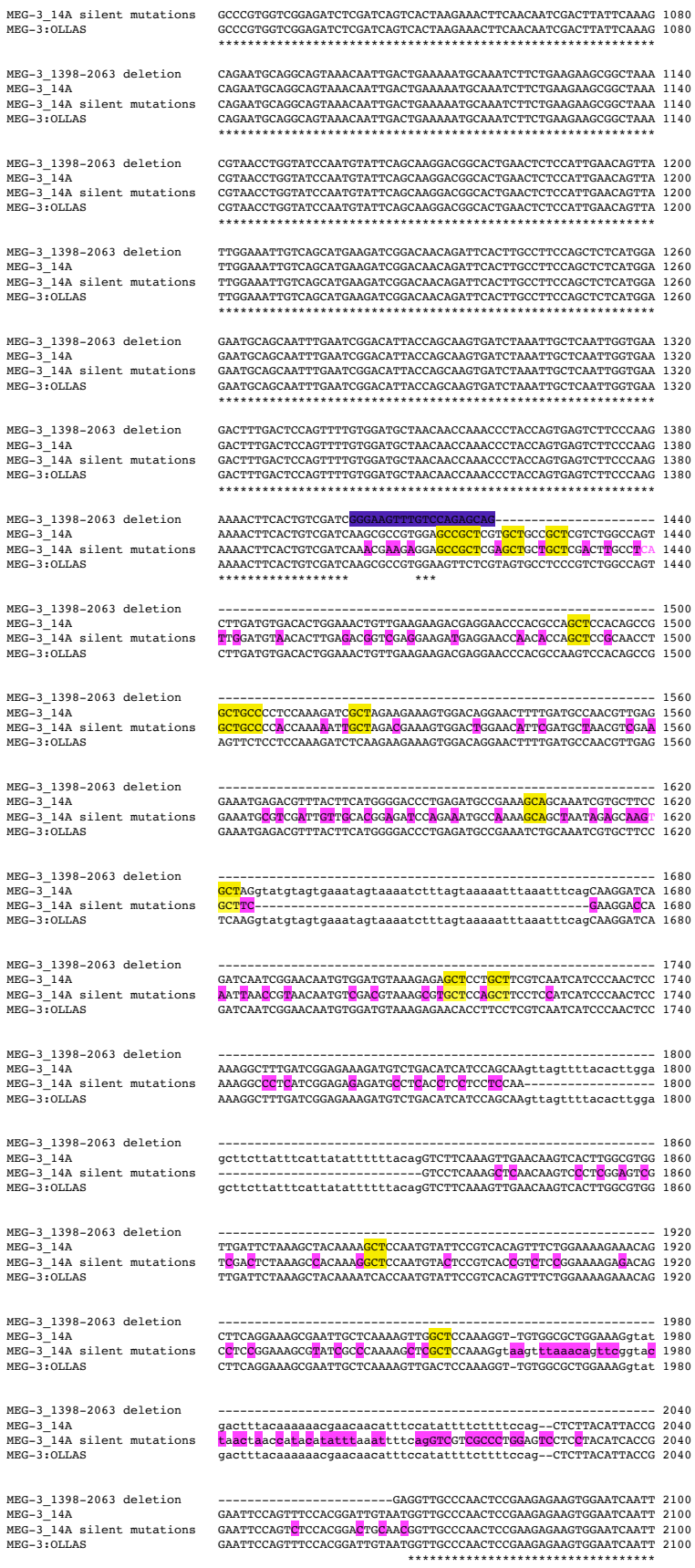

Figure 1 –supplement 1 A continued

```
MEG-3_1398-2063 deletion     GTGAAATTCGTGCAGCTGAAGTATACAATCAAGCTGGGAAATGGCCCTTCGAAATCACCA 2160
MEG-3_14A                    GTGAAATTCGTGCAGCTGAAGTATACAATCAAGCTGGGAAATGGCCCTTCGAAATCACCA 2160
MEG-3_14A silent mutations   GTGAAATTCGTGCAGCTGAAGTATACAATCAAGCTGGGAAATGGCCCTTCGAAATCACCA 2160
MEG-3:OLLAS                  GTGAAATTCGTGCAGCTGAAGTATACAATCAAGCTGGGAAATGGCCCTTCGAAATCACCA 2160
                             ************************************************************

MEG-3_1398-2063 deletion     Ggtaaggtccaagttaataaatccgctatcgatcaagcatatggaaaataatgtacaagc 2220
MEG-3_14A                    Ggtaaggtccaagttaataaatccgctatcgatcaagcatatggaaaataatgtacaagc 2220
MEG-3_14A silent mutations   Ggtaaggtccaagttaataaatccgctatcgatcaagcatatggaaaataatgtacaagc 2220
MEG-3:OLLAS                  Ggtaaggtccaagttaataaatccgctatcgatcaagcatatggaaaataatgtacaagc 2220
                             ************************************************************

MEG-3_1398-2063 deletion     tgaaaagattgagctcaaaacttgattcaaatcctgtaaaattattttctgagtacagta 2280
MEG-3_14A                    tgaaaagattgagctcaaaacttgattcaaatcctgtaaaattattttctgagtacagta 2280
MEG-3_14A silent mutations   tgaaaagattgagctcaaaacttgattcaaatcctgtaaaattattttctgagtacagta 2280
MEG-3:OLLAS                  tgaaaagattgagctcaaaacttgattcaaatcctgtaaaattattttctgagtacagta 2280
                             ************************************************************

MEG-3_1398-2063 deletion     aatttctttcagTGATCCGGCTCCACTTCCTTGTGAATCAGCCGATCGGATCGAATATCC 2340
MEG-3_14A                    aatttctttcagTGATCCGGCTCCACTTCCTTGTGAATCAGCCGATCGGATCGAATATCC 2340
MEG-3_14A silent mutations   aatttctttcagTGATCCGGCTCCACTTCCTTGTGAATCAGCCGATCGGATCGAATATCC 2340
MEG-3:OLLAS                  aatttctttcagTGATCCGGCTCCACTTCCTTGTGAATCAGCCGATCGGATCGAATATCC 2340
                             ************************************************************

MEG-3_1398-2063 deletion     TTCTCAAGATTGCACTCAAGATCCAGCTTCAACCTCGCCACCACCTCGCATTTCTGAAAG 2400
MEG-3_14A                    TTCTCAAGATTGCACTCAAGATCCAGCTTCAACCTCGCCACCACCTCGCATTTCTGAAAG 2400
MEG-3_14A silent mutations   TTCTCAAGATTGCACTCAAGATCCAGCTTCAACCTCGCCACCACCTCGCATTTCTGAAAG 2400
MEG-3:OLLAS                  TTCTCAAGATTGCACTCAAGATCCAGCTTCAACCTCGCCACCACCTCGCATTTCTGAAAG 2400
                             ************************************************************

MEG-3_1398-2063 deletion     CTTGACAGCATTCCTGGAAGCTCAGCAAGACTTTAACGACTACATTGATACTAACTACAA 2460
MEG-3_14A                    CTTGACAGCATTCCTGGAAGCTCAGCAAGACTTTAACGACTACATTGATACTAACTACAA 2460
MEG-3_14A silent mutations   CTTGACAGCATTCCTGGAAGCTCAGCAAGACTTTAACGACTACATTGATACTAACTACAA 2460
MEG-3:OLLAS                  CTTGACAGCATTCCTGGAAGCTCAGCAAGACTTTAACGACTACATTGATACTAACTACAA 2460
                             ************************************************************

MEG-3_1398-2063 deletion     AGAAAAGACACAACTCCTGAAAGTGAATTTGAATATTCACGGGATGTCACCTGAAAGATG 2520
MEG-3_14A                    AGAAAAGACACAACTCCTGAAAGTGAATTTGAATATTCACGGGATGTCACCTGAAAGATG 2520
MEG-3_14A silent mutations   AGAAAAGACACAACTCCTGAAAGTGAATTTGAATATTCACGGGATGTCACCTGAAAGATG 2520
MEG-3:OLLAS                  AGAAAAGACACAACTCCTGAAAGTGAATTTGAATATTCACGGGATGTCACCTGAAAGATG 2520
                             ************************************************************

MEG-3_1398-2063 deletion     GCTGTACTTGAATTATTTTTGCACCGAGACAATTCCAAGATTGGATGGTCCTTATGCCGA 2580
MEG-3_14A                    GCTGTACTTGAATTATTTTTGCACCGAGACAATTCCAAGATTGGATGGTCCTTATGCCGA 2580
MEG-3_14A silent mutations   GCTGTACTTGAATTATTTTTGCACCGAGACAATTCCAAGATTGGATGGTCCTTATGCCGA 2580
MEG-3:OLLAS                  GCTGTACTTGAATTATTTTTGCACCGAGACAATTCCAAGATTGGATGGTCCTTATGCCGA 2580
                             ************************************************************

MEG-3_1398-2063 deletion     TGgtaagaaagataagacatatttaatcttgaaaactttaatttttcagATCCAAGAGT 2640
MEG-3_14A                    TGgtaagaaagataagacatatttaatcttgaaaactttaatttttcagATCCAAGAGT 2640
MEG-3_14A silent mutations   TGgtaagaaagataagacatatttaatcttgaaaactttaatttttcagATCCAAGAGT 2640
MEG-3:OLLAS                  TGgtaagaaagataagacatatttaatcttgaaaactttaatttttcagATCCAAGAGT 2640
                             ************************************************************

MEG-3_1398-2063 deletion     TCCACCTGTGCGAAATATGTTCAGAAAATGGTTCCTCCGTTTTGCTGAAGCCTGCTTAGG 2700
MEG-3_14A                    TCCACCTGTGCGAAATATGTTCAGAAAATGGTTCCTCCGTTTTGCTGAAGCCTGCTTAGG 2700
MEG-3_14A silent mutations   TCCACCTGTGCGAAATATGTTCAGAAAATGGTTCCTCCGTTTTGCTGAAGCCTGCTTAGG 2700
MEG-3:OLLAS                  TCCACCTGTGCGAAATATGTTCAGAAAATGGTTCCTCCGTTTTGCTGAAGCCTGCTTAGG 2700
                             ************************************************************

MEG-3_1398-2063 deletion     AAATCCTCACCAGCTTGCAGTTATGCAAGAGATTGCTGCCACGTTTGTTCAGGCTCGGCT 2760
MEG-3_14A                    AAATCCTCACCAGCTTGCAGTTATGCAAGAGATTGCTGCCACGTTTGTTCAGGCTCGGCT 2760
MEG-3_14A silent mutations   AAATCCTCACCAGCTTGCAGTTATGCAAGAGATTGCTGCCACGTTTGTTCAGGCTCGGCT 2760
MEG-3:OLLAS                  AAATCCTCACCAGCTTGCAGTTATGCAAGAGATTGCTGCCACGTTTGTTCAGGCTCGGCT 2760
                             ************************************************************

MEG-3_1398-2063 deletion     GGACGATACGAGCAGCTCCACAGACTCCACCAATATGCTCTACATGTTGTGGAAGGAGTG 2820
MEG-3_14A                    GGACGATACGAGCAGCTCCACAGACTCCACCAATATGCTCTACATGTTGTGGAAGGAGTG 2820
MEG-3_14A silent mutations   GGACGATACGAGCAGCTCCACAGACTCCACCAATATGCTCTACATGTTGTGGAAGGAGTG 2820
MEG-3:OLLAS                  GGACGATACGAGCAGCTCCACAGACTCCACCAATATGCTCTACATGTTGTGGAAGGAGTG 2820
                             ************************************************************

MEG-3_1398-2063 deletion     TATCGGACAGAAGAATATCATCGCAATTGCTGATGCGTGTTTACTTGCACATCTTCGGAA 2880
MEG-3_14A                    TATCGGACAGAAGAATATCATCGCAATTGCTGATGCGTGTTTACTTGCACATCTTCGGAA 2880
MEG-3_14A silent mutations   TATCGGACAGAAGAATATCATCGCAATTGCTGATGCGTGTTTACTTGCACATCTTCGGAA 2880
MEG-3:OLLAS                  TATCGGACAGAAGAATATCATCGCAATTGCTGATGCGTGTTTACTTGCACATCTTCGGAA 2880
                             ************************************************************

MEG-3_1398-2063 deletion     ATCGGATCCTATCAAATACTTGAATGTAAAACGGGATTGGCTGGAATCTATTTTTGACCC 2940
MEG-3_14A                    ATCGGATCCTATCAAATACTTGAATGTAAAACGGGATTGGCTGGAATCTATTTTTGACCC 2940
MEG-3_14A silent mutations   ATCGGATCCTATCAAATACTTGAATGTAAAACGGGATTGGCTGGAATCTATTTTTGACCC 2940
MEG-3:OLLAS                  ATCGGATCCTATCAAATACTTGAATGTAAAACGGGATTGGCTGGAATCTATTTTTGACCC 2940
                             ************************************************************

MEG-3_1398-2063 deletion     ACCCAGAGATCAATCCGGATTCGCCAACGAGCTCGGACCACGTCTCATGGGAAAGTGA 2998
MEG-3_14A                    ACCCAGAGATCAATCCGGATTCGCCAACGAGCTCGGACCACGTCTCATGGGAAAGTGA 2998
MEG-3_14A silent mutations   ACCCAGAGATCAATCCGGATTCGCCAACGAGCTCGGACCACGTCTCATGGGAAAGTGA 2998
MEG-3:OLLAS                  ACCCAGAGATCAATCCGGATTCGCCAACGAGCTCGGACCACGTCTCATGGGAAAGTGA 2998
                             ************************************************************
```

Figure 1 –supplement 1 B

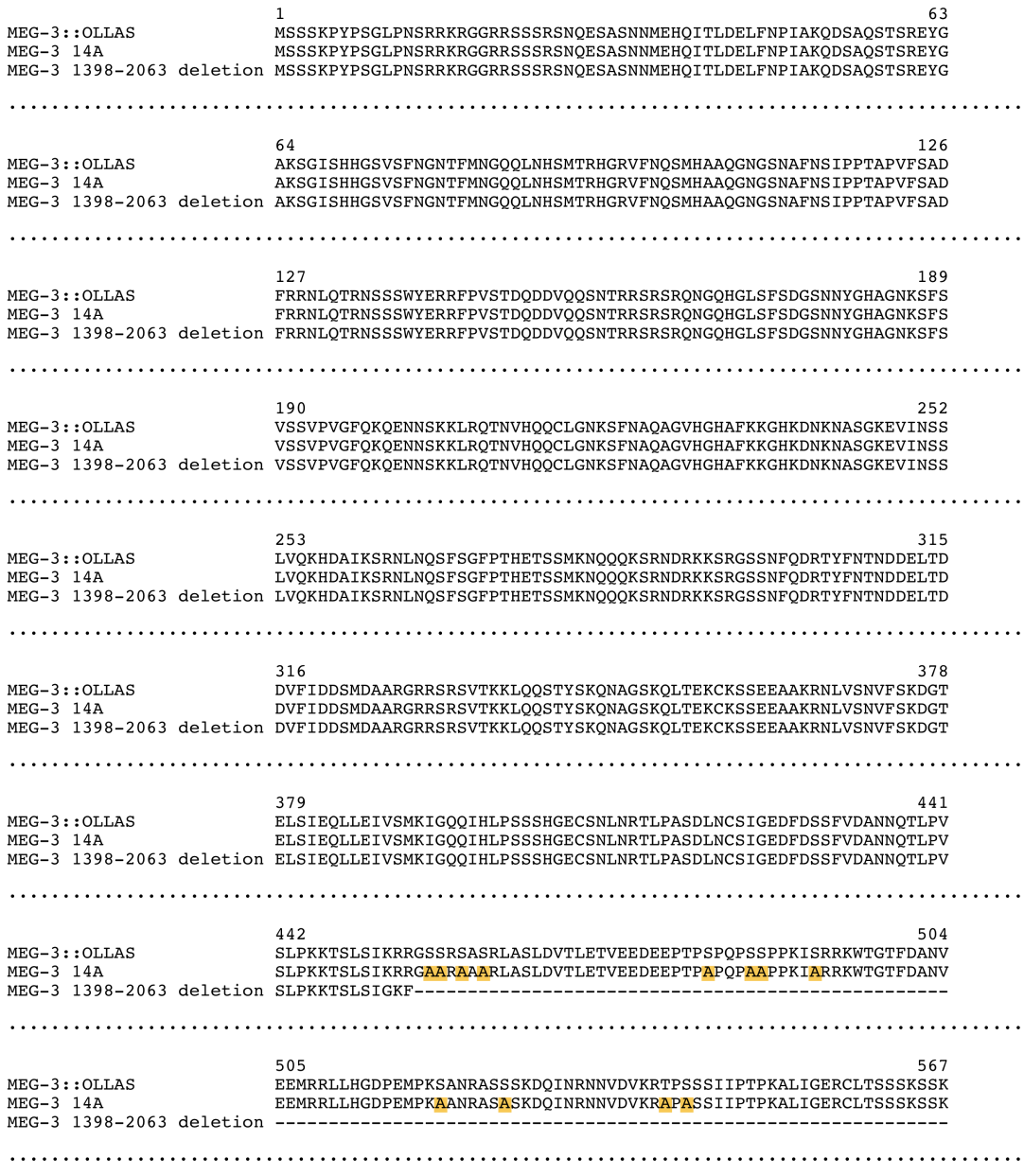

Figure 1 –supplement 1 B continued

```
                         568                                                  630
MEG-3::OLLAS             LNKSLGVVDSKATKSPMYSVTVSGKETASGKRIAQKLTPKVVALESSYITGIPVSTDCNGCPT
MEG-3 14A                LNKSLGVVDSKATKAPMYSVTVSGKETASGKRIAQKLAPKVVALESSYITGIPVSTDCNGCPT
MEG-3 1398-2063 deletion ----------------------------------------------------VQSRGGCPT

.....................................................................................

                         631                                                  693
MEG-3::OLLAS             PKRSGINCEIRAAEVYNQAGKWPFEITSDPAPLPCESADRIEYPSQDCTQDPASTSPPPRISE
MEG-3 14A                PKRSGINCEIRAAEVYNQAGKWPFEITSDPAPLPCESADRIEYPSQDCTQDPASTSPPPRISE
MEG-3 1398-2063 deletion PKRSGINCEIRAAEVYNQAGKWPFEITSDPAPLPCESADRIEYPSQDCTQDPASTSPPPRISE

.....................................................................................

                         694                                                  756
MEG-3::OLLAS             SLTAFLEAQQDFNDYIDTNYKEKTQLLKVNLNIHGMSPERWLYLNYFCTETIPRLDGPYADDP
MEG-3 14A                SLTAFLEAQQDFNDYIDTNYKEKTQLLKVNLNIHGMSPERWLYLNYFCTETIPRLDGPYADDP
MEG-3 1398-2063 deletion SLTAFLEAQQDFNDYIDTNYKEKTQLLKVNLNIHGMSPERWLYLNYFCTETIPRLDGPYADDP

.....................................................................................

                         757                                                  819
MEG-3::OLLAS             RVPPVRNMFRKWFLRFAEACLGNPHQLAVMQEIAATFVQARLDDTSSSTDSTNMLYMLWKECI
MEG-3 14A                RVPPVRNMFRKWFLRFAEACLGNPHQLAVMQEIAATFVQARLDDTSSSTDSTNMLYMLWKECI
MEG-3 1398-2063 deletion RVPPVRNMFRKWFLRFAEACLGNPHQLAVMQEIAATFVQARLDDTSSSTDSTNMLYMLWKECI

.....................................................................................

                         820                                              876
MEG-3::OLLAS             GQKNIIAIADACLLAHLRKSDPIKYLNVKRDWLESIFDPPRDQSGFANELGPRLMGK
MEG-3 14A                GQKNIIAIADACLLAHLRKSDPIKYLNVKRDWLESIFDPPRDQSGFANELGPRLMGK
MEG-3 1398-2063 deletion GQKNIIAIADACLLAHLRKSDPIKYLNVKRDWLESIFDPPRDQSGFANELGPRLMGK

.....................................................................................
```

Figure 2 - Characterization of MEG-3_{14A}

A. Representative photomicrographs of one-cell embryos expressing wild type MEG-3 or MEG-3_{14A} and immunostained for MEG-3 (anti-OLLAS antibody) and PGL-1 (anti-PGL-1 antibody). Images are maximum projections of 15 z-slices spaced 1µm apart.

B. Westerns of mixed-stage embryos (1-100 cell stage) harvested from synchronized worms expressing the indicated OLLAS-tagged proteins. N2 is a negative control.

C. Representative photomicrographs of one-cell embryos expressing wild type MEG-3 or MEG-3_{14A} and PGL-1::GFP. Images are sum projections of 15 z-slices spaced 1µm apart.

D. Scatterplot of the mean PGL-1::GFP intensity over background in one cell embryos expressing MEG-3 or MEG-3_{14A}. Each dot represents an embryo. Bars are the mean and one standard deviation.

E. Westerns of embryos expressing MEG-3 or MEG-3_{14A}. N2 is a negative control.

F. Westerns of embryos expressing the indicated OLLAS-tagged proteins run on SDS-PAGE gels with (top) and without (bottom). Two independent replicates are shown (right and left).N2 is a negative control. MEG-1 is included as a positive control for the Phos-tag reagent, note the separation into two distinct bands.

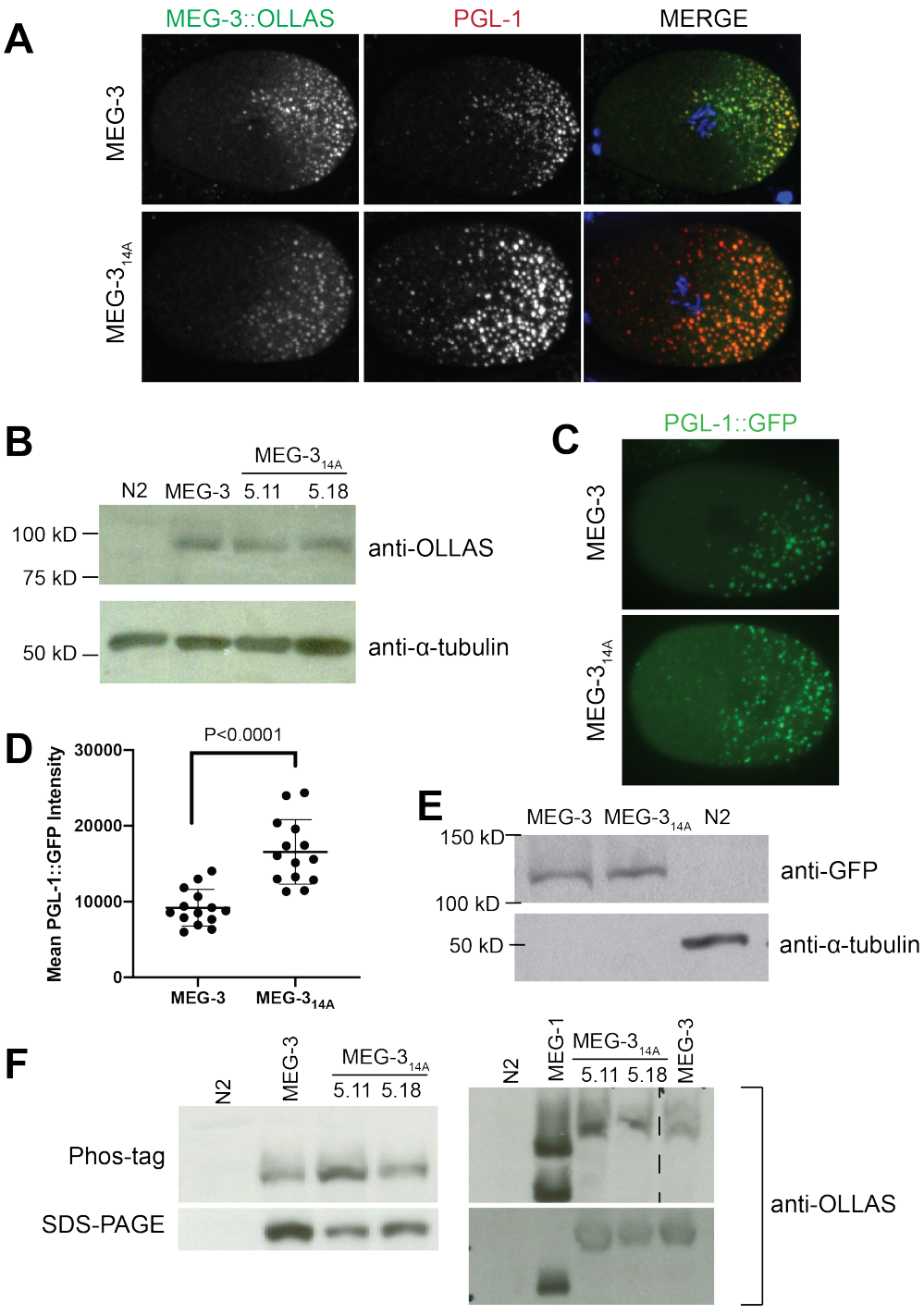
A
MEG-3::OLLAS
PGL-1
MERGE
MEG-3
MEG-3 14A
B
MEG-3 14A
N2
MEG-3
5.11
5.18
100 kD
75 kD
anti-OLLAS
50 kD
anti-α-tubulin
C
PGL-1::GFP
MEG-3
MEG-3 14A
D
P<0.0001
Mean PGL-1::GFP Intensity
30000
20000
10000
0
MEG-3
MEG-3 14A
E
MEG-3
MEG-3 14A
N2
150 kD
anti-GFP
100 kD
50 kD
anti-α-tubulin
F
N2
MEG-3
MEG-3 14A
5.11 5.18
Phos-tag
SDS-PAGE
N2
MEG-1
MEG-3 14A
5.11 5.18
MEG-3
anti-OLLAS

Appendix D

Replacement of all serines in the MEG-3 intrinsically disordered region (aa1-544) with alanine

A portion of the results in this chapter are also published in “Cas9-assisted recombineering in C. elegans: genome editing using in vivo assembly of linear DNAs.“ by Paix, A., Schmidt, H., Seydoux, G., published in Nucleic Acids Res. 44, e128 in 2016

D.1 Rationale

While MEG-3 localization is affected by loss of MBK-2 kinase activity (Appendix B), mutating 14 possible phosphorylation sites in MEG-3 did not have a noticeable affect on MEG-3 localization (Appendix C). This experiment served a dual purpose, to determine if mutating all the serines in MEG-3 to alanine would affect its localization, but also to determine if we could replace an entire gene by homology directed repair. Starting with a strain (JH3439) in which the meg-3 coding sequence had been deleted and replaced with a Cas9 guide sequence and PAM (HotSpot 2 GGCAGGATGTCAGCCAGAGG) the MEG-3 disordered region was inserted with 87 serine to alanine mutations (hereafter referred to as MEG-$3_{IDR\ 87A}$) with a C-terminal OLLAS tag. To allow for the possibility of the remaining sequence to be inserted later, a new guide sequence (Hotspot 1 GGGAAGTTTGTCCAGAGCAG) was included 5' to the OLLAS tag. A schematic of the *meg-3* locus before and after editing, as well as the repair templates is provided in Figure 1. DNA and protein sequence of MEG-$3_{IDR\ 87A}$ as compared to MEG-3_{IDR} are provided in Figure 1 – supplement 1

D.2 Results

Of the 92 F1 progeny screened by CRISPR, four had inserts of the expected size and three had smaller inserts. The four correct inserts were isolated as homozygotes. To confirm expression, we performed a western blot for the OLLAS tag on mixed-stage whole worm lysates. Expression of an OLLAS-tagged protein of the expected size (62kD) was confirmed only in lines B (JH3892) and D (JH3893), while lines A and C did not express any OLLAS tagged proteins (Figure 2).

To determine the localization of MEG-$3_{IDR\ 87A}$ we performed immunofluorescence on embryos from the MEG-$3_{IDR\ 87A}$ expressing lines B and D, as well as embryos expressing MEG-3_{IDR} as a positive control. As expected, MEG-3_{IDR} was enriched in the P cell but was not strongly enriched in P granules. However, both lines of MEG-$3_{IDR\ 87A}$ were symmetric in the embryo and did not enrich in P granules at any stage of embryonic development (Figure 3).

D.3 Conclusions and further questions

It is possible to insert nearly 2kb by homology directed repair using two overlapping dsDNA templates. Splitting the homology-directed repair template as such is likely to be most beneficial when making large insertions where achieving high concentrations of long repair templates is challenging.

MEG-$3_{IDR\ 87A}$ can be expressed from the MEG-3 locus. However, while MEG-$3_{IDR\ 87A}$ expression was detectable by western blot in mixed-stage worms, by immunofluorescence it appeared to be at a much lower level than MEG-3_{IDR} in the early embryo. It is possible that the expression seen on the western blot is actually present at a different stage of development. Additionally, while the HotSpot guide sequences were designed to produce an in-frame peptide, this does add 16 amino acids with unknown affect to the final protein. Due to the many caveats with this strain and that it appeared completely non-functional, the C-terminal sequence was never added.

If it is indeed expressed in the early embryo, MEG-$3_{IDR\ 87A}$ appears to be deficient in both the granule and cytoplasmic gradient functions of MEG-3. As MEG-3_{IDR} is necessary and sufficient for MEG-3 to bind RNA and enrich in the P cell (Smith et al.,

2016), it might be interesting to test the RNA binding of MEG-$3_{IDR\ 87A}$ *in vitro*, given it fails to enrich in the P cell.

Finally, since these experiments were performed in embryos with the *meg-4* locus intact, PGL-1 localization was not affected. However, given MEG-3_{IDR} is not sufficient to localize PGL-1/3, MEG-$3_{IDR\ 87A}$ would likely be insufficient as well.

D.4 Methods

CRISPR/Cas9 genome editing - CRISPR/Cas9 genome editing was performed as described in (Paix et al., 2017b). A list of strains generated in this study along with the required guides, repair templates and starting strains is provided in Appendix F - Table 1. Genome edits were detected by PCR with primers CATTCTTGTTGCGTGGTCCC and TCACAAGGAGAAGCGAGTTG. Expected sizes are deletion = 278 bp, insertion of MEG-3_{87A} = 2024 bp.

Western blotting - Mixed-stage worms were collected from unsynchronized plates of worms and washed three times in M9. Worms were pelleted by centrifugation and resuspened in 50 µL PBS/protease inhibitor (1 Roche complete mini with EDTA dissolved in 50mL of PBS). For each lane, 5.5 µL of worms was mixed with 2.5 µL 4x sample buffer (Bio-Rad Hercules, CA) and 2 µL 1M DTT. Samples were then snap-frozen and thawed in a 40˚C water bath three times to lyse them, then denatured at 95˚C for five minutes. Lysates were briefly spun down then run on 4-12% Bis-Tris pre-cast gels (Bio-Rad Hercules, CA). Western blot transfer was performed for 1 hr at 4°C onto PVDF membranes. Membranes were blocked overnight and washed in 5% milk, 0.1% Tween-20 in PBS; primary antibodies were incubated overnight at 4˚ C; secondary antibodies

were incubated for two hours at room temperature. Antibody dilutions in 5% milk/PBST: Rat α OLLAS-L2 (1:1000, Novus Biological Littleton, CO), Mouse α tubulin (1:1000, Sigma St. Louis, MO),

Immunostaining **-** Adult worms were placed into M9 on poly-l-lysine (0.01%) coated slides and squashed with a coverslip to extrude embryos. Slides were frozen by laying on aluminum blocks pre-chilled with dry ice for >5 min. Embryos were permeabilized by freeze-cracking (removal of coverslips from slides) followed by incubation in methanol at -20˚C for >15 min, and in acetone -20˚C for 10 min. Slides were blocked in PBS-Tween (0.1%) BSA (0.5%) for 30min at room temperature, and incubated with 50 ul primary antibody overnight at 4˚C in a humid chamber. Primary antibody dilution (in PBST/BSA) Rat αOLLAS-L2 (1:200, Novus Biological Littleton, CO), Secondary antibody was applied for 2 hr at room temperature. Samples were mounted in VECTASHIELD Antifade Mounting Media with DAPI. Embryos were staged using DAPI stained nuclei.

Confocal Imaging - Fluorescence confocal microscopy was performed using a Zeiss Axio Imager with a Yokogawa spinning-disc confocal scanner. Samples were illuminated with 405/488/561/637nm solid-state laser (Coherent), using a 405/488/561/640 transmitting dichroic (Semrock) and 624-40/692-40/525-30/445-45nm bandpass filter (Semrock) respectively. Images from either microscope were taken with using Slidebook v6.0 software (Intelligent Imaging Innovations) using a 63X-1.4NA.

D.5 Figures

Figure 1 - Diagram of the insertion of MEG-$3_{IDR\ 87A}$ at the *meg-3* locus using CRISPR/Cas9.

A. *meg-3* locus in the starting strain, JH3439 in which the *meg-3* open reading frame is replaced with the sequence of guide RNA HotSpot 2

B. Two overlapping dsDNA repair templates for MEG-$3_{IDR\ 87A}$ generated by PCR. Homology arms overlapping with the genome and each other are 35bp.

C. *meg-3* locus in the resulting MEG-$3_{IDR\ 87A}$ strain.

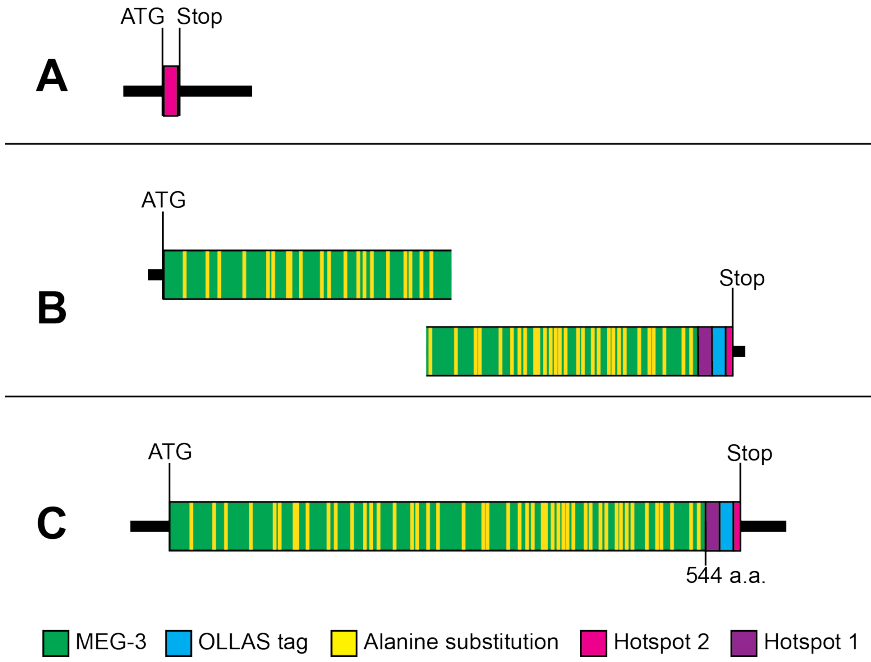
A
ATG
Stop
B
ATG
Stop
C
ATG
Stop
544 a.a.
MEG-3
OLLAS tag
Alanine substitution
Hotspot 2
Hotspot 1

Figure 1 – supplement 1 DNA and protein sequences of MEG-$3_{IDR\ 87A}$ aligned with MEG-3_{IDR}

A. Aligned DNA sequences of the coding region of MEG-$3_{IDR\ 87A}$ and MEG-3_{IDR} . Exons are in uppercase, introns in lowercase. Yellow color indicates alanine substitutions, purple indicates the HotSpot 1 and PAM DNA sequence, blue indicates the OLLAS sequence and pink indicates remaining HotSpot 2 and PAM DNA sequence. Asterisks below the sequence indicate 100% identical bases between the sequences

B. Aligned protein sequences MEG-$3_{IDR\ 87A}$ and MEG-3_{IDR}. Yellow color indicates the alanine substitutions, purple color indicates the HotSpot 1 and PAM sequence, blue color indicates the OLLAS tag, and pink indicates remaining HotSpot 2 and PAM.

Figure 1 – supplement 1 A

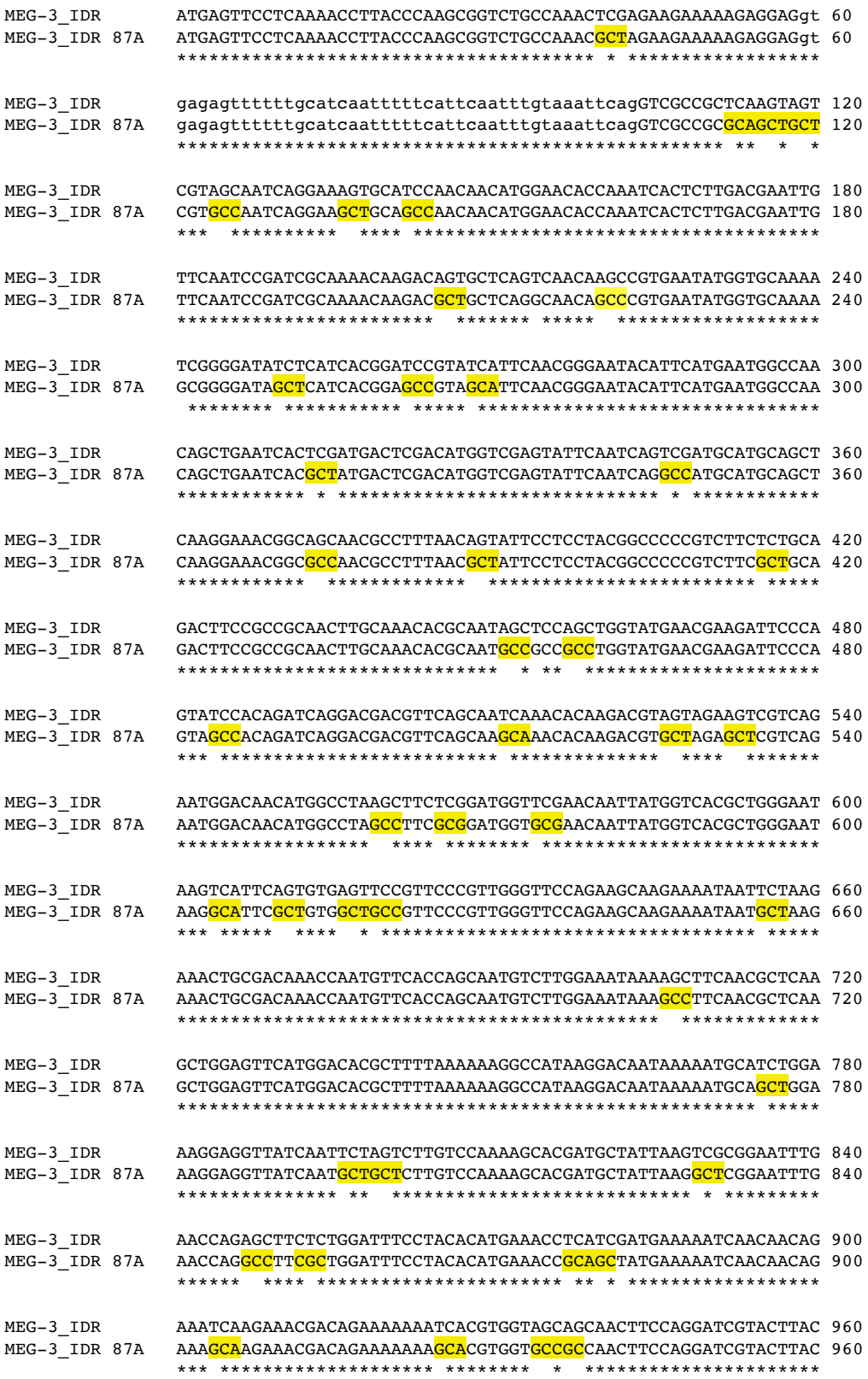

Figure 1 – supplement 1 A continued

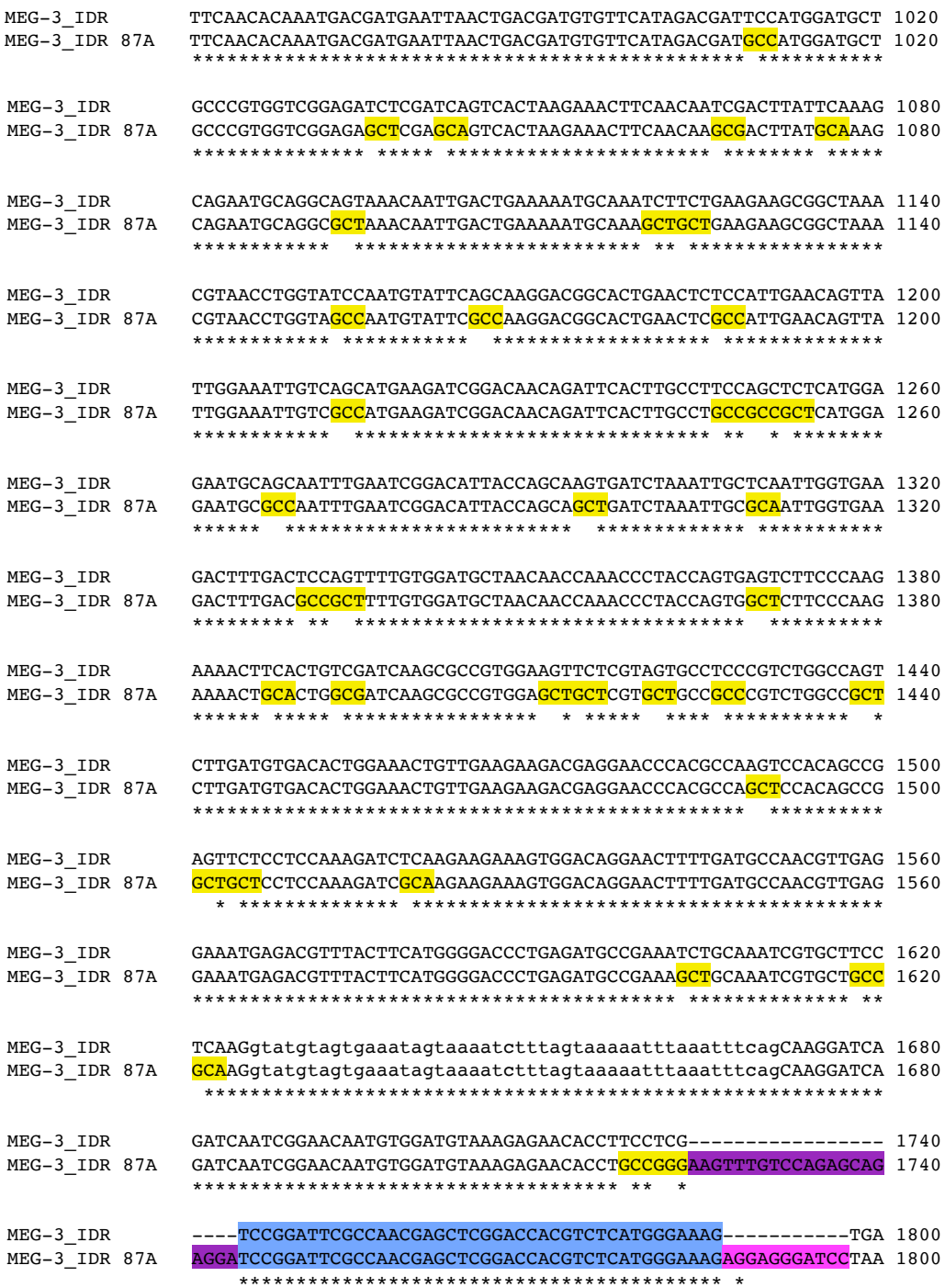

Figure 1 – supplement 1 B

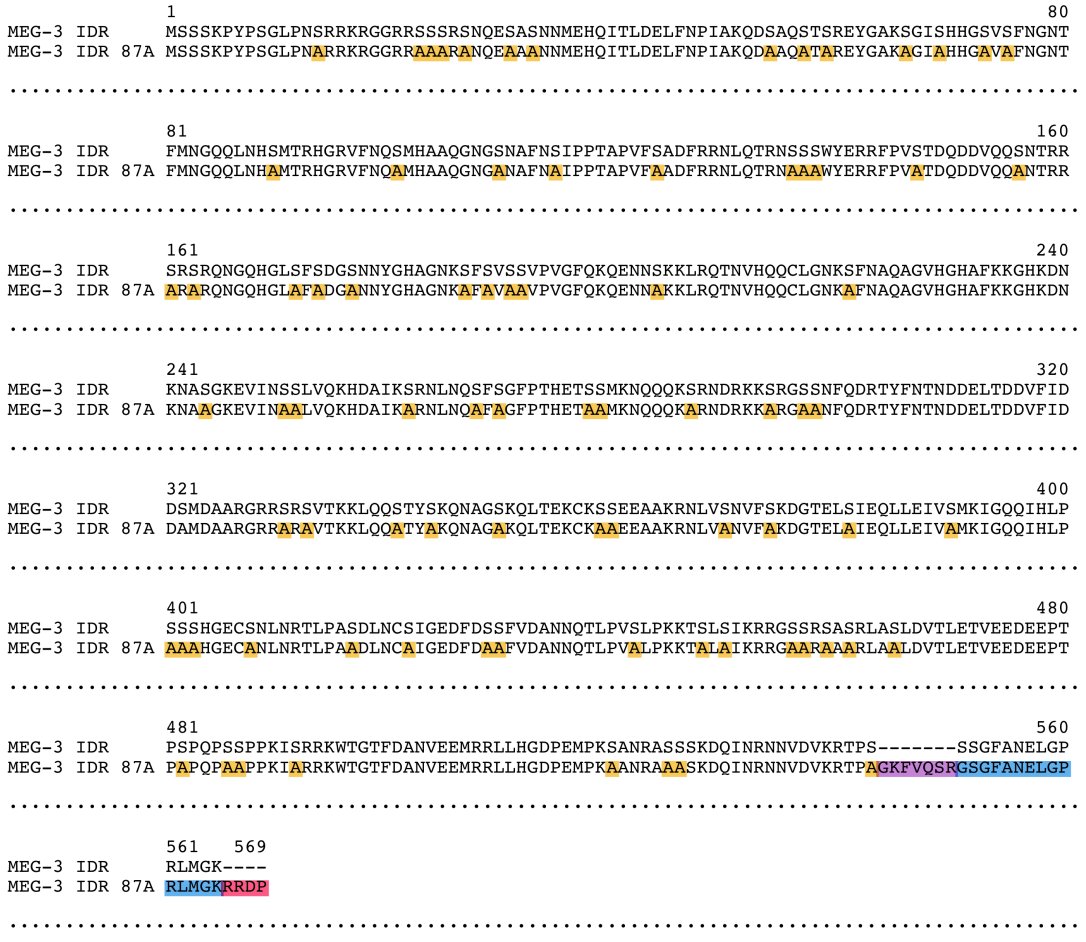

Figure 2 - Western blot to confirm MEG-$3_{IDR\ 87A}$ expression

A. Western blots of mixed-stage worms (L1-gravid adult) expressing the indicated MEG-3 derivatives or no OLLAS-tagged protein (N2, negative control).

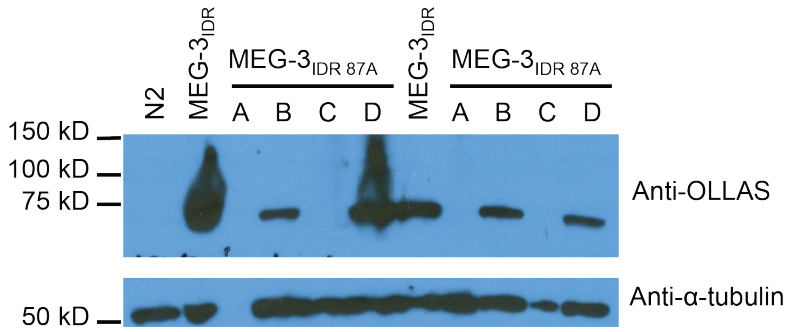
N2
MEG-3IDR
MEG-3IDR 87A
A B C D
MEG-3IDR
MEG-3IDR 87A
A B C D
150 kD
100 kD
75 kD
Anti-OLLAS
50 kD
Anti-α-tubulin

Figure 3 - MEG-$3_{IDR\ 87A}$ localization in embryos

A. Representative photomicrographs of embryos expressing the Indicated MEG-3 derivatives and immunostained for MEG-3 (anti-OLLAS antibody). Images are maximum projections of 15 z-slices spaced 1µm apart.

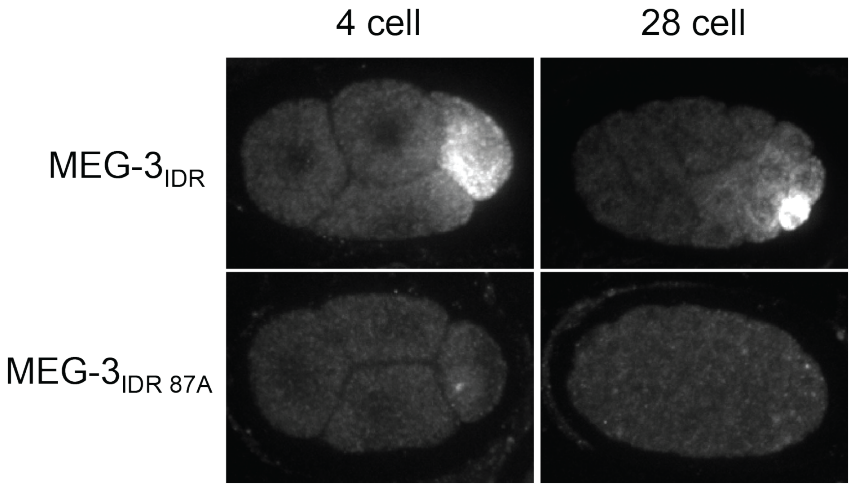
4 cell
28 cell
MEG-3IDR
MEG-3IDR 87A

Appendix E

RNAi insensitivity of MEG-3 derivatives

E.1 Rationale

meg-3 and *meg-4* are redundantly required for dsRNA-mediated gene silencing (RNAi) (Dodson and Kennedy, 2019; Ouyang et al., 2019). As the MEG-3 derivatives (MEG-3_{Cterm}, MEG-3_{IDR}, MEG-3_{HMGL-}) all have fertility defects and fail to enrich mRNAs in the embryonic P cell similar to the *meg-3 meg-4* double deletion, we wondered if they might also affect the RNAi response.

E.2 Results

When treated with control RNAi, all genotypes had no embryonic lethality. Worms expressing wild-type MEG-3 had 100% embryonic lethality when treated with *pos-1* RNAi. Consistent with published results, *meg-3 meg-4* worms were completely resistant to RNAi, having no embryonic lethality when treated with *pos-1* RNAi. MEG-3_{Cterm} and MEG-3_{HMGL-} behaved identically to the double deletion. However, worms expressing MEG-3_{IDR} had only a partial resistance to RNAi, with an average of 27% embryonic lethality on *pos-1* RNAi (Figure 1).

E.3 Conclusions and further questions

The MEG-3 IDR, C-terminus and HMG-like motif are all required for the full RNAi response, however loss of the C-terminus appears to be less severe than the other mutations. These data are the result of a single experiment containing multiple replicates. Before delving deeper, this experiments should be repeated, including with an RNAi construct targeting a different gene. If it holds that worms expressing MEG-3_{IDR} are still partially competent for RNAi while the other derivatives are not, this would be

interesting to explore further, perhaps by comparing small RNA sequencing between the derivatives and/or the double deletion.

E.4 Methods

RNAi treatment and embryonic lethality - Worms were treated with *pos-1* or control RNAi, from hatch to adulthood, by placing ~10 mothers in a drop of bleach on the appropriate RNAi plate. Embryonic lethality was scored by placing ~10 RNAi-treated mothers onto a fresh RNAi plate and allowing them to lay eggs for ~2 hours. Mothers were then removed and the number of embryos was counted. The number of adults on each plate was then counted after three days. Embryonic lethality for each plate was calculated as [(embryos – adults)/embryos]. In the case where the number of adults observed exceeded the number of embryos, the embryonic lethality was scored as 0%.

E.5 Figures

Figure 1 – Response to RNAi treatment of MEG-3 derivatives

A. Plot of the embryonic lethality of the indicated MEG-3 derivatives in a *meg-4* deletion background following the indicated RNAi treatment. Each dot represents the pooled ~2hr brood of ~10 mothers. Total number of embryos counted is indicated above

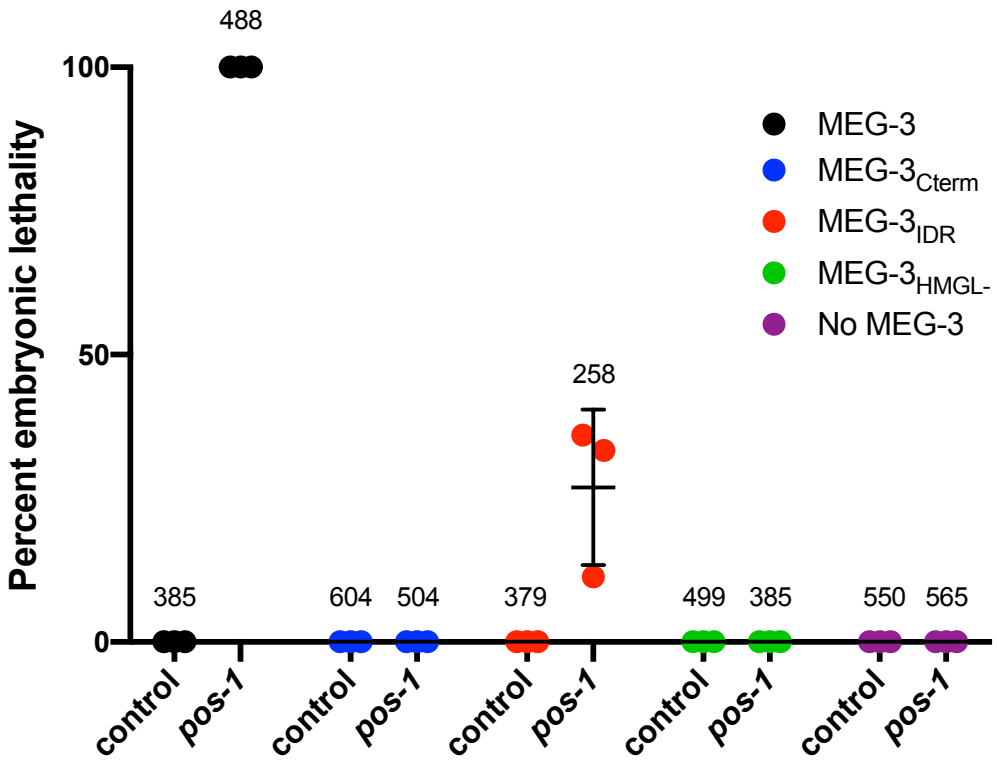
488
100
50
0
Percent embryonic lethality
MEG-3
MEG-3Cterm
MEG-3IDR
MEG-3HMGL-
No MEG-3
258
385
604
504
379
499
385
550
565
control
pos-1
control
pos-1
control
pos-1
control
pos-1
control
pos-1

Table 1 – Individual replicate values for response to RNAi treatment of MEG-3 derivatives

MEG-3 Genotype	RNAi	Replicate 1		Replicate 2		Replicate 3		**Average**	
		(n)	Embryonic Lethality	(n)	Embryonic Lethality	(n)	Embryonic Lethality	**Total (n)**	**Embryonic Lethality**
MEG-3	control	126	0.0%	122	0.0%	137	0.0%	**385**	**0.0%**
	pos-1	121	100.0%	200	100.0%	167	100.0%	**488**	**100.0%**
$MEG\text{-}3_{Cterm}$	control	167	0.0%	145	0.0%	292	0.0%	**604**	**0.0%**
	pos-1	180	0.0%	150	0.0%	174	0.0%	**504**	**0.0%**
$MEG\text{-}3_{IDR}$	control	122	0.0%	119	0.0%	138	0.0%	**379**	**0.0%**
	pos-1	89	36.0%	63	33.3%	106	11.3%	**258**	**26.9%**
$MEG\text{-}3_{HMGL\text{-}}$	control	194	0.0%	156	0.0%	149	0.0%	**499**	**0.0%**
	pos-1	132	0.0%	148	0.0%	105	0.0%	**385**	**0.0%**
meg-3	control	184	0.0%	175	0.0%	191	0.0%	**550**	**0.0%**
	pos-1	143	0.0%	248	0.0%	174	0.0%	**565**	**0.0%**

Appendix F

Table of *C. elegans* strains generated in this work

Table 1 – *C. elegans* strains generated by CRISPR/Cas9 editing in the course of this work. Includes required guide RNAs, homology directed-repair templates and starting strains. Strains marked by an asterix (*) were not maintained.

Strain	Genotype	Description	Derived from	Guide RNA sequence(s)	Repair Template	Published
JH3477	*meg-3(ax3051) meg-4(ax3052)*	MEG-3::OLLAS *meg-4* deletion	JH3374	tctgcccaggaacttgtaac, ggagtttggcagatcacatg	gttgcaggtatgagttcttcaaagctttcctcatgtgggaagtttgtccagagcagagg aacgggtagttttctattgttatcaggactgctgc	Smith et al., 2016
JH3479	*meg-3(ax3056) meg-4(ax3052)*	MEG-3_{IDR}::OLLAS *meg-4* deletion	JH3422	same as JH3477	same as JH3477	Smith et al., 2016
JH3517	*meg-3(ax4500) meg-4(ax2080)*	MEG-3_{698}::OLLAS MEG-4::3xFLAG	JH3374	tgaaagcttgacagcattcctgg, tcagtacaatcattgatctc	caccacctcgcatttctgaaagcttgacagcattccaatccggattcgccaacgagc tcggaccacgtctcatgggaaagtgattgtaccaatttatatctattacttgtagact ata	Chapter 2
JH3630	*meg-3(ax4500) meg-4(ax4505)*	MEG-3_{698}::OLLAS *meg-4* deletion	JH3517	same as JH3477	same as JH3477	Chapter 2
JH3632	*meg-3(4501) meg-4(ax3052)*	MEG-3(HMGL deletion)::OLLAS meg-4 deletion	JH3477	gtcaagctttcagaaatgcg, atccaatcttggaattgtct	ctcaagatccagcttcaacctcgccaccacctcgcacaattccaagattggatggtc cttatgccgatgg	Chapter 2
JH3861	*meg-3(3502) meg-4(ax3052)*	MEG-3_{HMGL}::OLLAS *meg-4* deletion	JH3632	tccaatcttggaattgtgcg	ctcaagatccagcttcaacctcgccaccacctcgcatttctgaaagcttgacagcat ttttggaggcgcaacaggatgccaacgacgctattgatactaacgccaaagaaaa gacacaactcctgaaagtgaatttggctattcacgggatgtcacctgaaagatggc tgtacttgaattatttttgcaccgagacaattccaagattggatggtccttatgccga tgg	Chapter 2
JH3420	*meg-3(ax4503) meg-4(ax2080)*	MEG-3_{Cterm}::OLLAS MEG-4::3xFLAG	JH3374	tcctcaaaaccttacccaag, tcagatcaatcggaacaatg	tttttgcaggtatgagctcctcaaaaccttacccatcgtcaatcatcccaactccaaa ggctttgatcgg	Chapter 2
JH3553	*meg-3(ax4503) meg-4(ax4504)*	MEG-3_{Cterm}::OLLAS *meg-4* deletion	JH3420	same as JH3477	same as JH3477	Chapter 2
JH3475	*meg-3(ax3055) meg-4(ax3052)*	*meg-3* deletion *meg-4* deletion	JH3477	tcctcaaaaccttacccaag, tcgagtttggcagaccgctt	gcaggtatgagttcctcaaaaccttacccaagggcaggatgtcagccagaggagg gatcctaattgtaccaatttatatctattacttgtagactatattg	Smith et al., 2016
JH3196	*mbk-2(2052)*	V5::MBK-2	N2	ctttttgagccgtcaacat	gctctcgttatctttgaaagttaaagtgagttgagagtgtaacacactcggccacac acacacaagaatgggaaagccaattccgaatccgcttctcggcttggattcaacta cacttttgagccgtcaacatcgggcaatcgaatggggtatagaggtaagagag	Paix et al., 2014
JH3274	*meg-1(ax2051); nos-2(ax2049)*	MEG-1::OLLAS; NOS-2::3xFLAG	JH3193	ccaacgtctcattcattgct	agacttgtgaacttatataaataacaagcaatttttttttcagtgacaaggaattgcc aagcaatgaatccggattcgccaacgagctcggaccacgtctcatgggaaagtga gacgttggacaattggttcgcctacaagaacacacttactgtgctgc	Appendix A
F9-5-5*	*meg-3(ax3051) meg-4(ax3052); mbk-2(dd5)*	MEG-3::OLLAS MEG-4::FLAG; *mbk-2 (ts)*	JH3347	agaggatgagaatgaccagc	ccggatatccattattgcccggggaagacgaaaacaaccagctggcacttatcatt gaactactcggaagaggatg	Appendix B
F9-6-4*	*meg-3(ax3051) meg-4(ax3052); mbk-2(dd5)*	MEG-3::OLLAS MEG-4::FLAG; *mbk-2 (ts)*	JH3374	same as F9-5-5	same as F9-5-5	Appendix B
JH3889	*meg-3(ax4506) meg-4(ax2080)*	MEG-3(1398-2063bp Hotspot1 deletion)::OLLAS MEG-4::FLAG	JH3477	tcactgtcgatcaagcgccg, tgggcaaccattacaatccg	gcaggtatgagttcctcaaaaccttacccaagggcaggatgtcagccagaggagg gatcctaattgtaccaatttatatctattacttgtagactatattg	Appendix C
JH3890	*meg-3(ax4507) meg-4(ax2080)*	MEG-3_{14A}::OLLAS MEG-4::FLAG	JH3889	ggcaggatgtcagccagagg	PCR amplification ccagtgagtcttcccaagaaaacttcactgtcgatc, caattgattccacttctcttcggagttgggcaacc	Appendix C
JH3891	*meg-3(ax4508) meg-4(ax2080)*	MEG-3_{14A}::OLLAS MEG-4::FLAG	JH3889	ggcaggatgtcagccagagg	same as 3890	Appendix C
JH3439	*meg-3(ax 3055) meg-4(ax 2080)*	*meg-3* (HotSpot 2 deletion) MEG-4::FLAG	JH3294	same as JH3475	same as JH3475	Appendix D
JH3894	*meg-3(ax4507) meg-4(ax2080); pgl-1(x)*	MEG-3_{14A}::OLLAS MEG-4::FLAG; PGL-1::meGFP	JH3890 x JH3269	n/a	n/a	Appendix C
JH3892	*meg-3(ax4509) meg-4(ax2080)*	MEG-$3_{IDR\ 87}$::OLLAS MEG-4::FLAG	JH3439	ggcaggatgtcagccagagg	PCR atgagttcctcaaaaccttaccc, gtctatgaacacatcgtcagtta left template, gattccatggatgctgcccg ggcaggtgttctctttacatcc rght template	Appendix D
JH3893	*meg-3(ax4510) meg-4(ax2080)*	MEG-$3_{IDR\ 87}$::OLLAS MEG-4::FLAG	JH3439	ggcaggatgtcagccagagg	same as JH3892	Appendix D

References

Aoki, S.T., Kershner, A.M., Bingman, C.A., Wickens, M., Kimble, J., 2016. PGL germ granule assembly protein is a base-specific, single-stranded RNase. Proc. Natl. Acad. Sci. U. S. A. 113, 1279–1284. https://doi.org/10.1073/pnas.1524400113

Arribere, J.A., Bell, R.T., Fu, B.X.H., Artiles, K.L., Hartman, P.S., Fire, A.Z., 2014. Efficient marker-free recovery of custom genetic modifications with CRISPR/Cas9 in Caenorhabditis elegans. Genetics 198, 837–846. https://doi.org/10.1534/genetics.114.169730

Banani, S.F., Lee, H.O., Hyman, A.A., Rosen, M.K., 2017. Biomolecular condensates: organizers of cellular biochemistry. Nat. Rev. Mol. Cell Biol. 18, 285–298. https://doi.org/10.1038/nrm.2017.7

Baugh, L.R., Hill, A.A., Slonim, D.K., Brown, E.L., Hunter, C.P., 2003. Composition and dynamics of the Caenorhabditis elegans early embryonic transcriptome. Dev. Camb. Engl. 130, 889–900. https://doi.org/10.1242/dev.00302

Beumer, K.J., Trautman, J.K., Mukherjee, K., Carroll, D., 2013. Donor DNA Utilization During Gene Targeting with Zinc-Finger Nucleases. G3 Bethesda Md 3, 657–664. https://doi.org/10.1534/g3.112.005439

Boke, E., Ruer, M., Wühr, M., Coughlin, M., Lemaitre, R., Gygi, S.P., Alberti, S., Drechsel, D., Hyman, A.A., Mitchison, T.J., 2016. Amyloid-like Self-Assembly of a Cellular Compartment. Cell 166, 637–650. https://doi.org/10.1016/j.cell.2016.06.051

Brangwynne, C.P., Eckmann, C.R., Courson, D.S., Rybarska, A., Hoege, C., Gharakhani, J., Jülicher, F., Hyman, A.A., 2009. Germline P granules are liquid droplets that

localize by controlled dissolution/condensation. Science 324, 1729–1732. https://doi.org/10.1126/science.1172046

Brenner, S., 1974. The Genetics of CAENORHABDITIS ELEGANS. Genetics 77, 71–94.

Carmell, M.A., Dokshin, G.A., Skaletsky, H., Hu, Y.-C., van Wolfswinkel, J.C., Igarashi, K.J., Bellott, D.W., Nefedov, M., Reddien, P.W., Enders, G.C., Uversky, V.N., Mello, C.C., Page, D.C., 2016. A widely employed germ cell marker is an ancient disordered protein with reproductive functions in diverse eukaryotes. eLife 5. https://doi.org/10.7554/eLife.19993

Dodson, A.E., Kennedy, S., 2019. Germ Granules Coordinate RNA-Based Epigenetic Inheritance Pathways. Dev. Cell 50, 704-715.e4. https://doi.org/10.1016/j.devcel.2019.07.025

Drozdetskiy, A., Cole, C., Procter, J., Barton, G.J., 2015. JPred4: a protein secondary structure prediction server. Nucleic Acids Res. 43, W389-394. https://doi.org/10.1093/nar/gkv332

Edgar, R.C., 2004. MUSCLE: multiple sequence alignment with high accuracy and high throughput. Nucleic Acids Res. 32, 1792–1797. https://doi.org/10.1093/nar/gkh340

Feric, M., Vaidya, N., Harmon, T.S., Mitrea, D.M., Zhu, L., Richardson, T.M., Kriwacki, R.W., Pappu, R.V., Brangwynne, C.P., 2016. Coexisting Liquid Phases Underlie Nucleolar Subcompartments. Cell 165, 1686–1697. https://doi.org/10.1016/j.cell.2016.04.047

Fuentes, R., Mullins, M.C., Fernández, J., 2018. Formation and dynamics of cytoplasmic domains and their genetic regulation during the zebrafish oocyte-

to-embryo transition. Mech. Dev. 154, 259–269. https://doi.org/10.1016/j.mod.2018.08.001

Gallo, C.M., Munro, E., Rasoloson, D., Merritt, C., Seydoux, G., 2008. Processing bodies and germ granules are distinct RNA granules that interact in C. elegans embryos. Dev. Biol. 323, 76–87. https://doi.org/10.1016/j.ydbio.2008.07.008

Gasiunas, G., Barrangou, R., Horvath, P., Siksnys, V., 2012. Cas9-crRNA ribonucleoprotein complex mediates specific DNA cleavage for adaptive immunity in bacteria. Proc. Natl. Acad. Sci. U. S. A. 109, E2579-2586. https://doi.org/10.1073/pnas.1208507109

Genzor, P., Bortvin, A., 2015. A unique HMG-box domain of mouse Maelstrom binds structured RNA but not double stranded DNA. PloS One 10, e0120268. https://doi.org/10.1371/journal.pone.0120268

Guillén-Boixet, J., Kopach, A., Holehouse, A.S., Wittmann, S., Jahnel, M., Schlüßler, R., Kim, K., Trussina, I.R.E.A., Wang, J., Mateju, D., Poser, I., Maharana, S., Ruer-Gruß, M., Richter, D., Zhang, X., Chang, Y.-T., Guck, J., Honigmann, A., Mahamid, J., Hyman, A.A., Pappu, R.V., Alberti, S., Franzmann, T.M., 2020. RNA-Induced Conformational Switching and Clustering of G3BP Drive Stress Granule Assembly by Condensation. Cell 181, 346-361.e17. https://doi.org/10.1016/j.cell.2020.03.049

Hanazawa, M., Yonetani, M., Sugimoto, A., 2011. PGL proteins self associate and bind RNPs to mediate germ granule assembly in C. elegans. J. Cell Biol. 192, 929–937. https://doi.org/10.1083/jcb.201010106

Jamieson-Lucy, A., Mullins, M.C., 2019. The vertebrate Balbiani body, germ plasm, and oocyte polarity. Curr. Top. Dev. Biol. 135, 1–34. https://doi.org/10.1016/bs.ctdb.2019.04.003

Jinek, M., Chylinski, K., Fonfara, I., Hauer, M., Doudna, J.A., Charpentier, E., 2012. A programmable dual-RNA-guided DNA endonuclease in adaptive bacterial immunity. Science 337, 816–821. https://doi.org/10.1126/science.1225829

Kinoshita, E., Kinoshita-Kikuta, E., Takiyama, K., Koike, T., 2006. Phosphate-binding Tag, a New Tool to Visualize Phosphorylated Proteins. Mol. Cell. Proteomics 5, 749–757. https://doi.org/10.1074/mcp.T500024-MCP200

Kistler, K.E., Trcek, T., Hurd, T.R., Chen, R., Liang, F.-X., Sall, J., Kato, M., Lehmann, R., 2018. Phase transitioned nuclear Oskar promotes cell division of Drosophila primordial germ cells. eLife 7. https://doi.org/10.7554/eLife.37949

Lee, C.-Y.S., Putnam, A., Lu, T., He, S., Ouyang, J.P.T., Seydoux, G., 2020. Recruitment of mRNAs to P granules by condensation with intrinsically-disordered proteins. eLife 9, e52896. https://doi.org/10.7554/eLife.52896

Li, H.-R., Chiang, W.-C., Chou, P.-C., Wang, W.-J., Huang, J.-R., 2018. TAR DNA-binding protein 43 (TDP-43) liquid-liquid phase separation is mediated by just a few aromatic residues. J. Biol. Chem. 293, 6090–6098. https://doi.org/10.1074/jbc.AC117.001037

Lin, Y., Protter, D.S.W., Rosen, M.K., Parker, R., 2015. Formation and Maturation of Phase-Separated Liquid Droplets by RNA-Binding Proteins. Mol. Cell 60, 208–219. https://doi.org/10.1016/j.molcel.2015.08.018

Little, S.C., Sinsimer, K.S., Lee, J.J., Wieschaus, E.F., Gavis, E.R., 2015. Independent and coordinate trafficking of single Drosophila germ plasm mRNAs. Nat. Cell Biol. 17, 558–568. https://doi.org/10.1038/ncb3143

Marnik, E.A., Updike, D.L., 2019. Membraneless organelles: P granules in Caenorhabditis elegans. Traffic Cph. Den. 20, 373–379. https://doi.org/10.1111/tra.12644

Mello, C.C., Kramer, J.M., Stinchcomb, D., Ambros, V., 1991. Efficient gene transfer in C.elegans: extrachromosomal maintenance and integration of transforming sequences. EMBO J. 10, 3959–3970.

Mészáros, B., Erdős, G., Dosztányi, Z., 2018. IUPred2A: context-dependent prediction of protein disorder as a function of redox state and protein binding. Nucleic Acids Res. 46, W329–W337. https://doi.org/10.1093/nar/gky384

Mitrea, D.M., Kriwacki, R.W., 2016. Phase separation in biology; functional organization of a higher order. Cell Commun. Signal. CCS 14, 1. https://doi.org/10.1186/s12964-015-0125-7

Molliex, A., Temirov, J., Lee, J., Coughlin, M., Kanagaraj, A.P., Kim, H.J., Mittag, T., Taylor, J.P., 2015. Phase separation by low complexity domains promotes stress granule assembly and drives pathological fibrillization. Cell 163, 123–133. https://doi.org/10.1016/j.cell.2015.09.015

Nakamura, H., DeRose, R., Inoue, T., 2019. Harnessing biomolecular condensates in living cells. J. Biochem. (Tokyo) 166, 13–27. https://doi.org/10.1093/jb/mvz028

Niepielko, M.G., Eagle, W.V.I., Gavis, E.R., 2018. Stochastic Seeding Coupled with mRNA Self-Recruitment Generates Heterogeneous Drosophila Germ Granules. Curr. Biol. CB 28, 1872-1881.e3. https://doi.org/10.1016/j.cub.2018.04.037

Nishi, Y., Rogers, E., Robertson, S.M., Lin, R., 2008. Polo kinases regulate C. elegans embryonic polarity via binding to DYRK2-primed MEX-5 and MEX-6. Dev. Camb. Engl. 135, 687–697. https://doi.org/10.1242/dev.013425

Ouyang, J.P.T., Folkmann, A., Bernard, L., Lee, C.-Y., Seroussi, U., Charlesworth, A.G., Claycomb, J.M., Seydoux, G., 2019. P Granules Protect RNA Interference Genes from Silencing by piRNAs. Dev. Cell 50, 716-728.e6. https://doi.org/10.1016/j.devcel.2019.07.026

Paix, A., Folkmann, A., Goldman, D.H., Kulaga, H., Grzelak, M.J., Rasoloson, D., Paidemarry, S., Green, R., Reed, R.R., Seydoux, G., 2017a. Precision genome editing using synthesis-dependent repair of Cas9-induced DNA breaks. Proc. Natl. Acad. Sci. U. S. A. 114, E10745–E10754. https://doi.org/10.1073/pnas.1711979114

Paix, A., Folkmann, A., Seydoux, G., 2017b. Precision genome editing using CRISPR-Cas9 and linear repair templates in C. elegans. Methods San Diego Calif 121–122, 86–93. https://doi.org/10.1016/j.ymeth.2017.03.023

Parker, D.M., Winkenbach, L.P., Boyson, S., Saxton, M.N., Daidone, C., Al-Mazaydeh, Z.A., Nishimura, M.T., Mueller, F., Osborne Nishimura, E., 2020. mRNA localization is linked to translation regulation in the Caenorhabditis elegans germ lineage. Dev. Camb. Engl. 147. https://doi.org/10.1242/dev.186817

Pellettieri, J., Reinke, V., Kim, S.K., Seydoux, G., 2003. Coordinate activation of maternal protein degradation during the egg-to-embryo transition in C. elegans. Dev. Cell 5, 451–462. https://doi.org/10.1016/s1534-5807(03)00231-4

Puigbò, P., Bravo, I.G., Garcia-Vallve, S., 2008. CAIcal: a combined set of tools to assess codon usage adaptation. Biol. Direct 3, 38. https://doi.org/10.1186/1745-6150-3-38

Putnam, A., Cassani, M., Smith, J., Seydoux, G., 2019. A gel phase promotes condensation of liquid P granules in Caenorhabditis elegans embryos. Nat. Struct. Mol. Biol. 26, 220–226. https://doi.org/10.1038/s41594-019-0193-2

Quintin, S., Mains, P.E., Zinke, A., Hyman, A.A., 2003. The mbk-2 kinase is required for inactivation of MEI-1/katanin in the one-cell Caenorhabditis elegans embryo. EMBO Rep. 4, 1175–1181. https://doi.org/10.1038/sj.embor.7400029

Reeves, R., 2001. Molecular biology of HMGA proteins: hubs of nuclear function. Gene 277, 63–81. https://doi.org/10.1016/s0378-1119(01)00689-8

Rio, D.C., 2012. Filter-binding assay for analysis of RNA-protein interactions. Cold Spring Harb. Protoc. 2012, 1078–1081. https://doi.org/10.1101/pdb.prot071449

Roovers, E.F., Kaaij, L.J.T., Redl, S., Bronkhorst, A.W., Wiebrands, K., de Jesus Domingues, A.M., Huang, H.-Y., Han, C.-T., Riemer, S., Dosch, R., Salvenmoser, W., Grün, D., Butter, F., van Oudenaarden, A., Ketting, R.F., 2018. Tdrd6a Regulates the Aggregation of Buc into Functional Subcellular Compartments that Drive Germ Cell Specification. Dev. Cell 46, 285-301.e9. https://doi.org/10.1016/j.devcel.2018.07.009

Saha, S., Weber, C.A., Nousch, M., Adame-Arana, O., Hoege, C., Hein, M.Y., Osborne-Nishimura, E., Mahamid, J., Jahnel, M., Jawerth, L., Pozniakovski, A., Eckmann, C.R., Jülicher, F., Hyman, A.A., 2016. Polar Positioning of Phase-Separated Liquid Compartments in Cells Regulated by an mRNA Competition Mechanism. Cell 166, 1572-1584.e16. https://doi.org/10.1016/j.cell.2016.08.006

Sander, J.D., Joung, J.K., 2014. CRISPR-Cas systems for editing, regulating and targeting genomes. Nat. Biotechnol. 32, 347–355. https://doi.org/10.1038/nbt.2842

Sanders, D.W., Kedersha, N., Lee, D.S.W., Strom, A.R., Drake, V., Riback, J.A., Bracha, D., Eeftens, J.M., Iwanicki, A., Wang, A., Wei, M.-T., Whitney, G., Lyons, S.M., Anderson, P., Jacobs, W.M., Ivanov, P., Brangwynne, C.P., 2020. Competing Protein-RNA Interaction Networks Control Multiphase Intracellular Organization. Cell 181, 306-324.e28. https://doi.org/10.1016/j.cell.2020.03.050

Seydoux, G., 2018. The P Granules of C. elegans: A Genetic Model for the Study of RNA-Protein Condensates. J. Mol. Biol. 430, 4702–4710. https://doi.org/10.1016/j.jmb.2018.08.007

Seydoux, G., Fire, A., 1994. Soma-germline asymmetry in the distributions of embryonic RNAs in Caenorhabditis elegans. Dev. Camb. Engl. 120, 2823–2834.

Smith, J., Calidas, D., Schmidt, H., Lu, T., Rasoloson, D., Seydoux, G., 2016. Spatial patterning of P granules by RNA-induced phase separation of the intrinsically-disordered protein MEG-3. eLife 5. https://doi.org/10.7554/eLife.21337

Stros, M., Launholt, D., Grasser, K.D., 2007. The HMG-box: a versatile protein domain occurring in a wide variety of DNA-binding proteins. Cell. Mol. Life Sci. CMLS 64, 2590–2606. https://doi.org/10.1007/s00018-007-7162-3

Subramaniam, K., Seydoux, G., 1999. nos-1 and nos-2, two genes related to Drosophila nanos, regulate primordial germ cell development and survival in Caenorhabditis elegans. Dev. Camb. Engl. 126, 4861–4871.

Tauber, D., Tauber, G., Parker, R., 2020. Mechanisms and Regulation of RNA Condensation in RNP Granule Formation. Trends Biochem. Sci. 45, 764–778. https://doi.org/10.1016/j.tibs.2020.05.002

Thapar, R., 2015. Structure-specific nucleic acid recognition by L-motifs and their diverse roles in expression and regulation of the genome. Biochim. Biophys. Acta 1849, 677–687. https://doi.org/10.1016/j.bbagrm.2015.02.006

Trcek, T., Grosch, M., York, A., Shroff, H., Lionnet, T., Lehmann, R., 2015. Drosophila germ granules are structured and contain homotypic mRNA clusters. Nat. Commun. 6, 7962. https://doi.org/10.1038/ncomms8962

Trcek, T., Lehmann, R., 2019. Germ granules in Drosophila. Traffic Cph. Den. 20, 650–660. https://doi.org/10.1111/tra.12674

Tropea, J.E., Cherry, S., Waugh, D.S., 2009. Expression and purification of soluble His(6)-tagged TEV protease. Methods Mol. Biol. Clifton NJ 498, 297–307. https://doi.org/10.1007/978-1-59745-196-3_19

Uebel, C.J., Phillips, C.M., 2019. Phase-separated protein dynamics are affected by fluorescent tag choice. MicroPublication Biol. 2019.

Updike, D., Strome, S., 2010. P granule assembly and function in Caenorhabditis elegans germ cells. J. Androl. 31, 53–60. https://doi.org/10.2164/jandrol.109.008292

Updike, D.L., Hachey, S.J., Kreher, J., Strome, S., 2011. P granules extend the nuclear pore complex environment in the C. elegans germ line. J. Cell Biol. 192, 939–948. https://doi.org/10.1083/jcb.201010104

Van Treeck, B., Protter, D.S.W., Matheny, T., Khong, A., Link, C.D., Parker, R., 2018. RNA self-assembly contributes to stress granule formation and defining the stress granule transcriptome. Proc. Natl. Acad. Sci. U. S. A. 115, 2734–2739. https://doi.org/10.1073/pnas.1800038115

Waaijers, S., Boxem, M., 2014. Engineering the Caenorhabditis elegans genome with CRISPR/Cas9. Methods San Diego Calif 68, 381–388. https://doi.org/10.1016/j.ymeth.2014.03.024

Wang, Jennifer T, Smith, J., Chen, B.-C., Schmidt, H., Rasoloson, D., Paix, A., Lambrus, B.G., Calidas, D., Betzig, E., Seydoux, G., 2014. Regulation of RNA granule dynamics by phosphorylation of serine-rich, intrinsically disordered proteins in C. elegans. eLife 3, e04591. https://doi.org/library i

Wang, Jennifer T., Smith, J., Chen, B.-C., Schmidt, H., Rasoloson, D., Paix, A., Lambrus, B.G., Calidas, D., Betzig, E., Seydoux, G., 2014. Regulation of RNA granule dynamics by phosphorylation of serine-rich, intrinsically disordered proteins in C. elegans. eLife 3. https://doi.org/10.7554/elife.04591

Wilson, M., Koopman, P., 2002. Matching SOX: partner proteins and co-factors of the SOX family of transcriptional regulators. Curr. Opin. Genet. Dev. 12, 441–446. https://doi.org/10.1016/s0959-437x(02)00323-4

Wu, Y., Han, B., Gauvin, T.J., Smith, J., Singh, A., Griffin, E.E., 2019. Single-molecule dynamics of the P granule scaffold MEG-3 in the Caenorhabditis elegans zygote. Mol. Biol. Cell 30, 333–345. https://doi.org/10.1091/mbc.E18-06-0402

Yang, P., Mathieu, C., Kolaitis, R.-M., Zhang, P., Messing, J., Yurtsever, U., Yang, Z., Wu, J., Li, Y., Pan, Q., Yu, J., Martin, E.W., Mittag, T., Kim, H.J., Taylor, J.P., 2020. G3BP1 Is a Tunable Switch that Triggers Phase Separation to Assemble Stress Granules. Cell 181, 325-345.e28. https://doi.org/10.1016/j.cell.2020.03.046

Zagrovic, B., Bartonek, L., Polyansky, A.A., 2018. RNA-protein interactions in an unstructured context. FEBS Lett. 592, 2901–2916. https://doi.org/10.1002/1873-3468.13116

Zhang, D., Glotzer, M., 2014. Efficient site-specific editing of the C. elegans genome (preprint). Genetics. https://doi.org/10.1101/007344

Zhang, H., Elbaum-Garfinkle, S., Langdon, E.M., Taylor, N., Occhipinti, P., Bridges, A.A., Brangwynne, C.P., Gladfelter, A.S., 2015. RNA Controls PolyQ Protein Phase Transitions. Mol. Cell 60, 220–230. https://doi.org/10.1016/j.molcel.2015.09.017

CURRICULUM VITAE

EDUCATION

Johns Hopkins University Department of Genetic Medicine
PhD, Human Genetics (Expected) December 2020

University of Delaware
B.S. with Honors in Biochemistry, *summa cum laude* 2013

RESEARCH EXPERIENCE

Department of Molecular Biology and Genetics JHSOM 2013-present
Project: Structure function analysis *in vivo* and *in vitro* of the P granule scaffold protein MEG-3
Thesis Advisor: Geraldine Seydoux

University of Delaware Department of Plant and Soil Sciences 2010-2013
Project: Identification and classification of marine bacteriophages from shotgun metagenomic libraries
Advisor: K. Eric Wommack

University of Delaware Department of Chemistry and Biochemistry 2011
Project: Functional modification of poly-proline molecules for drug delivery
Advisor: Neal Zondlo

TEACHING EXPERIENCE

Teaching Assistant, for Principles of Genetics 2015
Primary Instructor: Geraldine Seydoux
Wrote and graded a portion of the problem sets and final exam, hosted help sessions for students

Teaching Assistant, Honors General Chemistry 111/112 2010-2013
Primary Instructor: Susan Groh
Graded a portion of all problem sets and exams, hosted help sessions for students

Laboratory Instructor, Elementary Biochemistry 216 2013
Primary Instructor: Karen Hoober
Instructed the lab portion of the course, graded lab reports and hosted help sessions for students

CONFERENCE PRESENTATIONS

Biomolecular Condensates: Phase-Separated Organizers of Cellular Biochemistry in Snowbird, UT April 10-13, 2019
Poster: How to build an RNA granule: surprise, it's not only about IDRs!

2017 ASCB | EMBO Meeting in Philadelphia, PA December 2-6, 2017
Poster: How to build a granule: distinct roles for globular and intrinsically-disordered domains in P granule assembly

ASCB Annual Meeting in San Francisco, CA December 3-7, 2016
Poster: Regulation of RNA granule assembly by phosphorylation of an intrinsically-disordered protein scaffold

PUBLICATIONS

Schmidt, H., Putnam, A., Rasoloson, D., Seydoux, G., 2020. Coordination of RNA and protein condensation by the P granule protein MEG-3. bioRxiv 2020.10.15.340570. https://doi.org/10.1101/2020.10.15.340570 ***Under review: eLife***

Smith, J., Calidas, D., **Schmidt, H**., Lu, T., Rasoloson, D., Seydoux, G., 2016. Spatial patterning of P granules by RNA-induced phase separation of the intrinsically-disordered protein MEG-3. Elife 5.

Paix, A., **Schmidt, H.,** Seydoux, G., 2016. Cas9-assisted recombineering in C. elegans: genome editing using in vivo assembly of linear DNAs. Nucleic Acids Res. 44, e128.

Wang, J.T., Smith, J., Chen, B.-C., **Schmidt, H.,** Rasoloson, D., Paix, A., Lambrus, B.G., Calidas, D., Betzig, E., Seydoux, G., 2014. Regulation of RNA granule dynamics by phosphorylation of serine-rich, intrinsically disordered proteins in C. elegans. Elife 3, e04591.

Paix, A., Wang, Y., Smith, H.E., Lee, C.-Y.S., Calidas, D., Lu, T., Smith, J., **Schmidt, H.,** Krause, M.W., Seydoux, G., 2014. Scalable and versatile genome editing using linear DNAs with microhomology to Cas9 Sites in Caenorhabditis elegans. Genetics 198, 1347–1356.

Schmidt, H.F., Sakowski, E.G., Williamson, S.J., Polson, S.W., Wommack, K.E., 2014. Shotgun metagenomics indicates novel family A DNA polymerases predominate within marine virioplankton. ISME J 8, 103–114.